Nonlinear integrated photonic devices based on gallium phosphide

Alejandro Lorenzo-Ruiz

To cite this version:

Alejandro Lorenzo-Ruiz. Nonlinear integrated photonic devices based on gallium phosphide. Optics / Photonic. INSA de Rennes, 2021. English. NNT : 2021ISAR0002 . tel-03279201

HAL Id: tel-03279201
https://theses.hal.science/tel-03279201

Submitted on 6 Jul 2021

THESE DE DOCTORAT DE

L'INSTITUT NATIONAL DES SCIENCES
APPLIQUEES RENNES

ECOLE DOCTORALE N° 596
Matière, Molécules, Matériaux
Spécialité : *Photonique*

Par
Alejandro LORENZO RUIZ

Nonlinear integrated photonic devices based on gallium phosphide

Thèse présentée et soutenue à Rennes le 05/02/2021
Unité de recherche : FOTON-OHM
Thèse N° : 21ISAR 04 / D21 - 04

Rapporteurs avant soutenance :

Christelle MONAT	Professeure, INL, Ecole centrale de Lyon
Mathieu CHAUVET	Professeur, FEMTO-ST, Université de Franche-Comté

Composition du Jury :

Président :	Sophie BOUCHOULE	Directrice de recherche CNRS, C2N, Université Paris-Saclay
Examinateur :	François LÉO	Chercheur FNRS, OPERA, Université libre de Bruxelles
Directeur de thèse :	Charles CORNET	Professeur, FOTON, INSA de Rennes
Co-encadrant. de thèse :	Yoan LÉGER	Chargé de recherche CNRS, FOTON, INSA de Rennes
Co-encadrant. de thèse :	Alexandre BECK	Maître de conférences, Institut FOTON, INSA de Rennes

Acknowledgments

Je voudrais remercier les membres du jury, que malgré la situation sanitaire ils ont réussi a lire et suivre mon travail de thèse. Merci à Christelle Monat et à Mathieu Chauvet pour leurs rapports très constructifs qui ont contribué à améliorer ce manuscrit. Je remercie également Sophie Bouchoule et François Léo pour leurs commentaires bienveillants sur ce travail.

J'exprime aussi ma gratitude à Pascal Besnard, directeur du laboratoire, pour m'avoir accepté dans l'Institut FOTON et Charles Cornet comment directeur de l'unite OHM. Évidement je remercie surtout Charles pour son travaille comment directeur de ma thèse ainsi que le travaille de Yoan Léger et Alexandre Beck comment co-encadrants. Nous avons réussi à faire un travaille dans des domaines différentes de la photonique, qui donne aujourd'hui des résultats prometteurs. Vous m'avez aidé beaucoup pendant ces 3 années à toutes les niveaux, hors labo aussi, je suis vraiment heureux de vous avoir eu comme encadrants de thèse.

Je remercie Julie Le Pouliquen et Karine Tavernier. Grâce à elles le travail en salle blanche a pu continuer même si nous étions confinés.

Bien sûr, je remercie Gaëlle et Alex car ils ont été des amis (et professeurs de français) exceptionnels. A tous les doctorants qui m'ont accueilli à mon arrivée, Ronan, Daniel, Ida, Mickaël et Tore et avec qui j'ai partagé du temps pendant ma thèse, Lipin, Ang, Marie, Mekan et Fei.

Je tiens également à remercier tout le personnel du laboratoire, qui m'a accueilli chaleureusement dès le début, en discutant avec moi et, bien sûr, en m'enseignant la culture française. Je remercie également beaucoup le personnel de l'INSA (service de recherche et groupe de renforcement musculaire) pour m'avoir aidé pendant mon séjour à Rennes, un gros câlin à tous.

Y por supuesto tendría que haber una parte de agradecimientos en español, en primer lugar agradecer a mis padres y a mi hermana, porque sin ellos (literalmente) nada de esto hubiese sido posible. Y agradecer a toda mi familia por haberme acompañado durante todo este camino.

Continuo agradeciendo a todos mis amigos que han sido el apoyo más grande que uno podría desear: Agus, Alfonso, Alberto, Andrés, Cristina, David, Fran, Ignacio, Isabel, Jaime, Juan Carlos, Manuel, Miguel F. y Miguel S. Por supuesto una mención especial a María por todo lo que ha aguantado durante estos tres años. Gracias también a todos aquellos que han compartido un rato de su tiempo conmigo.

Contents

Introduction

The realization of the *laser* in 1960 by Maiman [1] was the beginning of what has been called *photonics*. As the industry of semiconductors was growing enormously in the second half of the XXth century due to the microelectronics development, photonics was making use of that knowledge, leading to the creation of the first laser diodes during the sixties that culminated in 1970 with the demonstration of the first room-temperature continuous laser diode by Alferov and co-workers [2].

While the notion of *optical fiber* and *waveguide* were known long before these discoveries, researchers began to find applications to these devices. Probably, the most remarkable one was the transmission of information, proposed in 1966 by Kao *et al.* [3], and even used for the camera system that was sent to the Moon in 1968 by the NASA. The word *photonics* was proposed by Aigrain at that time to describe the use of photons in ways analogous to the use of electrons [4].

In the next decade companies started to install the first underground fibers for data transmission, even in metropolitan areas. It was the beginning of the *Optical communications*. While the cheap production of optical fibers based in silica (SiO_2) encouraged the research in fibers, the advances in microelectronics with the establishment of the *Silicon Valley* instigated researchers to explore the integration of the light waveguides into the Si platform. In 1985, the first silicon-on-silicon waveguide was demonstrated [5]. In the following years silicon-on-sapphire [6] and silicon-on-germanium [7] alternatives were proposed to improve the devices. This began the study in the late 80s of passive and active waveguide-based devices such as switches and modulators, and many fundamental studies dealing with basic building blocks of the silicon photonics technology.

The 90's arrived and with them the first concept of chip integrating optoelectronic devices, transistors and Si waveguides on the same substrate by Abstreiter and Soref [8, 9]. In this decade, the erbium-doped fiber amplifier [10] and the quantum cascade lasers [11] were also invented, two fundamental pieces in the actual use of photonic devices. Moreover, the revolution in computing brought a lot of advances in the experimental techniques and the first bonding techniques were developed, enabling the access to different functionalities not available in the native silicon-on-insulator (SOI) platform [12].

More recently, the idea of integrating photonic structures with a real microchip, has been deeply studied, especially by the research teams of big technological companies like Intel or IBM. While the short-term proposal is the use of light to interconnect different microelectronics systems, specific processing tasks could be in the future directly allocated to photonic components. Probably the most notorious examples of this is the generation of entangled photon-pairs, with applications in quantum computing [13], quantum key distribution [14], teleportation [15], metrology [16], etc. The possibility of integrating these sources directly into compact chips is thanks to the photonic nonlinear components and is a key milestone in the rise of photonic technologies.

While the demand of new functionalities for photonic devices increased, notably for nonlinear processes, researchers had to focus on finding the best materials to satisfy those requirements. III-V semiconductors materials are among the most promising ones. These are not limited to binary combinations III-V elemental compounds but they also include alloys and non-stoichiometric compounds, opening a huge window of possible materials with different characteristics like direct or indirect band-gap, different refractive indices and transparency windows. In this thesis, we will focus on the use of gallium phosphide, GaP, and take advantage of its large indirect band gap to avoid two-photon absorption and its large nonlinear susceptibility coefficient.

So far, a very large set of photonic devices has been investigated. The most promising of these devices may be the whispering gallery mode (WGM) resonator. Offering a high photonic confinement, the possibility of small modal volume and the integration with other photonic components make them ideal for nonlinear processes in integrated photonics where high power sources are not available. Several demonstrations of integrated nonlinear devices using III-V WGMs resonators were already reported, especially for second harmonic generation, the doubling of the frequency of an electromagnetic wave, for example with AlN microrings [17] or GaAs microdisks [18, 19, 20].

The objective of this thesis is to investigate different aspects of nonlinear integrated devices based on GaP material, focusing on two processes: the use of GaP microdisks to perform second harmonic generation in the near infrared regime and the use of IR waves to produce THz using difference frequency generation. This work is divided in 5 chapters:

- Chapter 1 introduces the background of the subject, explaining the theoretical basis of photonic confinement, both in straight rectangular waveguides and in circular resonators, introducing the whispering gallery modes. The nonlinear processes are also presented, for both the second harmonic generation and the THz generation. The notion of phase-matching is shown, especially in the case of GaP circular microresonators. Finally we briefly review the state-of-the-art and thesis objectives for the aforementioned applications.

- In chapter 2 we present the vertical evanescent coupling strategy for the wavelength converter based on a GaP microdisk. We study the coupling process to address its impact on the efficiency of the device. We investigate the propagation constant mismatched couplers as well as the control over the depletion or non-depletion regime of the nonlinear conversion.
- In chapter 3 we demonstrate that the origin of the specific phase-matching selection rules in circular microresonators is due to the Berry phase acquired by the transverse spin angular momentum components of the electromagnetic fields. We obtain the general form of the nonlinear susceptibility in the novel basis so that the selection rule can be easily comprehended for any material. We also detail the specific case of the zinc-blende materials like GaP.
- Chapter 4 is about the technological processes needed to fabricate the devices designed in chapter 2. We study different bonding techniques to obtain GaP membranes on insulator. We design electron beam lithography mask for the photonic components and analyse the requirements and problems in actual fabrication. Lastly, using different approaches we also explore the encapsulation of the components to prepare the two-level configuration.
- Finally, in chapter 5 we investigate and propose a novel approach for integrated THz generation in the Reststrahlen band. We show how to use surface phonon

polariton modes to guide THz waves and how an unusual crystal alignment is suited for this configuration. We propose the use of a GaP stripe as the medium for this THz generation, obtaining theoretical efficiencies comparable to those of the state-of-the-art.

Chapter 1

Nonlinear Integrated Photonics

1.1 Integration Technology of III-V Photonic Circuits

Integrated photonics now faces the challenge of substituting or even going beyond some functionalities of microelectronics. The industry demands the integration of new capabilities into compact microchips for a range of applications that goes from optical interconnects [21, 22] to quantum technologies (figure 1(a)) [23, 24]. To do so, a whole set of active and passive functions are needed: signal processing devices [25]; sensors [26]; light sources [27]; wavelength converters [28]; optical memories [29]; etc. All of these technologies are possible thanks to the development of technological processing at the nanoscale to produce small footprint devices.

Many of the functionalities available are driven by the specific properties of the material chosen for the device. The main photonic platform is based on silicon (Si) due to the expertise inherited by microelectronics. Silicon is a very mature platform with a lot of fabrication and process flow studies developed for Complementary Metal-Oxide-Semiconductor (CMOS) technology. Silicon on Insulator (SOI) platform has been widely used when designing and developing photonic integrated circuits (PICs) due to the high refractive index contrast between Si and air/silica, giving a very good confinement for light.

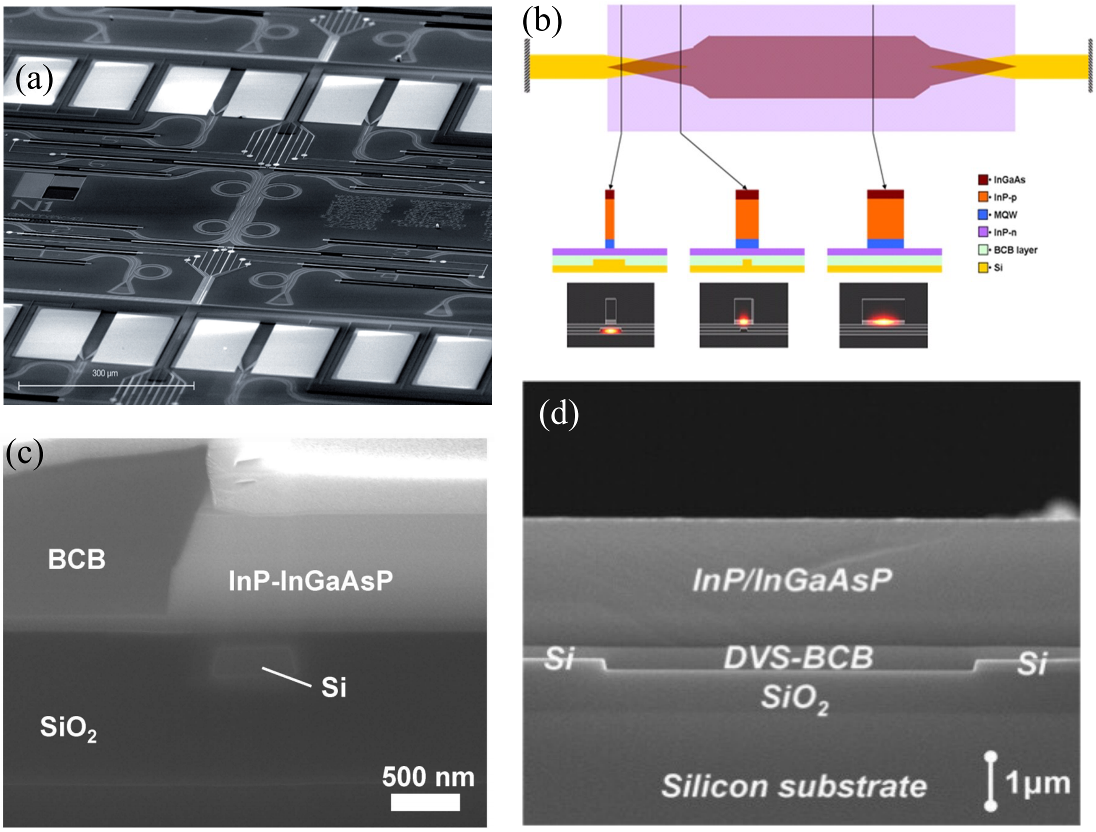

Figure 1.1: (a) Integrated photonic CNOT quantum gate after the final fabrication step [30]. (b) Top view, cross sections and mode profiles of the III-V/SOI laser using tapered waveguide and active medium [31]. (c)Edge of an InP/InGaAsP disk and the SOI waveguide [32]. (d) Cross-section of an InP/InGaAsP device and a BCB planarizing bonding layer [33].

But for some specific components, nonlinear effects are required [34]. Even if Si has a well-studied set of applications in the nonlinear regime [35], when approaching the visible spectrum ($< 1.1\mu m$) the absorption limits its use (figure 1.3). Furthermore, Si is a centro-symmetrical material which makes it not suitable for second-order nonlinear optics under normal conditions.

To fill this gap, new materials, mainly III-V semiconductors, are proposed as great alternatives. With high second-order nonlinear susceptibility (χ^2), they enable efficient nonlinear processes. They also exhibit large refractive indices, allowing light confinement to maximize the nonlinear effect. In these semiconductors a large variety of band-gaps is found, some of them with indirect band-gap, convenient to minimize losses, some other with direct band-gaps adapted for laser emission integrated monolithically [36]. But the problem with III-V semiconductors comes from the fact that they usually cannot be easily grown on silicon wafers due to the lattice parameter mismatch, differences in the thermal expansions coefficients and structural issues in growing a polar material on a nonpolar substrate [37]; this limits the wafer-scale production to very specific cases. Different strategies were proposed to improve the monolithic integration of III-V semiconductors on silicon, such as the deposition of thick buffer layers to burry defects created at the hetero-interface using Molecular Beam Epitaxy (MBE) or Liquid Phase Epitaxy (LPE) [38]. Chemical vapour deposition techniques are also used for this task like Metal-organic Chemical Vapour Deposition (MOCVD) method to grow some III-V like GaAs/InGaAs on Si [39] or Low Pressure Chemical Vapor Deposition (LPCVD) to grow Si_3N_4 (figure 1.2 (b)).

At research level, there are several strategies to fabricate photonic devices on a III-V/Si platform. The flip-chip method [12], where some pads are used to solder the Si and the III-V layer, is now commonly used in photonics. In the last years, very good results have been obtained with the use of different bonding techniques. In direct wafer bonding, also called fusion bonding, the two wafer surfaces are directly pressed together with a very precise alignment and then heated to bond them. In laboratories, more accessible solutions are used such as the use of resins as an adhesive [40]. Most of the times the chosen compound is benzocyclobutene (BCB)(figure 1.1 (b)). A thin layer is deposited at the surface, spin coating is used to planarize the structure, allowing the bonding of already patterned structures (figure 1 (c) and (d)). The low refractive index of BCB makes it appropriate as a cladding material for optical confinement and a neutral component for the evanescent photonic coupling between different layers of the photonic integrated circuit (PIC). Then a thermal treatment of no more than 300 °C bonds the surfaces, this will limit the maximum temperature that can be reached during the post-processing steps of this kind of samples. A detailed discussion on these bonding techniques applied to our samples is provided in chapter 4.

But so far, most of the demonstration of advanced nonlinear photonic components have been made in suspended configurations (figure 1.2). These configurations are interesting to maximize the photonic confinement thanks to the low refractive index of air. But when trying to implement functionalities into actual chips, suspended configurations are way too fragile to withstand real operation of the devices although some commercial solutions exist but with a very limited lifetime.

1.2 Choosing Gallium Phosphide as a Nonlinear Photonics Platform

Gallium phosphide has been widely used in the industry of semiconductors [45]. Its indirect band-gap of $2.26eV$ limits its use as a light source compared to other

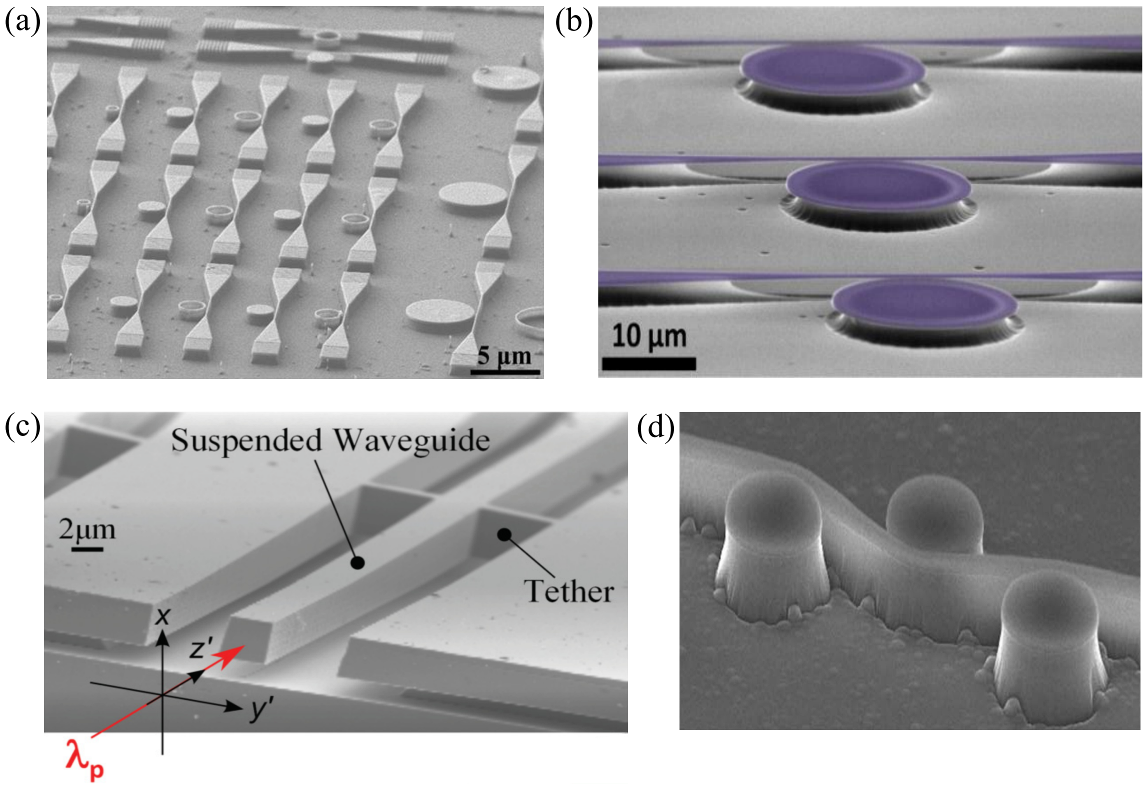

Figure 1.2: (a) Array of GaP resonators on a etched diamond substrate [41]. (b) SEM image of Si_3N_4 disk resonators coupled to a suspended waveguide [42]. (c)InP suspended waveguide on InGaAs for THz generation [43]. (d) Waveguide-coupled disk resonators of GaP-on-diamond [44].

semiconductors like InP, GaAs or GaN. But when thinking about nonlinear devices, this indirect band-gap is an advantage, reducing the photon absorption even when approaching the value of the band-gap, at the wavelength of 549 nm and the two-photon absorption when working in the IR (figure 1.3).

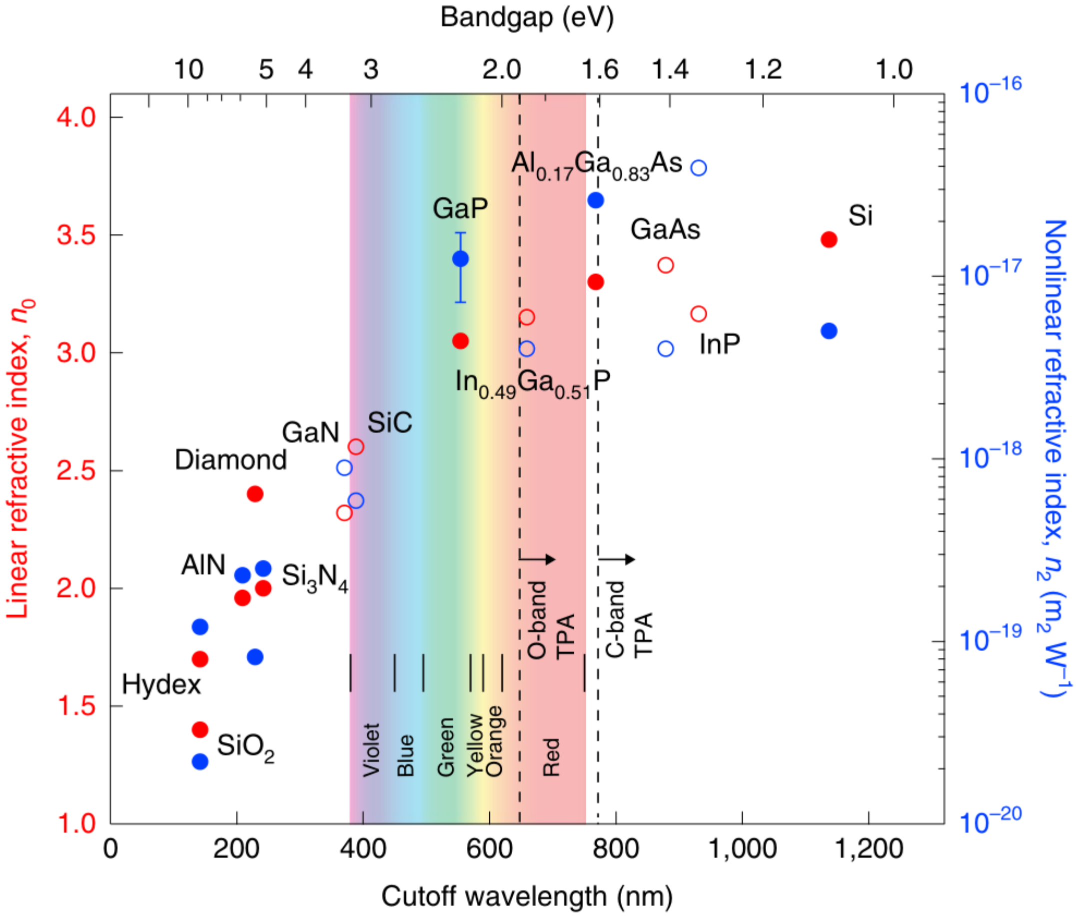

Figure 1.3: Linear (red) and nonlinear (blue) refractive indices of various integrated photonics materials, plotted versus band-gap energy and its corresponding wavelength. [46].

The crystalline structure of GaP is zinc-blende (ZB). The unit cell has a face-centered cubic (FCC) structure of gallium atoms where half of the tetragonal sites are occupied by phosphorus atoms. The space group of this crystal structure is $F\bar{4}3m$. One of the characteristics of this group is the existence of the $\bar{4}$-symmetry, enabling $\bar{4}$ quasi-phase-matching for second-order nonlinear processes [47] as it will be discussed in section 1.3.3. This is complemented with one of the highest nonlinear susceptibility of integrated photonics materials, $50\,\mathrm{pm\,V^{-1}}$ in the O-band for second-order susceptibility and $10^{-17}\,\mathrm{m^2\,W^{-1}}$ for third-order nonlinear refractive index, as shown in figure 1.3.

The lattice parameter for GaP is $5.45\,\mathrm{Å}$, the closest to Si ($5.43\,\mathrm{Å}$) among all binary III-V semiconductors, with just a $0.36\,\%$ mismatch. This makes of GaP one of the best candidates for low defect epitaxial growth on Si, with the perspective of technological scalability.

Another advantage provided by this GaP/Si platform is the chemical contrast between GaP and Si. The experimental processes for making integrated photonic circuits are based on lithography and etching techniques. A good difference in the chemical reactivity between Si and GaP allows an easy and affordable procedure to remove one of the components while the other remains inert.

1.3 Photonic Confinement

Photonic confinement is the essential ingredient of integrated photonic circuits as it allows guiding light towards devices and even enhancing light-matter interaction to increase the efficiency of the nonlinear processes. To confine electromagnetic fields we need to introduce refractive (n) discontinuities between a high refractive index region, called *core*, and a surrounding lower refractive index region called *cladding*. When total internal reflection condition is reached, light remains confined within the core region; the higher the contrast between refractive indices, the stronger the confinement. Typical cladding materials in semiconductors photonics technology are SiO_2 and BCB, with refractive indices of 1.44 and 1.54 at 1.55 µm. This makes semiconductors (particularly Si but also GaP) very good materials for submicrometer-size devices due to their large refractive index (i.e. $n_0 > 3$ as shown in figure 1.3).

1.3.1 Dielectric Waveguides

For the sake of conciseness, we will focus our analysis to rectangular waveguides. In PICs, most of the waveguides do not show a square section and confinement perpendicular to the PIC plane (vertical direction in the following) is tighter than the one in the plane (so-called lateral confinement). Hence, we adopt the convention of the slab waveguide (i.e. a 2D planar waveguide) to describe the polarization state of the confined modes. In the following sections, we will consider propagation along z direction, x and y being the horizontal and vertical axis respectively.

- Transverse Electric (TE) modes have their main electric field component in the slab plane, perpendicular to the propagation direction, so that all fields components can be derived from the longitudinal magnetic field component H_z from Maxwell's equations.

- Transverse Magnetic (TM) modes, have their main magnetic field component in the slab plane, perpendicular to the propagation direction, so that all fields components can be derived from the longitudinal electric field component E_z from Maxwell's equations.

In some cases, lateral and vertical confinements become comparable together so that neither E_z nor H_z completely vanishes, making all modes hybrid. We will however adopt the usual TE/TM PIC nomenclature instead of E^x/E^y in Goell's notation [48].

There are several methods to semi-analytically obtain the profiles of propagating modes like Marcatilli's method or Effective Refractive Index method but nowadays computational methods are the usual way to go, in particular the Finite Element Method (FEM) and the Finite-Difference Time-Domain (FDTD). Both methods are used in this thesis to obtain the modes supported by a waveguide.

Even if we will not solve semi-analytically the equations that describe the modes, there are some particularities that can be deduced without solving them. We can write the Helmholtz's equation in a homogeneous medium as a function of the longitudinal components:

$$\begin{gathered} \frac{\partial^2 E_z}{\partial x^2} + \frac{\partial^2 E_z}{\partial y^2} + (k_i^2 - \beta^2) E_z = 0 \\ \frac{\partial^2 H_z}{\partial x^2} + \frac{\partial^2 H_z}{\partial y^2} + (k_i^2 - \beta^2) H_z = 0 \end{gathered} \tag{1.1}$$

And the equations for all transversal components as a function of the longitudinal ones:

$$(k^2 - \beta^2) E_x = i\beta \frac{\partial E_z}{\partial x} + i\omega\mu_0 \frac{\partial H_z}{\partial y} \tag{1.2}$$

$$(k^2 - \beta^2) E_y = i\beta \frac{\partial E_z}{\partial y} - i\omega\mu_0 \frac{\partial H_z}{\partial x} \tag{1.3}$$

$$(k^2 - \beta^2) H_x = i\beta \frac{\partial H_z}{\partial x} - i\omega\varepsilon \frac{\partial E_z}{\partial y} \tag{1.4}$$

$$(k^2 - \beta^2) H_y = i\beta \frac{\partial H_z}{\partial y} + i\omega\varepsilon \frac{\partial E_z}{\partial x} \tag{1.5}$$

where k is the propagation vector, defined as $k_i = n_i\omega/c$ and β the propagation constant, that is the same in every part of the space[1]. Solving the equations 1.1 in every region with the same n_i gives the profile of the different modes. The solution to those equations are only possible for discrete values of $(k^2 - \beta^2)$, being the eigenvalues supported modes that satisfy both total internal reflection and wavefront propagation.

For 2D confinement, each eigenvalue is associated to a mode associated with a set of two indices, the horizontal and vertical orders. These indices describe the number of nodes in the horizontal and vertical direction respectively. The notation for the modes is thus given by the two indices and polarization. This makes the fundamental modes TE_{00} and TM_{00}. The higher the order of the mode, the more power propagates outside the core. Higher order modes thus feature smaller effective refractive index. The modal dispersion (the variation of β with ω) is thus different for each mode depending on the geometry of the waveguide. It can be calculated from the field continuity relations and is presented in figure 1.4 for a rectangular waveguide.

It is important to note that the longitudinal electric field components (z components) are non-zero for both polarizations. Even though these components do not contribute to the Poynting vector, they carry energy and can couple to produce nonlinear effects. These longitudinal electric field components are proportional to the first derivative of the transverse magnetic field component in the transverse plane. Thus, the stronger the mode is confined, the more energy is stored in the longitudinal electric field component. The contribution of the longitudinal component of the field in second-order processes has long been ignored in the literature in favor of the transverse components of the field even when using WGMs [47] but was recently evidenced experimentally in InGaP waveguides [49]. The use of this longitudinal component is in fact, the principle behind the THz generation scheme proposed in chapter 5.

---

[1] It is related to the effective refractive index through the equation $\beta = n_{eff} 2\pi/\lambda$

From this introduction to optical confinement, one can already imagine the difficulties encountered in designing hybrid IR to THz nonlinear devices that should both confine waves in the n-IR domain (with wavelength in the μm range) and waves in the THz range (with wavelengths from dozens to a hundred of µm). This, in addition to the issue of absorption losses for all III-V in the far-IR regime, imposes the use of new strategies like the use of surface phonons polaritons to guide the propagation of EM waves, making possible to guide THz waves with waveguides of just a few hundreds of nanometres of width and height. This will be further discussed in chapter 5.

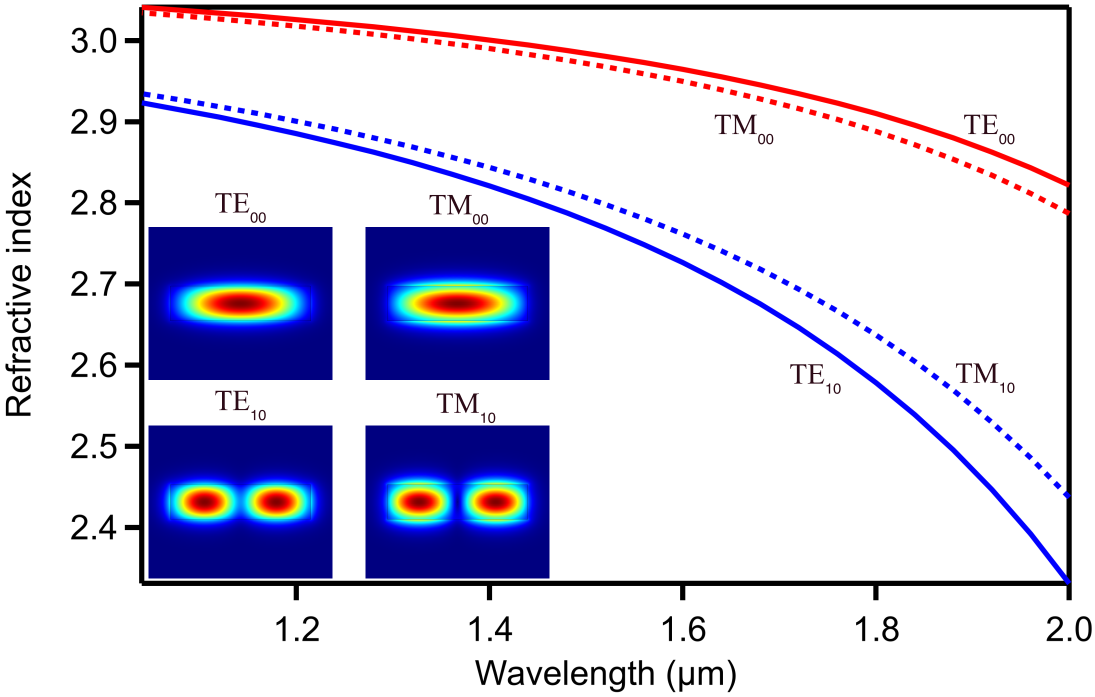

Figure 1.4: Dispersion curves and mode profiles for the first four modes of a stripe waveguide.

1.3.2 Whispering Gallery Modes

The study of the whispering gallery modes (WGMs) starts at the end of XIX^{th} century when Lord Rayleigh tried to explain a curious phenomenon in Saint Paul's cathedral. Small sounds produced under the dome could be heard far from the source if you were close to dome's wall, suggesting that the sounds were propagating along the curvature of the dome. Sound intensity decays usually with the square of the distance while in the gallery of whispers, the decay was linear. Rayleigh did experiments with candles to describe precisely the propagation of sound waves and deduced that these were confined to a close distance from the wall, explaining why whispers could be heard from far away. Because of that, Rayleigh named those waves Whispering Gallery Modes [50].

In the late XX^{th} century, this effect was used to build circular microresonators for optics. While linear cavities have a system of mirrors where the light is trapped by the reflection at the borders of the cavity, circular resonators trap light by total internal reflection in the edge of the disk/cylinder/toroid/sphere, making a resonant cavity (figure 1.5(a)). This causes a high confinement of light in the eigenmodes of the cavity, giving modal volumes of just a few μm^2 in small microresonators. This effect makes WGMs very interesting for integrated nonlinear photonics, where the use of powerful sources is not available.

In the same way that we defined two different polarization modes for waveguides, we will distinguish between TE and TM WGMs (fig 1.5(b) and (c)). In cylindrical coordinates, we have:

- Transverse electric: The electric field is in the microdisk's plane and the magnetic field is along z plane. Then, the only non-zero components are E_r, E_φ

and H_z

- Transverse magnetic: The electric field is the vertical direction, z and the magnetic field in the microdisk's plane. Here the non-zero components are H_r, H_φ and E_z.

In microdisks, the vertical confinement is many times higher than the horizontal one. We can thus use the *effective refractive index method* in the vertical direction, which implies obtaining the eigenmodes of a slab of the same thickness as the microresonator, reducing the problem to a 2D flat disk with a set of effective refractive indices (n_{eff}), obtained for each eigenmode in the slab and labelled by a planar confinement order.

Inserting the effective refractive index into the wavevector k, we write the Helmholtz equation in cylindrical coordinates for the two states of polarization:

$$\begin{aligned} (\frac{\partial^2}{\partial r^2} + \frac{\partial}{r\partial r} + \frac{\partial^2}{r^2\partial\varphi^2} + k^2)H_z(r,\varphi) = 0 \text{ for TE} \\ (\frac{\partial^2}{\partial r^2} + \frac{\partial}{r\partial r} + \frac{\partial^2}{r^2\partial\varphi^2} + k^2)E_z(r,\varphi) = 0 \text{ for TM} \end{aligned} \tag{1.6}$$

we can separate variables and see the azimuthal and radial contributions independently. The equations corresponding to the TE polarization are:

$$(\frac{\partial^2}{\partial\varphi^2} + m^2)H_z(\varphi) = 0 \tag{1.7}$$

$$(\frac{\partial^2}{\partial r^2} + \frac{\partial}{r\partial r} + k^2 - \frac{m^2}{r^2})H_z(r) = 0 \tag{1.8}$$

where m is an integer, that corresponds to the number of optical cycles in one revolution. This number characterizes the propagation of the WGMs and is called *azimuthal* *order* (figure 1.5(a)). Like for the rectangular waveguide, the solutions for equation 1.8 are restricted to eigenvalues of k. The solutions for the radial dependence are characterized in the radial component are defined by their *radial order* (figure 1.5(d) and (e)).

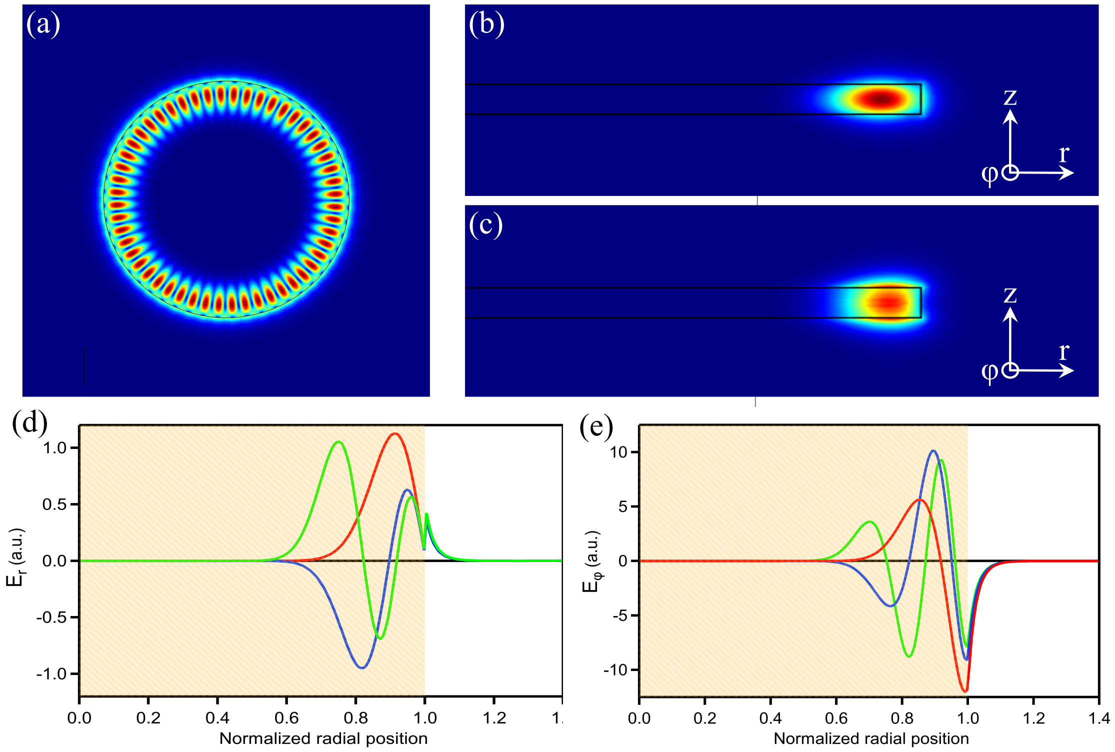

Figure 1.5: (a) Top view of the electric field of a WGM. (b) and (c) Cross-section of the electric field of a TE and TM WGMs respectively. (d) Radial component of the electric field for TE WGMs with radial numbers equal to 1 (red), 2 (blue) and 3 (green). (e) Azimuthal component of the electric field for TE WGMs with radial numbers equal to 1 (red), 2 (blue) and 3 (green).

Every WGM is thus defined by an azimuthal, a radial and a planar order for each polarization. Like in the waveguides, each of these modes will have a different dispersion relation and different fields distribution map.

A particularity of the WGMs, is that all of the k solutions obtained in the

Helmholtz equation 1.8, are complex values. The real part defines the wavelength of the resonance:

$$\lambda = \frac{2\pi}{Re(k)} \tag{1.9}$$

The imaginary part characterizes the bending losses. Indeed, all WGMs are intrinsically lossy and their *quality factor*, the characteristic number of optical cycles before confined energy is lost to the radiation continuum, is thus limited by:

$$Q_{factor-bending} = \frac{Re(k)}{2Im(k)} \tag{1.10}$$

One can calculate the dependence of the bending Q_{factor} with the refractive index contrast and the radius of the disk as presented in figure 1.6. For small microdisks, the Q_{factor} is strongly reduced due to the curvature [51]. This effect is even higher in very thin microdisks, where the n_{eff} is small, reducing the refractive index contrast. The interest of this kind of devices in nanophotonics is that this effect is partially compensated by very small mode volumes, very convenient to increase the efficiency of the nonlinear processes.

In this work, we will work with GaP microdisks embedded in a dielectric cladding (silica or BCB polymer), with dimensions optimized for stric $\bar{4}$-QPM as reported in [52] (3.4 µm of radius and 180 nm of thickness). For such parameters, the effective refractive index of a GaP slab is 2.15 at 2 µm of wavelength for TE modes so that the index contrast n_1/n_2 in 1.6 is around 1.5 and the normalized radius about 23. This makes the bending Q_{factor} no larger than 500. The same calculation performed for TM modes around 1 µm of wavelength gives bending Q_{factor} in the range of 10^6.

In addition to the bending losses, there are other contributions to the total *intrinsic quality factor* that groups all the sources of losses of an isolated microresonator,

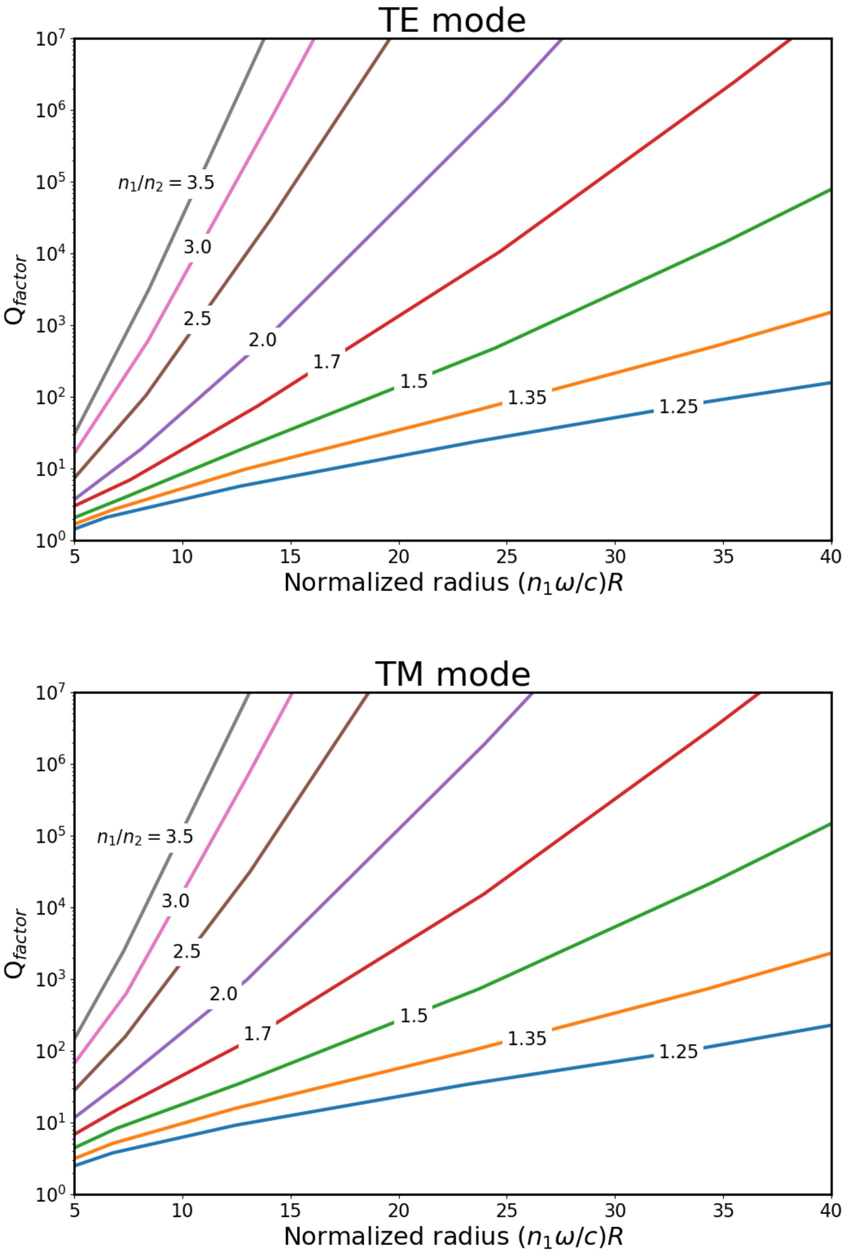

Figure 1.6: Quality factor of the lowest radial order TE and TM whispering gallery modes of a microdisk of effective refractive index of n_1 and a cladding of n_2 versus the normalized radius $(n_1\omega/c)R$. The family of diagonal lines represents different refractive index contrast (n_1/n_2) (figure modified from [51]).

without external coupling:

$$\frac{1}{Q_{intrinsic}} = \frac{1}{Q_{material}} + \frac{1}{Q_{surface}} + \frac{1}{Q_{scattering}} + \frac{1}{Q_{bending}} \tag{1.11}$$

corresponding to material (absorption), surface roughness, scattering and bending losses respectively. If we also add the contribution of an external coupler to excite the different modes we use the *loaded quality factor*:

$$\frac{1}{Q_{loaded}} = \frac{1}{Q_{coupling}} + \frac{1}{Q_{intrinsic}} \tag{1.12}$$

where $Q_{coupling}$ is the quality factor corresponding to the interaction between the resonator and the waveguide. In the following we will study the relevance of Q_{factor} for wavelength conversion in circular microresonators.

1.4 2^{nd} Order Nonlinear Processes

For the design of these photonic integrated devices, we need a set of nonlinear processes capable of wavelength conversion [34]. Second-order nonlinear processes appear when non-centro-symmetric materials are exposed to an intense electric field, producing a nonlinear response (amorphous solids and fluids have a zero second-order nonlinear susceptibility). If we express the response of the material to a sufficiently large electric field $E(t)$ as a power series under the assumption of an instantaneous response of the medium to the electric field applied, the macroscopic polarization $P(t)$ reads as:

$$P(t) = \varepsilon_0[\chi^{(1)}E(t) + \chi^{(2)}E^2(t) + \chi^{(3)}E^3(t) + \ldots] \tag{1.13}$$

where ε_0 is the permittivity of free space. $\chi^{(1)}$ corresponds to the linear susceptibility, $\chi^{(2)}$ to the second-order susceptibility, exclusive of non-centrosymmetric materials, and $\chi^{(3)}$ is third order susceptibility. In this thesis we will only focus on the nonlinear processes of second-order so all mentions to polarization onwards will refer to the *second-order polarization.*

Since the electric field and polarization are vectors, the $\chi^{(2)}$ susceptibility is a 3-rank tensor. It can be simplified thanks to the Kleinman symmetry condition. It is usually written as:

$$\chi^{(2)} = 2 \begin{pmatrix} d_{11} & d_{12} & d_{13} & d_{14} & d_{15} & d_{16} \\ d_{16} & d_{22} & d_{23} & d_{24} & d_{14} & d_{12} \\ d_{15} & d_{24} & d_{33} & d_{23} & d_{13} & d_{14} \end{pmatrix} \tag{1.14}$$

for electric fields written in the cartesian basis where x, y, z correspond to [100], [010], and [001] axes of the crystal.

Such a nonlinearity of the material response is mainly due to the electronic response when the process occurs in the visible and near infrared (n-IR) spectral ranges. However, as we approach the frequencies of the vibrational modes of the lattice, light begins to couple with phonons. This range is called *Reststrahlen Band*, and for III-V semiconductors it lies between 4 THz and 15 THz. There, the susceptibility becomes a combination of the electronic ($\chi^{(2)} = \varepsilon_\infty - 1$) and ionic contributions, the later can be written as

$$\chi^{(i)} = \varepsilon_0 - \varepsilon_\infty \tag{1.15}$$

A more detailed analysis about the nonlinear susceptibility at phonon frequencies will be given in chapter 5.

Taking only second-order terms of equation 1.13 we can write the interaction of the two beams at frequencies ω_1 and ω_2, leading to:

$$\tilde{P}(t) = \varepsilon_0 \chi^{(2)}[E_1^2 e^{i2\omega_1 t} + E_2^2 e^{-i2\omega_2 t} + 2E_1E_2 e^{-i(\omega_1+\omega_2)t} + 2E_1E_2^* e^{-i(\omega_1-\omega_2)t} + c.c.] \\ + 2\varepsilon_0\chi^{(2)}[E_1E_1^* + E_2E_2^*] \quad (1.16)$$

This general expression gathers all of the nonlinear effects of second-order: second harmonic generation (SHG) [53]; sum frequency generation (SFG) [54]; difference frequency generation (DFG) [55]; optical rectification (OR) [56]. We can write the expressions of the polarization for each physical process.

$$\begin{aligned} P(2\omega_1) &= \varepsilon_0\chi^{(2)}E_1^2 \quad (SHG) \\ P(2\omega_2) &= \varepsilon_0\chi^{(2)}E_2^2 \quad (SHG) \\ P(\omega_1+\omega_2) &= 2\varepsilon_0\chi^{(2)}E_1E_2 \quad (SFG) \\ P(\omega_1-\omega_2) &= 2\varepsilon_0\chi^{(2)}E_1E_2^* \quad (DFG) \\ P(0) &= 2\varepsilon\chi^{(2)}(E_1E_1^* + E_2E_2^*) \quad (OR) \end{aligned} \quad (1.17)$$

In this thesis, we will only consider two of these processes: SHG to perform wavelength conversion from n-IR to visible spectral range and DFG to produce THz frequencies from mid-IR waves or from IR waves in the telecom band. From here onwards, when describing the DFG processes, the notation of the generated frequency will be ω_{THz} since the only objective of those processes in this thesis is the generation of THz waves.

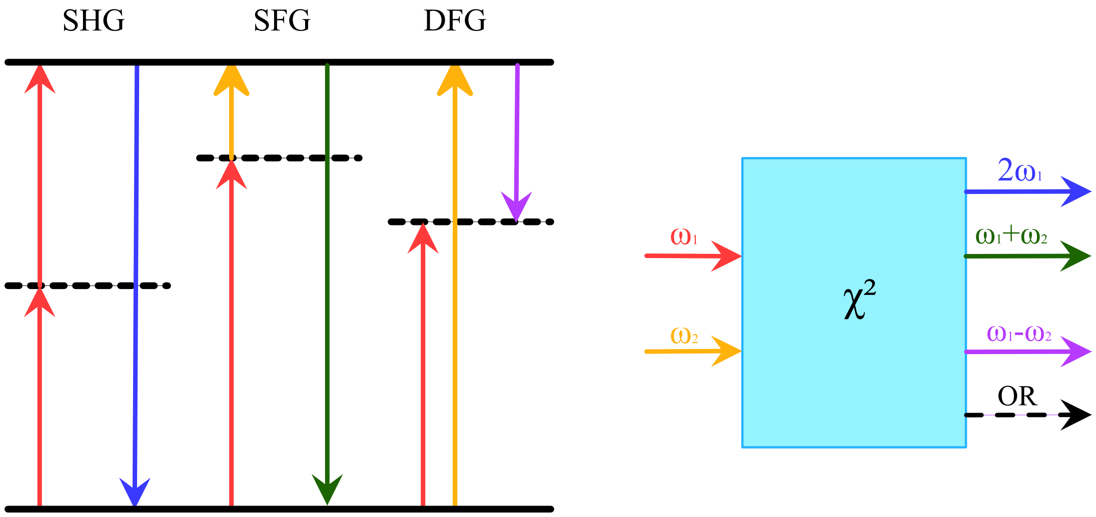

Figure 1.7: Schematic representation of the different second-order processes and their energy levels.

1.4.1 Second Harmonic Generation

The process of second harmonic generation was the first nonlinear effect observed [57]. Schematically illustrated in fig 1.7, taking a fundamental frequency ω, it doubles its frequency by interacting with a material with a non-zero $\chi^{(2)}$, the process can be seen as destroying two photons of the fundamental frequency and creating one photon at frequency 2ω.

Mathematically, we can extract the general expression of the nonlinear polarization for the SHG process from equation 1.17. We restrict the problem to linear propagation along z direction and use the slowly varying envelope approximation to write:

$$\frac{\partial E_{2\omega}(z)}{\partial z} = \frac{i4\pi\omega^2}{c^2 k_{2\omega}}\chi^{(2)} E_\omega(z)^2 e^{-i\Delta kz} \tag{1.18}$$

where Δk is the wavevector mismatch $k_{2\omega} - 2k_{\omega}$ as $k = \frac{n\omega}{c}$.

This process allows a convenient and easy generation of coherent radiation in the visible and n-IR ranges by frequency doubling thanks to the large choice of sources available between $1 - 2\mu m$. The efficiency of this process can be defined quantified in two different ways. The conversion efficiency ($\eta_{conv} = P_{out}/P_{in}^2$) refers to the coefficient of the quadratic evolution of the output power P_{out} as a function of the input power. This is the value usually used in the literature to discuss nonlinear process efficiency but its usefulness can be criticized when going beyond the regime of non-depletion of the pump. The device efficiency ($\eta_{dev} = P_{out}/P_{in}$) on the contrary, allows to assess more easily the ratio of optical power converted from a frequency to the other and is thus well suited to the description of devices, having in mind that it is itself a function of the input power. More details about efficiency and the role of coupling into it are given in chapter 2.

1.4.2 Difference Frequency Generation

In the difference frequency generation process, represented in fig 1.7, using two pump beams of frequencies ω_1 and ω_2 we produce a photon, called idler, at frequency $\omega_{THz} = \omega_1 - \omega_2$. Here the process is different compared to SHG in the fact that only the pump photon of highest energy is annihilated while the pump beam at lower energy gets amplified, and the idler is generated. This is why depending on the purpose, the DFG process can also be called parametric amplification.

Again, we can write the general expression of the nonlinear polarization for the

THz generation from equation 1.17:

$$\frac{\partial E_{\omega THz}(z)}{\partial z} = \frac{i2\pi\omega_{THz}^2}{c^2 k_{THz}} \chi^{(2)} E_1(z) E_2(z) e^{-i\Delta kz} \tag{1.19}$$

This relation is a general description and it can be applied to pure optical DFG.

DFG process has been widely used to produce THz sources with frequencies in the range of few THz and output powers from dozens of nW to the µW scale [58]. This is one step below quantum cascade lasers (QCL) that are the main source of coherent THz radiation, going up to 4.75 THz [59], with output power in the mW regime but at the cost of cryogenic conditions, making them hardly suitable for further integration with photonic integrated circuits. DFG process has also been integrated into QCL cavities to created very compact sources with intra-cavity DFG [60].

1.4.3 Phase-matching in Nonlinear Processes

In equations 1.18 and 1.19 we introduced the term Δk, known as momentum mismatch or *phase-mismatch.* When this term is equal to zero, the intensity of the generated field increases quadratically with the propagation distance z, this is called *perfect phase-matching.* On the contrary, when a non-zero mismatch exists, the intensity of the nonlinear process evolves as a sine with distance and is thus limited to a maximum value. The distance between a maximum and a minimum of this evolution is called coherence length L_c. Traditionally, when working on macroscopic materials, perfect phase-matching was achieved by use of birefringent materials to compensate the chromatic dispersion of the material which induces different refractive indices at ω and at 2ω.

Those materials are not easily usable in integrated photonics so new strategies have been conceived for the application of nonlinear processes in integrated configurations. As detailed in the previous section, the propagation in a confined medium produces different modes, each one having a different effective refractive index. Higher order modes have a larger portion of the power propagating outside the core and therefore a smaller n_{eff}. This can be used to compensate the chromatic dispersion and thus achieve *modal phase-matching*. This method will be used for the generation of THz waves in chapter 5.

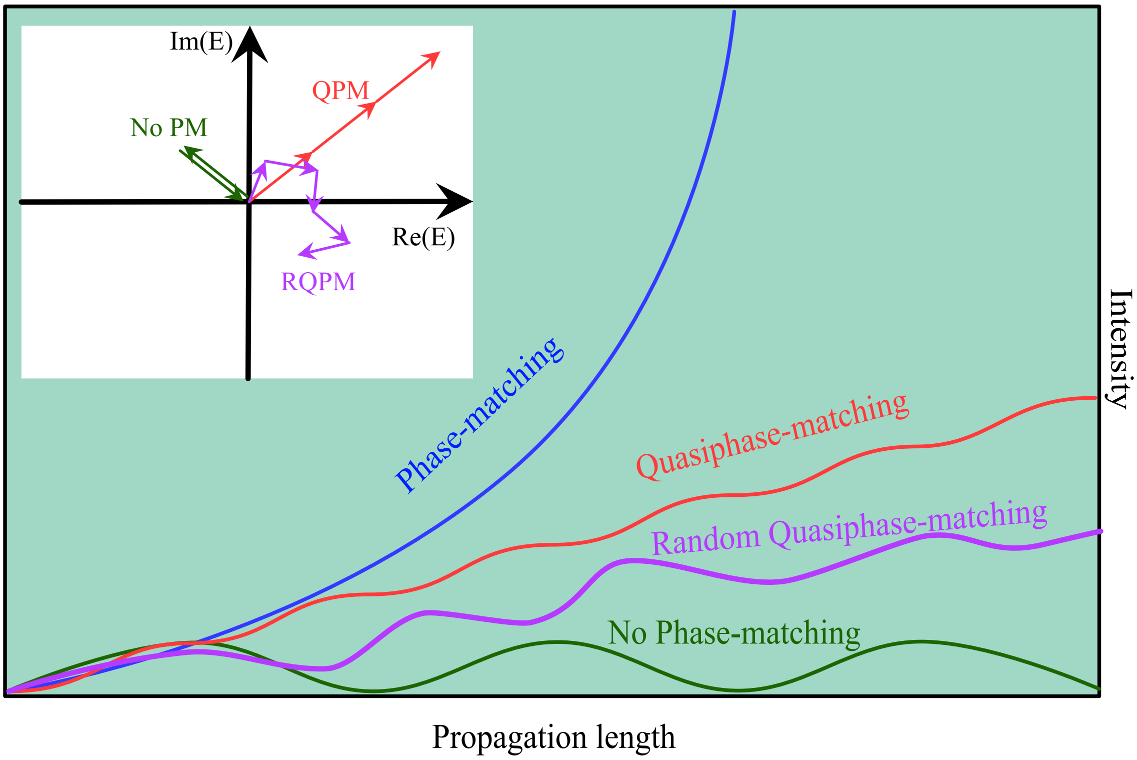

Figure 1.8: Intensity of the SHG with the propagation length for phase-matching, QPM, Random QPM and phase-mismatch. Inset: Addition to electric field without phase-matching, with QPM and with RQPM.

More recently, *quasi-phase-matching* (QPM) has been used, especially in integrated devices. Instead of having an homogeneous crystal, a material with spatially modulated nonlinear properties is used. In this case a finite phase-mismatch is allowed and the crystal polarity of the material is reversed periodically following the coherence length associated with the phase mismatch so that the nonlinear signal can go on increasing as the pump propagates along the engineered medium. This is the case of periodic-poled materials like oriented-patterned GaP (OP-GaP) [61] as presented in fig 1.8.

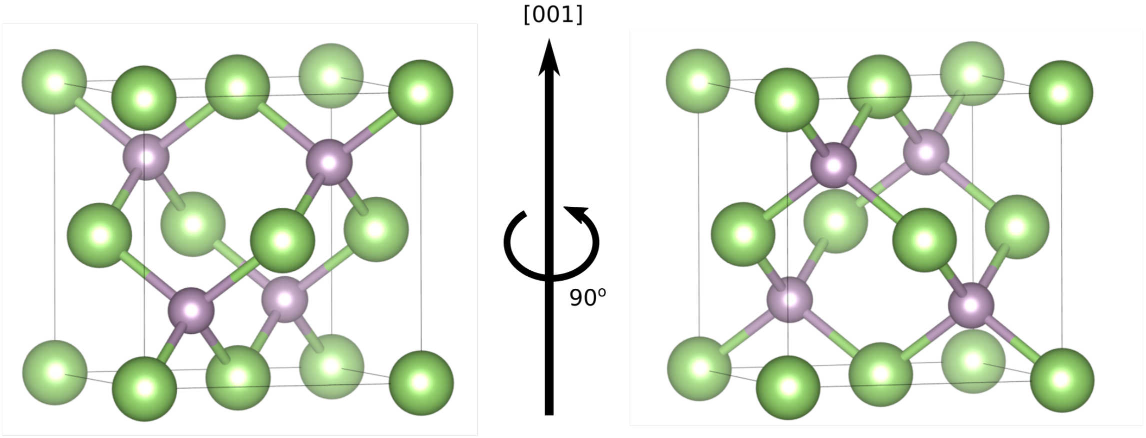

Figure 1.9: Unit cell of GaP. When rotated 90° around [001] axis the resulting cell corresponds to the reflection on the [001] plane, this changes the polarity of the crystal and thus, the sign of susceptibility.

Quasi-phase-matching can also be naturally achieved in circular microresonators when the material has a specific crystal symmetry. For example, for zinc-blende materials, like GaP, with $\bar{4}3m$ crystallographic symmetry, the rotation of 90° around [001] direction, is identical to the reflection on the [001] plane (S_4 symmetry element, figure 1.9). Hence, the nonlinear susceptibility will change sign every quarter turn in a circular resonator. This natural poling is referred as $\bar{4}$-QPM [47].

Following the work of Dumeige *et al.*, the restriction of the nonlinear susceptibility to the only non-zero coefficient d_{14} leads, in first approximation, to the limitation of the SHG process to a conversion from fundamental TE modes to TM SH modes. Then, writing equation 1.18 in cylindrical coordinates and adding the angular dependency of the nonlinear susceptibility we can describe the SHG process in materials as:

$$\frac{\partial E(2\omega)}{\partial \theta} = -\frac{i\beta_{2\omega}^2}{4m_{2\omega}\epsilon_0\epsilon_{2\omega}} E_\omega^2 [K_+ e^{i(\Delta m+2)\theta} + K_- e^{i(\Delta m-2)\theta}] \tag{1.20}$$

Where we introduced the nonlinear polarization overlap terms $K_\pm$, using the mode profiles (E_i) of the selected WGMs:

$$K_\pm = \int_0^R \epsilon_0 r^2 d_{14} (E_{r,\omega} E_{\theta,\omega} \pm \frac{i}{2}(E_{\theta,\omega}^2 - E_{r,\omega}^2) E_{z,2\omega}^* dr \tag{1.21}$$

As shown in equation 1.20, the phase-matching condition transform into a selection rule on the azimuthal number of the fundamental and SH modes: $m_{SH} - 2m_f = \pm 2$ [47]. This relation is characteristic of zinc-blende materials since other crystal symmetries feature different quanta in the azimuthal selection rule, an novel explanation of the origin of this term is given in chapter 3.

Without further recourse of the modal phase-matching, only the +2 condition can be achieved due to dispersions of the TE and TM WGMs. The conversion can be then calculated under the assumption of an undepleted pump. It strongly depends on the quality factors of both WGMs, it reads as:

$$\eta \simeq P_{IN} |K|^2 \frac{Q_{loaded/SH} Q_{loaded/f}^2}{\pi^3 m_{SH} m_f} \tag{1.22}$$

where P_{IN} refers to the pump power at the fundamental wavelength. Chapter 2 is dedicated to the optimization of this SHG conversion efficiency through the analysis of the interplay between different quality factors.

Random quasi-phase-matching is also expected in GaP microdisks grown on Si. The epitaxial growth of GaP on a non-polar substrate, like Si, produces antiphase domains (APDs), that consist in local inversions of III and V atoms in the crystal lattice. This induces a spatial distribution of opposite nonlinear susceptibility domains in the material. If the APD mean size and the average crystal polarity are well controlled, this QPM process can be competitive compared to natural $\bar{4}$-QPM (figure 1.8) [62].

Finally, the phase-matching condition can be derived differently in the case of DFG for THz generation. Since we have to meet energy conservation ($\omega_{THz} = \omega_1 - \omega_2$) and momentum conservation ($k_{THz} = k_1 - k_2$) we can write the expression:

$$\frac{\omega_{THz}}{k_{THz}} = \frac{\omega_1 - \omega_2}{k_1 - k_2} \simeq \frac{d\omega_{IR}}{dk_{IR}} \tag{1.23}$$

Since the spectral distance between pumps at ω_1 and ω_2 is short compared to their wavelengths, we can express the phase-matching condition as $n_{THz} = n_{g(IR)}$ where n_g is the *group index* ($n_g = d\omega/dk$) [63]. This means that the velocity of the envelope of the IR pumps has to be equal to the phase velocity of the THz generated. This approximation is only valid in the range of a few THz.

1.5 Positioning and Objectives

1.5.1 On the Physics of SHG in Microresonators

Second harmonic generation in circular resonator has been proposed and demonstrated by several groups. Fürst *et al.*, demonstrated SHG in a $LiNbO_3$ macroscopic resonator (R=1.9 mm) using natural phase-matching, achieving efficiencies up to 9% at 30 µW of continuous pump power [64]. They extended it later to visible and UV (317 nm) regimes [65, 66] with efficiencies of $4.6\,\%\,mW^{-1}$. Very recently and using x-cut $LiNbO_3$ to obtain natural QPM, Lin *et al.*, measured an efficiency of $9.9\,\%\,mW^{-1}$ [67].

Following a more integrated approach and using III-V semiconductors, Guo *et al.*, used AlN microrings [17], with a wavelength conversion between the telecom band and the visible regime, to demonstrate record efficiencies of $2.5\,\%\,mW^{-1}$ in undepleted regime and up to 12 % device efficiency in depleted regime with a pump power of 27 mW. Those conditions where used later by Li *et al.*, to propose the addition of a second active resonator of erbium-ion-doped silica to increase the efficiency up to 72 % with a few microwatts pumping [68]. Kuo *et al.* [18, 19, 20], demonstrated $\bar{4}$-QPM in GaAs microdisks to do wavelength conversion between 2 µm and 1 µm, coupling the resonant modes with tapered fiber. The frequency doubling of 1.58 µm in suspended AlGaAs microdisks was also reported [69]. Finally, SHG in a GaN microdisk on Si from wavelengths in the telecom band using integrated lateral coupling was demonstrated [70].

More specifically, few GaP-based nonlinear devices were proposed in the recent years. GaP ring resonators on SiO_2 have been fabricated with quality factors up to 20000 [46, 71] (figure 1.10 (a) and (b)). For wavelength conversion, coupled $\bar{4}$ and modal phase-matching were used to achieve SHG with $3.8 \times 10^{-2}\,\%\,\mathrm{mW}^{-1}$ of normalized conversion efficiency by Lake *et al.*, using a microdisk of 6.52 µm of diameter. In this case a fiber taper was used to excite the fundamental modes at 1550 nm [72] (figure 1.10 (d)). Very recently a fully integrated approach was proposed by Logan *et al.*, also doing conversion from 1550 nm to 775 nm. In this case the coupling is made by a so-called pulley waveguide. Efficiencies up to $0.4\,\%\,\mathrm{mW}^{-1}$ were reported [73] (figure 1.10 (c)).

A part of the work in this thesis aims at designing a fully integrated system consisting of a GaP-on-Si microresonator for wavelength conversion between the telecom band and the visible/n-IR, using strict $\bar{4}$-QPM. In chapter 2 we will investigate different configurations of evanescent coupling to these systems. We will address the parameters that can be tuned to control the coupling and therefore, maximize the global efficiency of the device, introducing for the first time the relation between conversion efficiency and propagation constant mismatch between waveguide modes and WGMs. In chapter 3, we will provide an original approach to describe phase-matching rules in circular resonators, independently of the material under scrutiny, unveiling the origin of the quanta present in the QPM selection rules. Finally in chapter 4, we investigate the technological challenges for the realization of nonlinear converters based on the GaP photonic platform, following the design rules introduced in chapter 2.

1.5.2 Towards THz Generation in the Reststrahlen Band

Coherent sources of THz waves are not common, especially if we talk about sources in the Reststrahlen band of III-V semiconductors, the spectrum between 5 and 15

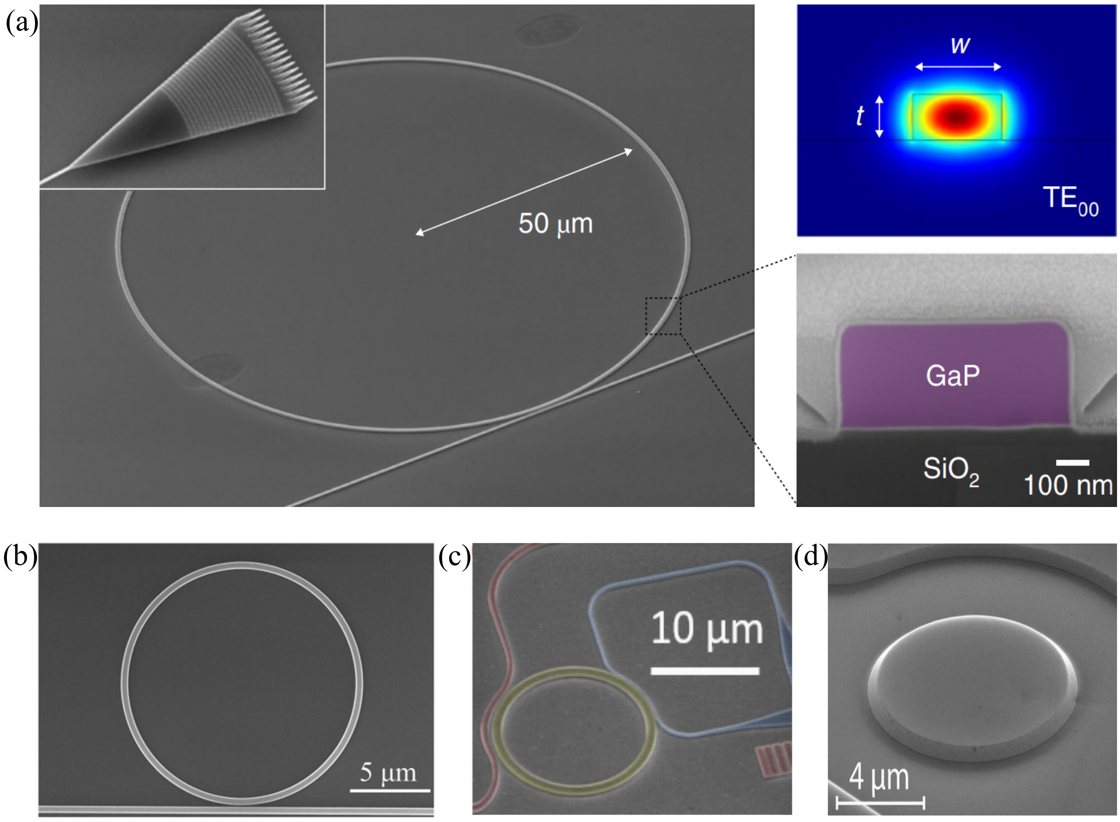

Figure 1.10: (a) SEM image of a ring resonator and the grating coupler with the cross-section and mode profile of the guide [46]. (b) Ring resonator comprising a 400 nm wide circular waveguide with a radius of 7.5 µm [71]. (c)GaP ring resonator with two independent output/input coupling pulley waveguides [73]. (d) Gallium phosphide microdisk for SHG between IR and visible regimes [72].

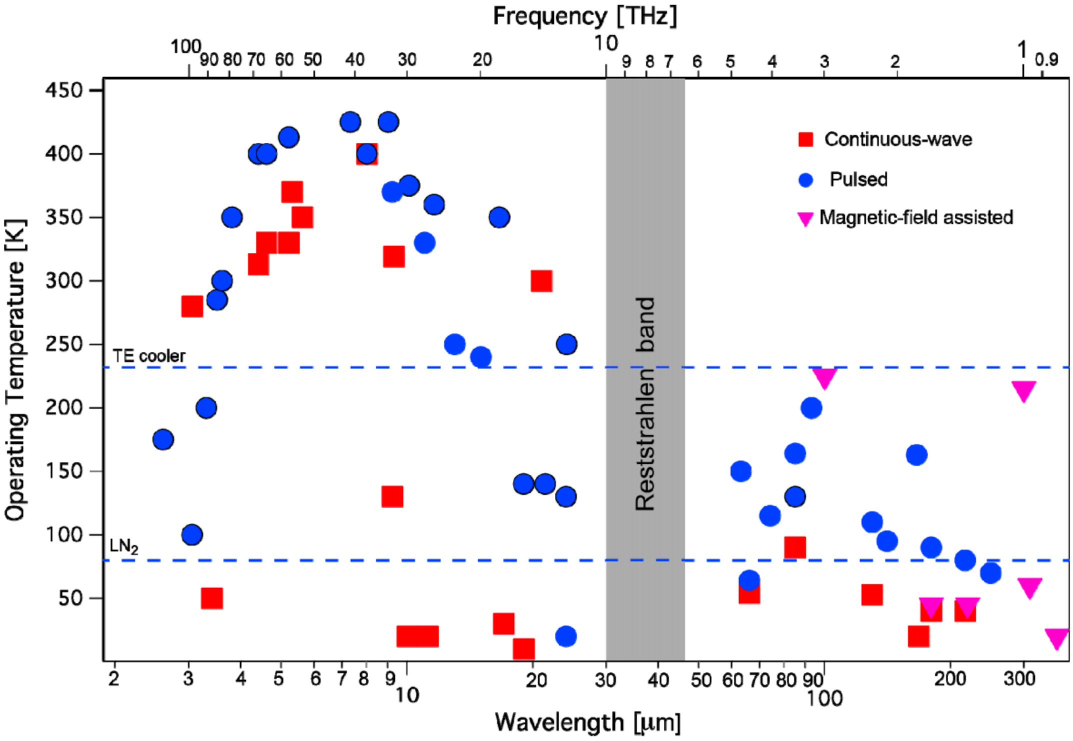

Figure 1.11: Operating temperature plot as a function of the emission wavelength for reported quantum cascade lasers [76]

THz. Quantum cascade lasers are the main source of THz waves in this range, achieving powers in the W range [74]. But most of the proposed devices need cryogenic conditions. An emission between 15-30 THz with output powers of 15 mW has been reported at room temperature [75]. Even with that, the Reststrahlen band of the semiconductors used for the QCLs remains uncovered (figure 1.11).

To cover this gap, DFG is one the most promising methods by using IR pumping waves. It has been integrated into actual mid-IR-QCL sources. Belkin *et al.*, showed THz generation at room temperature of a few hundreds of mW around 5 THz [60]. More recently the continuous wave around 2 THz of powers up to 300 μW below 200 K has been reported.

Looking at demonstrations of THz generations in III-V, the Ginzton laboratory reports on generation of 2 THz waves in planar GaAs waveguides [77, 78] and proposes the use of metallic guides to confine the THz modes while pumping in the GaAs stripe [79]. In GaP there are theoretical proposals for generating 6 THz waves with efficiencies up to $6.6 \times 10^{-4}\,\mathrm{W}^{-1}$ using collinear phase-matching [80, 63]. Using GaP rods high powers of up to 480 mW have been measured at 1.3 THz [81].

In chapter 5 we aim at exploring the generation of THz waves in the Reststrahlen band (at 11-12 THz for GaP) through DFG. We will see that this novel approach requires to consider the propagation of the THz wave in the geometry in the form of surface phonon polariton, so that specific geometries need to be developed for optimal nonlinear conversion.

Chapter 2

Design of III-V Microdisk Integration for Second Harmonic Generation

In this chapter we investigate evanescent coupling strategies for a wavelength converter based on strict $\bar{4}$-QPM microdisk resonator as first introduced by Dumeige *et al.* [47]. There, fundamental and SH modes share the same radial and planar orders, optimizing their field overlap. This specific configuration has lately been forsaken to the benefit of larger resonators, demonstrating higher quality factors and thus, considered as better qualified for efficient wavelength conversion. This chapter aims to demonstrate that the coupling strategy is a central part of the device efficiency and cannot be reduced to the sole goal of achieving critical coupling. In the following, we will investigate propagation constant mismatched couplers and demonstrate that the right coupling scheme can provide high tolerance over geometrical parameters and modal dispersion as well as the control over the depletion or non-depletion regime of the nonlinear conversion.

2.1 Integrated Evanescent Coupling Strategies

The mid-term goal of integrated photonics researchers and industry is to offer fully integrated and functional photonic devices and circuits, suitable for commercial use. The solutions have thus to be resistant enough to handle realistic operation conditions and ensure a long enough lifespan. Typically, when studying microdisks, the common coupling system is the tapered fiber, supported on the surface of the disk [18]. Tapered fibers offer an easy and cheap way to characterize microdisks, allowing some grade of tuning thanks to the possibility of repositioning the fiber aside of the resonator, finding the best position to excite a desired mode. But this flexibility comes with a cost since the difficulty of alignment, partly due to electrostatic forces, complicates the possibility of doing reproducible measurements. The impossibility of having a controlled vertical distance between the fiber and the surface of the microdisk, the round shape of the fiber and the variation of diameter from one tapered fiber to the other are also part of the list of issues related to this technique.

Going towards more integrated designs, one can cite suspended systems (as already shown in 1.2 a)) where the access waveguide is fully suspended in air at the same level as the resonator and generally built out of the same material as the latter. It benefits from the highest refractive index contrast possible, but it makes the device fragile. Some commercial solutions exist with very short suspended parts and a good external encapsulation to protect from dust and other environmental threats.

The usual way to overcome those problems is the use of fully encapsulated configurations, where both microdisk and waveguides are surrounded by a low refractive index dielectric, commonly SiO_2 or some polymeric resin [33]. This also allows the design of 3D PICs [82], overcoming the limitation of placing resonators and guides in the same plane. It also has limitations: After the fabrication process the geometrical parameters of the circuit cannot be modified, so very precise calculations have to be made to find the optimal values. Also, it requires an extremely precise alignment in the lithography steps, which often results in fabrication flaws for a significant part of fabricated devices. To build these 3D PICs one usually relies on bonding before processing rather than bonding two processed PICs due to the much higher precision in the e-beam lithography processes [32]. In this section we will explore the impact of the geometrical parameters of fully integrated evanescent couplers on the simultaneous coupling and its efficiency, in telecom and datacom bands, which will provide new insights on the SHG efficiency in III-V microdisks.

2.1.1 Coupled Mode Theory

When two waveguides are placed very close to each other so that the propagating modes inside them overlap together, optical power is transferred from one waveguide to the other over some length (called the “beat” length). Coupled mode theory (CMT) is the common perturbative approach to describe the interaction between these copropagating confined modes. It is based on the assumption that the field for the complete structure can be described as the linear superposition of the eigenmodes of each individual waveguide.

Assuming waves propagating along z-axis, the total field can be written as:

$$E = A(z)E_1 + B(z)E_2 \tag{2.1}$$

$$H = A(z)H_1 + B(z)H_2 \tag{2.2}$$

Where $E_{1/2}$ are the mode profiles of each individual waveguide. The total field should satisfy Maxwell equations:

$$\nabla \times E = i\omega\mu_0 H \tag{2.3}$$

$$\nabla \times H = -i\omega\varepsilon_0 N^2 E \tag{2.4}$$

where N is the refractive index distribution. Using the vector relation:

$$\nabla \times (AE) = A\nabla \times E + \frac{dA}{dz} u_z \times E \tag{2.5}$$

where u_z is the unit vector along the propagation direction, we can express the two fields as:

$$\frac{dA}{dz} u_z \times E_1 + \frac{dB}{dz} u_z \times E_2 = 0 \tag{2.6}$$

$$\frac{dA}{dz} u_z \times H_1 + i\omega\varepsilon_0 (N^2 N_1^2) A E_1 + \frac{dB}{dz} u_z \times H_2 + i\omega\varepsilon_0 (N^2 N_2^2) B E_2 = 0 \tag{2.7}$$

Integrating over space and making orthogonality relations appear, [83] we can write:

$$\frac{dA}{dz} + c_{12}\frac{dB}{dz} e^{i(\beta_2-\beta_1)z} + i\chi_1 A + i\kappa_{12} B e^{i(\beta_2-\beta_1)z} = 0 \tag{2.8}$$

$$\frac{dB}{dz} + c_{21}\frac{dA}{dz} e^{i(\beta_1-\beta_2)z} + i\chi_2 B + i\kappa_{21} A e^{i(\beta_1-\beta_2)z} = 0 \tag{2.9}$$

Three terms in these equations contain all the physics of the coupling process: c_{pq} is called butt coupling coefficient. It corresponds to the coupling that one should obtain if mode p just ended when mode q starts. χ_p is the coupling coefficient of the mode p onto itself and κ_{pq} is the coupling coefficient between mode p and q. Practically, the only non-negligible term is the latter:

$$\kappa_{pq} = \frac{\omega\varepsilon_0 \int\int (N^2 - N_q^2)\tilde{E}_p^* \tilde{E}_q dxdy}{\int\int u_z(\tilde{E}_p^* \times \tilde{H}_p + \tilde{E}_p \times \tilde{H}_p^*)dxdy} \tag{2.10}$$

With this approximation, in a lossless system we would have $\kappa_{12} = \kappa_{21}^*$. In addition, in most of the codirectional couplers, this parameter is real so that $\kappa_{12} = \kappa_{21} = \kappa$. It has also been demonstrated that monomode vertical coupling between WGMs and the coupling waveguide, can be described as coupling between two parallel slab waveguides using CMT [84].

To summarize the effect of a coupler, a scattering matrix can be obtained integrating equations 2.8 along the interaction length. With $A_{0/1}$ and $B_{0/1}$ as the input/output field envelopes in waveguide 1 and 2 respectively, the scattering matrix is defined as:

$$\begin{pmatrix} A_1 \\ B_1 \end{pmatrix} = \begin{pmatrix} t & -ir \\ -ir^* & t^* \end{pmatrix} \begin{pmatrix} A_0 \\ B_0 \end{pmatrix} \tag{2.11}$$

where t and r are the complex transmission and coupling coefficients of the coupler respectively (figure 2.1). When considering a lossless coupling, r and t satisfy the relationship $|r|^2 + |t|^2 = 1$, this approximation will be considered throughout this work.

A coupled circular resonator can be easily modeled from the latter relation, as an evanescent coupler with a feedback relation on one way as depicted in figure 2.1.

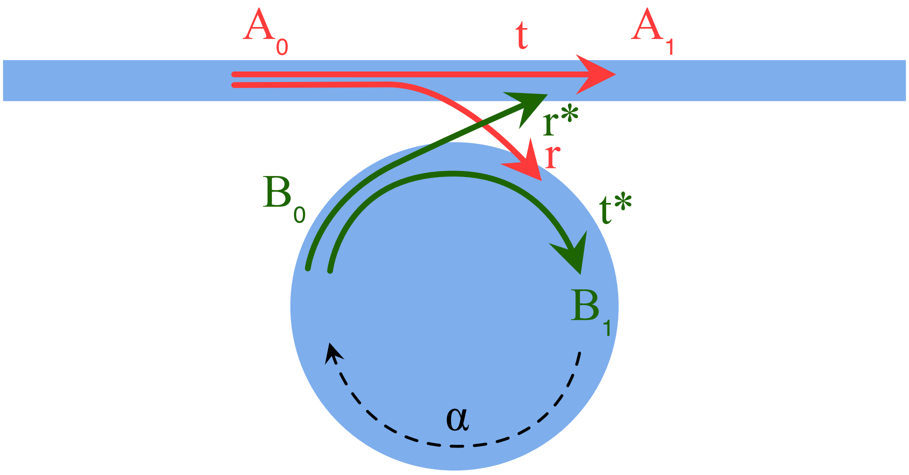

Figure 2.1: Scheme showing the notation used to describe the coupling through CMT. t is the transmission coefficient. r is the coupling coefficient between the waveguide and the resonator. α represents the internal losses each round-trip. A and B are the amplitudes of the fields in the waveguide and the microdisk respectively.

In the resonator, we model the intrinsic losses introduced in chapter 1 by the *inner circulation factor* α to model internal losses. Then, after one round trip, one can relate B_0 to B_1 writing explicitly the accumulated phase shift:

$$B_0 = B_1 \alpha e^{i\varphi} \tag{2.12}$$

φ being the phase difference in one round-trip.

If we consider a mismatched waveguide-resonator system, t and r can be written as:

$$t = [cos(\Gamma L) + i\frac{\Delta\beta}{2\Gamma}sin(\Gamma L)]e^{-i\frac{\Delta\beta L}{2}} \tag{2.13}$$

$$r = i\frac{\kappa}{2\Gamma}sin(\Gamma L)]e^{-i\frac{\Delta\beta L}{2}} \tag{2.14}$$

where $\Gamma = \sqrt{\kappa^2(\Delta\beta/2)^2}$ and L the coupling length.

These terms, t and α are directly related to the coupling and intrinsic quality factors respectively:

$$Q_{coupling} = \pi m\frac{\sqrt{t}}{1-t} \quad Q_{intrinsic} = \pi m\frac{\sqrt{\alpha}}{1-\alpha} \tag{2.15}$$

We can then define the *coupling regime*, described by the relationship between intrinsic and coupling quality factors. If $Q_{coupling}$ is higher than $Q_{intrinsic}$ we are in an *undercoupling regime.* On the contrary, if $Q_{coupling} < Q_{intrinsic}$, we say that we are in an *overcoupling regime.* The case where both are equal is called *critical coupling*, and is the point where the resonance peaks drop to zero, this point has usually been considered as the optimal point, not only for coupling but also for nonlinear processes. The validity of this assumption will be discussed in detail in the following.

In most textbooks, only the case of zero propagation constant mismatch is considered. By inserting equation 2.13 into equation 2.15, one can obtain the simultaneous influence of $\Delta\beta$ and κ on the $Q_{coupling}$ as plotted in figure 2.2. The coupling length is also calculated from the vertical overlap in the configurations studied in the next section (table 2.1).The ranges of κ and $\Delta\beta$ have been fitted to realistic values ($\kappa = 0.7$ correspond to the overlap with a waveguide in contact with the microdisk in vertical configuration at 2 µm of wavelength. While the minimal value of the $Q_{coupling}$

is obtained for $\Delta\beta = 0$ for a quite large value of κ, one can see a ring of large values of Q_{factor} around this point for finite values of $\Delta\beta$. For resonators presenting $Q_{intrinsic}$ above 10^4, this peripheral region is particularly interesting to achieve critical or undercoupling.

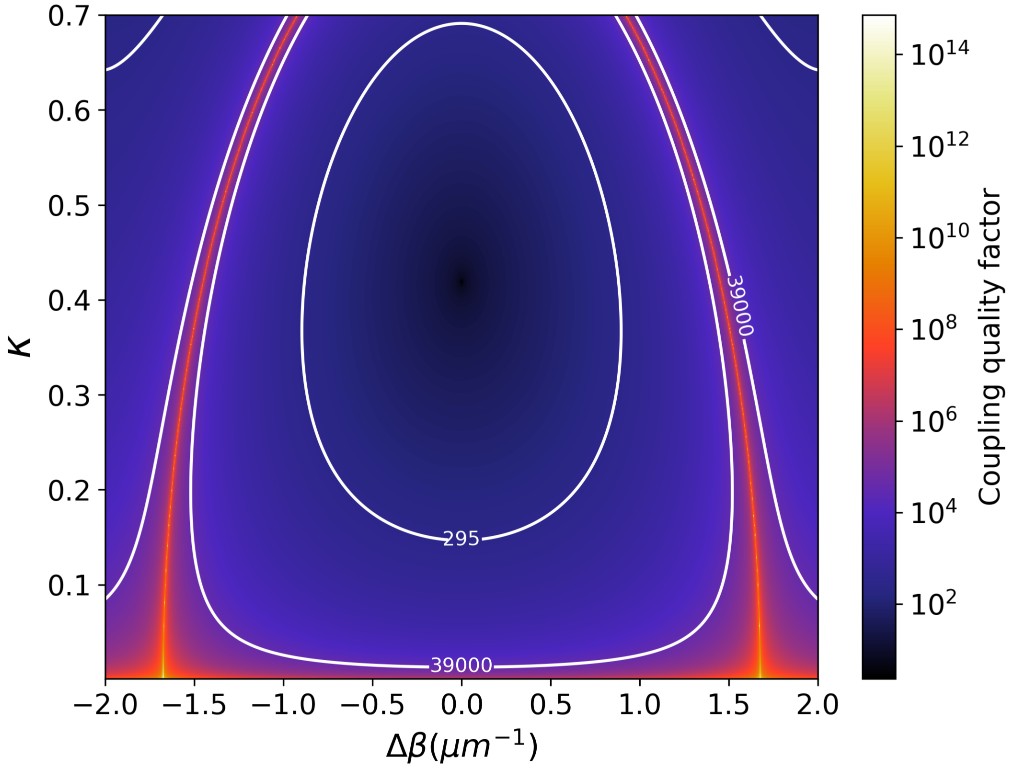

Figure 2.2: Surface map of coupling quality factor vs propagation constant mismatch and mode overlap for a coupling length of 3.75 µm. Contour lines correspond to the intrinsic Q factors of the selected WGMs for SHG, more details are given in section 2.1.3

2.1.2 How to Efficiently Couple a Wavelength Converter?

When designing integrated coupling systems for nonlinear elements in PICs, we need solutions to efficiently inject and extract photons of different wavelengths in different elements. For resonators, the standard procedure is to match the propagation constant of the modes in the waveguide with the resonant modes in the cavity. Then the phase term disappears in equations 2.8, which can be very convenient in pulley coupling schemes, where the waveguide bends around the resonator, to avoid destructive interferences. In the configuration of strict $\bar{4}$-QPM that we chose to investigate, disks are however very small, of a few microns in radius. We will thus focus on point-like coupling schemes only, where the coupling length is negligible compared to the perimeter of the resonator. We will first discuss configurations where propagation constant matching can be obtained for at least one wavelength of the SHG while in the next sections we will open the discussion to fully mismatched configurations.

Since for SHG a very precise design of the cavity is required due to the need of a double resonant condition and $\bar{4}$-QPM, the engineering of the propagation constants at both fundamental and SH wavelengths is left to the sole waveguide design, with the constraints of the SHG selection rules on polarization. Both dispersions of TE and TM modes of the waveguides should thus be under scrutiny.

We thus study a GaP microdisk of 3.4 µm of radius and 180 nm of thickness for SHG with strict $\bar{4}$-QPM between a fundamental TE mode at 2 µm and a SH TM mode at 1 µm with WGMs of azimuthal numbers of 18 and 38 respectively as predicted by Pierre Guillemé using semianalytical theory [52]. We will consider three different coupling schemes to this resonator as depicted in figure 2.3: the all-pass configuration, the add-drop configuration and the coupling to a slit waveguide. We

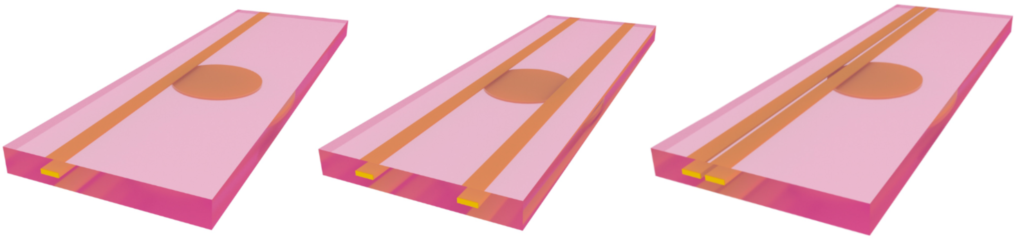

Figure 2.3: 3D representation of the three configurations studied: all-pass (left), add-drop (center) and slit (right).

consider in this section GaP rectangular waveguides to enable $\Delta\beta = 0$ conditions. The geometrical parameters can be found in table 2.1 and will be justified in section 2.1.3. 3D and plane cut sketches for the three configurations are presented in figures 2.3 and 2.4 respectively. This system is considered fully encapsulated in BCB[1]. Part of this work can be found in [85].

	All-pass	Add-drop (F/SH)	Slit (s=50nm)
Width	820nm	1000/820nm	700nm
Height	167nm	167nm	165nm
V_{dist}	400nm	400nm	400nm
H_{pos}	0nm	0/200nm	350nm

Table 2.1: Geometrical parameters of the different configurations for the β matching condition. For the all-pass configuration the waveguide has been designed for the fundamental wavelength.

The first approach studied for coupling between a waveguide and a resonator is the *all-pass* configuration. It consists of a single waveguide performing both tasks

---

[1] Refractive index of BCB is set to 1.54 according to manufacturer specifications.

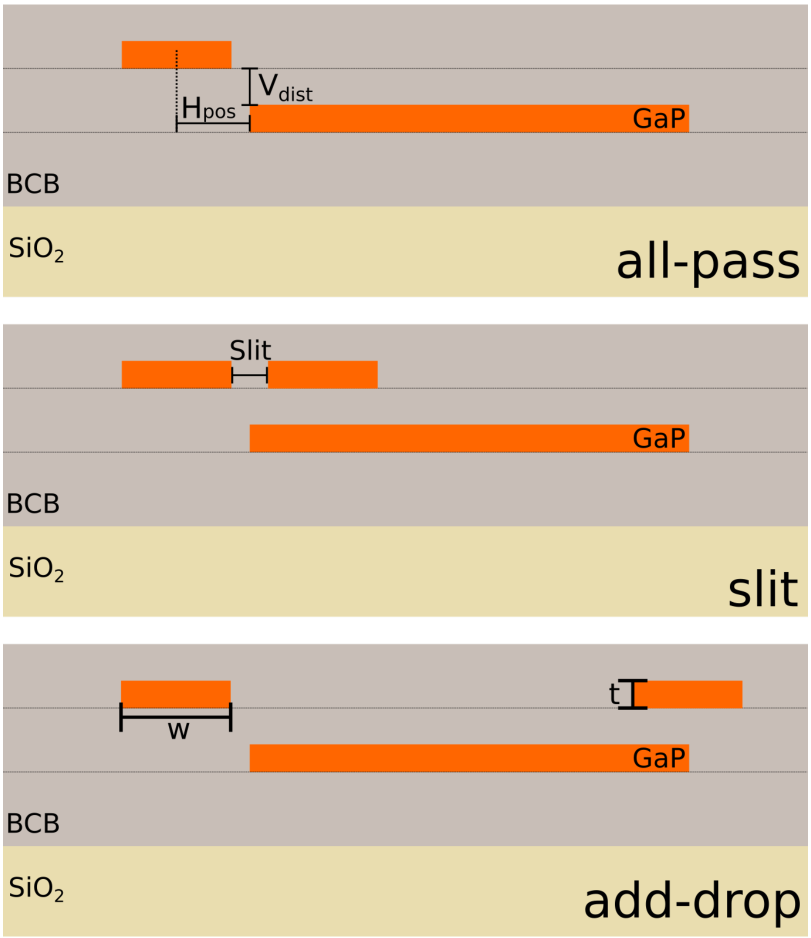

Figure 2.4: Vertical cut plane and geometrical variables studied of the three configurations analysed: all-pass (top), slit (center) and add-drop (bottom).

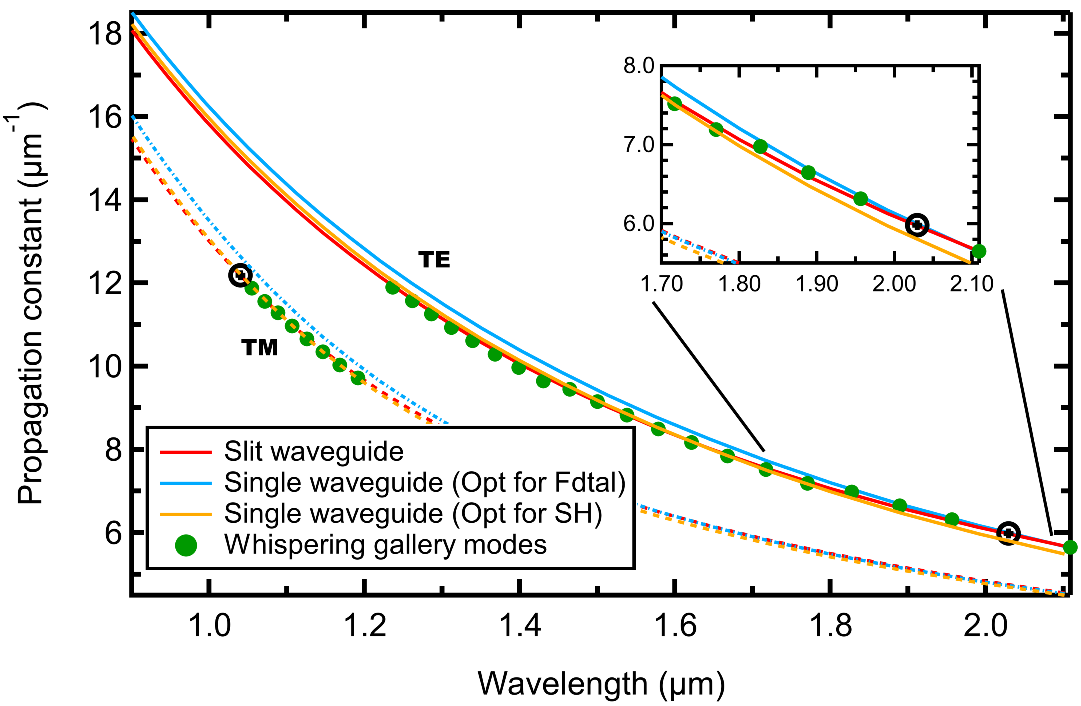

Figure 2.5: Dispersion curves of WGM and access waveguides for the studied system. Add drop configuration is then the combination of one single waveguide optimized for fundamental and other single waveguide optimized for SH. The effective propagation constant of WGMs is calculated following the method proposed in [86].

of injecting the fundamental and extracting the SH generated. The main problem is that WGMs and the modes supported in a rectangular waveguide have different group index so that their dispersion curves will be different and the $\Delta\beta = 0$ condition is only possible at one wavelength (as shown in fig 2.5). For a SHG process from 2 µm to 1 µm, the zero propagation constant mismatch can be obtained either for the TE fundamental mode only (blue curve) or the TM SH mode only (orange curve). The propagation constant of the targeted WGMs are $12.2\,\mu\text{m}^{-1}$ for the SH and $6.0\,\mu\text{m}^{-1}$ for the fundamental.

To solve this problem, the typical solution is the use of the so called *add-drop* configuration, where the coupling system is composed of two independent waveguides, one optimized for the injection of the fundamental and the other one optimized for the extraction of the second harmonic. While this configuration solves the problem of the difference in the dispersion, it adds the perturbation of a second waveguide to the microresonator, increasing the losses and lowering the Q_{factor} of the resonances.

Aside of these two well-known approaches, in this thesis we will also explore a third one, a *slit* waveguide. Here, the use of a small gap between two parallel waveguides results in the occurrence of *supermodes* which are the linear combinations of modes in each waveguide. The particularity of this system is that, if the gap is small enough, TE-polarized symmetric supermodes are mainly trapped inside the slit while TM-polarized supermodes propagate through the waveguides (figure 2.6). Then, modifications of the gap between guides mainly affect the propagation constant of the TE supermodes allowing a quasi-independent tuning of β for the input TE and output TM modes as shown with the red curves of figure 2.5, where $\Delta\beta = 0$ is obtained for both wavelengths.

For all of these three configurations we can consider fabrication tolerances in the

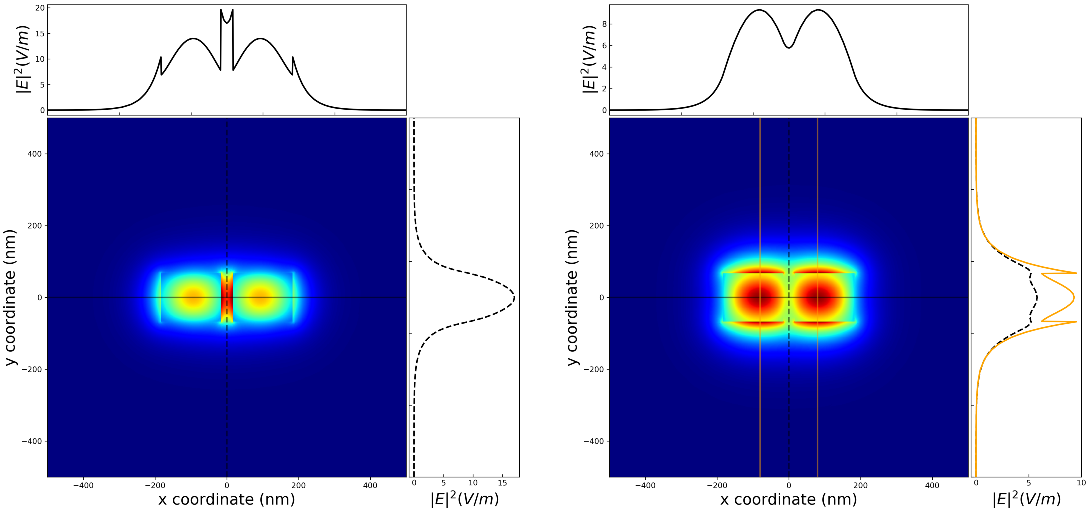

(a) (b)

Figure 2.6: Mode profiles of the symmetric TE (left) and TM (right) supermodes generated in the slit waveguide.

order of 5% taking into account film thickness variations due to local strain relaxation in the epitaxial layers, as well as lithography or etching-induced deviations onto the width of the waveguides or the slit opening. The variations introduced in the propagation constants by such flaws are not more than 1% for the three coupling cases making the three of them viable technologically. In next section we study the three schemes in 3D FDTD simulations to analyse the different coupling conditions achievable in each case.

2.1.3 3D FDTD Simulations of Vertical Coupling Schemes

Standard methods for computing the propagation in dielectric media are Finite Element Method (FEM) and Finite-Difference Time Domain (FDTD) simulations. Here we study the mode dispersion of rectangular waveguides through FEM methods and the propagation of light in the vertically coupled microresonator configurations described above, with three dimensional FDTD calculations.

Due to the tridimensional nature of the coupling configurations under scrutiny, calculating κ is not straightforward because of the difference in the symmetries between the circular resonator and the linear access waveguide. To overcome this, we rather calculate the transmission spectra of the coupled resonator so we can extract the loaded quality factor of the device. Then, calculating the intrinsic quality factor of the resonant modes by FEM and the propagation constant mismatch, we can retrieve κ for a given coupling configuration at both fundamental and SH frequencies.

To obtain the resonant frequencies and the intrinsic quality factor of the WGM we perform axisymmetric FEM calculations with the cross-section of the microdisk. This also allows obtaining the effective propagation constant of the WGM given by:

$$\beta_{WGM} = \frac{m}{r_{WGM}} \tag{2.16}$$

where m is the azimuthal number and r_{WGM} the radius of the mode as described in [86].

Due to the strict $\bar{4}$-QPM configuration under scrutiny, which require very thin disks, a large difference in the behaviours of the fundamental and SH modes is observed because of their polarizations: for the SH TM mode intrinsic Q factor values in the range of 10^6 are expected. For the sake of computational time, we added artificial absorption losses in the material to reduce it. On the other hand, the intrinsic quality factor for the fundamental TE mode is only 295. This low value is due to the small effective refractive index of the slab waveguide at 2 µm of wavelength, which strongly contributes to the reduction of the intrinsic Q factor as already presented in figure 1.6. The drawback of small $Q_{factors}$ is balanced by the large field overlap due to the strict $\bar{4}$-QPM condition.

The transmission FDTD simulations obtained for the three configurations introduced in section 2.1.2 are presented in figure 2.7. Due to the different computation methods used between Pierre Guillemé's work and the present work, energy conservation is not strictly reproduced for this set of azimuthal wavelength around 1 and 2 µm in the FDTD simulations. A refinement of the microdisk dimensions would be necessary to retrieve it. This energy mismatch does not hinder the discussion on coupling optimization. Using the intrinsic Q_{factor} calculated for the investigated resonator case and the calculated linewidths of the resonances we can thus extract the coupling Q_{factor} of the different configurations (provided in the figure), their coupling regime and an estimation of κ.

The optimization of the evanescent coupler parameters from the transmission simulations, as summarized in table 2.1 is not a straightforward task. The width and height of a waveguide are first adjusted to obtain β matching for one wavelength and reduce the β mismatch on the other one. In a second time the lateral position and vertical distance of the coupler are adjusted to find the balance between undercoupling on the fundamental wavelength and overcoupling on the SH wavelength, due to the different behaviour in their confinement. This is performed by analyzing both depth and width of the fundamental and SH resonances for each set of parameters. Note that we restricted our study to: i) identical thickness for both guides in the add-drop and slit configurations, ii) a vertical position of the waveguides above 100 nm, accessible experimentally with our facilities as it will be discussed in chapter 4, iii) similar waveguide alignments and vertical distances for all three configurations for the sake of validity of the comparison between the coupling schemes.

In fig 2.7 we can see that for the fundamental mode injection, we obtain a similar

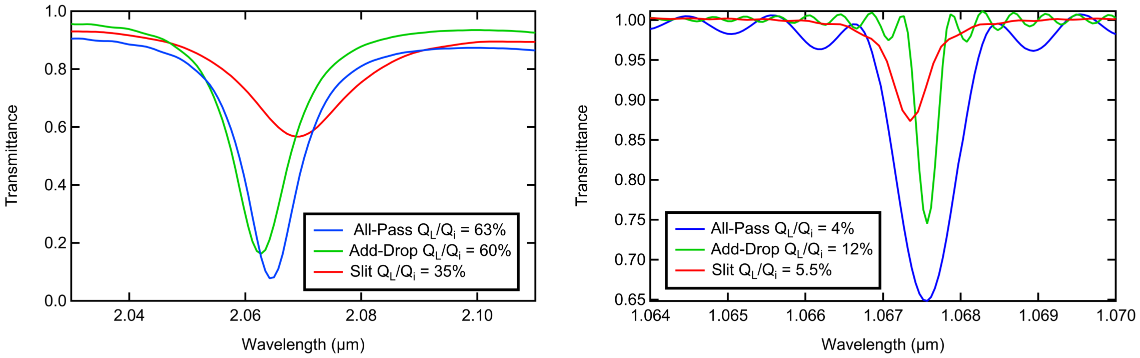

Figure 2.7: Transmission spectra in all configurations for fundamental(left) and second harmonic (right) wavelengths. Legend shows the ratio between loaded and intrinsic quality factors, which is 50% at critical coupling. Geometrical parameters can be found in table 2.1.

undercoupling regime for both the all-pass and add-drop configurations, resulting in a coupling Q_{factor} around 500. The transmission depth is slightly better for the all-pass configuration due to the absence of drop port. In fact, despite the optimization of the drop port for the SH, too much power is lost for the fundamental wavelength if the SH drop port waveguide is too close to the disk. To solve that we shift the horizontal position of the SH drop port by 200 nm (H_{pos}) resulting in a strong reduction of the resonance depth observed in figure 2.7 (green curve, right panel). For the slit waveguide, overcoupling can be reached with a $Q_{coupling} = 160$. These values of $Q_{coupling}$ allow us to retrieve κ values of 0.12, 0.13 and 0.21 for the all-pass, add-drop and slit cases respectively.

For the second harmonic case, due to the high intrinsic quality factor, all of the configurations are in overcoupling regime, as indicated by the small Q_{loaded} and transmission depth below 0.5. In the add-drop case, since the SH drop-port has been moved aside from the microdisk to prevent unintentional coupling of the fundamental mode in this port, the Q_{loaded} of the SH mode is enhanced in comparison with the all-pass case due to a smaller value of κ. The values of $Q_{coupling}$ on the SH modes are 1625 and 5300 for the all-pass and add-drop configuration respectively. With those $Q_{coupling}$, the values of κ are then 0.1 for the all-pass, 0.05 for the add-drop and 0.08 for the slit. For the slit waveguide configuration, a SH Q_{loaded} comparable to the one of the all-pass is observed but at the expense of a strong reduction on the transmission depth. This necessarily comes from an increase of the losses in the microdisk, due to insertion losses and scattering towards other supermodes of the slit waveguide. If this should not affect too much the efficiency of the doubly resonant nonlinear process, it will reduce the extraction of the SH mode by a factor of three compared to the all-pass case.

This means that in these configurations where β matching is obtained for at least one wavelength, the add-drop will be better adapted to continuous signal conversion thanks to its deep and sharp resonances at both frequencies. On the contrary, the all-pass configuration is particularly suited for wavelength conversion in the pulsed regime due to its broader resonances. For the slit waveguide configuration, a Q_{loaded} comparable to the one of the all-pass is observed but at the expense of a strong reduction on the transmission depth, this necessarily comes from an increase of the losses in the microdisk, due to insertion losses and scattering towards other supermodes of the slit waveguide. If this should not affect too much the efficiency of the doubly resonant nonlinear process, it will be detrimental for the extraction of the SH mode by a factor of three compared to the all-pass case. However. the increase of the size in resonance is also beneficial to ease the tuning of the resonances, increasing the overlap.

2.2 Conversion Efficiency

If the two parameters $\Delta\beta$ and κ is sufficient to fully characterize an evanescent coupler, it is not enough to address its impact on the conversion efficiency of a nonlinear process like SHG. To do so, in the following we first derive the conversion efficiency in strict $\bar{4}$-QPM and analyse the role of the different coupling parameters. In a second time, we also introduce the temporal nonlinear equations to point out the conditions required to be in a non-depletion and depletion regime of the pump.

2.2.1 Derivation of the Conversion Efficiency for Strict $\bar{4}$-QPM in the Undepleted Regime

To calculate the conversion efficiency in the case of strict $\bar{4}$-QPM we can integrate equation 1.20 along the microdisk, adding the attenuation term to account for losses at each round-trip. We obtain:

$$\frac{B_{0,SH}}{\alpha_{SH}e^{i\varphi_{SH}}} - B_{1,SH} = |B_{1,f}|^2 K \tag{2.17}$$

We can express the phase shift as a function of the azimuthal number $\varphi = -2m\pi$. It's important to remark that only resonant modes will have integer values of m.

Since there is no SH signal injected in the microresonator, $A_{0,SH} = 0$ and then we can use equation 2.11 to write $B_{1,SH} = t_{SH}B_{0,SH}$. Introducing this in 2.17 we have:

$$\frac{B_{0,SH}}{\alpha_{SH}e^{i\varphi_{SH}}} - t_{SH}B_{0,SH} = |B_{1,f}|^2 K \tag{2.18}$$

Now, since we are considering a non-depleted pump ($B_{1,f} = B_{0,f}$), isolating $B_{0,SH}$

and taking the squared modulus we can write:

$$|B_{0,SH}|^2 = |B_{0,f}|^4 \frac{|K|^2 \alpha_{SH}^2}{1 + \alpha_{SH}^2 t_{SH}^2 - 2\alpha_{SH} t_{SH} cos(\varphi_{SH})} \tag{2.19}$$

Now imposing the equation from annexe A, A.7, we obtain:

$$\begin{aligned} |B_{0,SH}|^2 = |A_{0,f}|^4 & \frac{|K|^2 \alpha_{SH}^2}{1 + \alpha_{SH}^2 t_{SH}^2 - 2\alpha_{SH} t_{SH} cos(\varphi_{SH})} \\ & \times (\frac{\alpha_f^2 (1 - t_f^2)}{1 + \alpha_f^2 t_f^2 - 2\alpha_f t_f cos(\varphi_f)})^2 \end{aligned} \tag{2.20}$$

from equation 2.11 with $A_{0,SH} = 0$ and $r^2 = 1 - t^2$ we have the following relationship:

$$|A_{1,SH}|^2 = (1 - t^2)|B_{0,SH}|^2 \tag{2.21}$$

we can define the input power as $P_{in} = |A_{0,f}|^2$ and write the conversion efficiency as:

$$\begin{aligned} \eta = \frac{P_{out}}{P_{in}} = \frac{|A_{1,SH}|^2}{|A_{0,f}|^2} = P_{in}|K|^2 & \frac{\alpha_{SH}^2 (1 - t_{SH}^2)}{1 + \alpha_{SH}^2 t_{SH}^2 - 2\alpha_{SH} t_{SH} cos(\varphi_{SH})} \\ & \times (\frac{\alpha_f^2 (1 - t_f^2)}{1 + \alpha_f^2 t_f^2 - 2\alpha_f t_f cos(\varphi_f)})^2 \end{aligned} \tag{2.22}$$

since for resonant modes φ is multiple of 2π, equation 2.22 can be simplified as:

$$\eta = P_{in}|K|^2 \frac{\alpha_{SH}^2 (1 - t_{SH}^2)}{(1 - \alpha_{SH} t_{SH})^2} \times (\frac{\alpha_f^2 (1 - t_f^2)}{(1 - \alpha_f t_f)^2})^2 \tag{2.23}$$

2.2.2 Impact of Coupling Parameters on the Conversion Efficiency in the Undepleted Regime

The transmittance coefficients, t_F and t_{SH}, in 2.23 can be expressed as a function of propagation constant mismatch and κ using equation 2.13. This means that we can explore the influence of these two parameters on the conversion efficiency. Also, since these terms will also define the quality factors, we can address the impact of coupling Q factors on the efficiency. This insight is interesting because in the literature, as mentioned before, critical coupling is most of the time considered as the optimal point for nonlinear wavelength conversion.

Let us first fix the coupling length and plot the efficiency as a function of κ_f and κ_{SH} for different values of $\Delta\beta$ (figure 2.8). Several conclusions can be extracted from this plot. First, we observe that the maximum value of efficiency is not, in first approximation, determined by $\Delta\beta$. This means that for any propagation constant mismatch, there is a couple of overlap parameters (κ_f, κ_{SH}) that gives the same optimal efficiency of the system. Second, critical coupling for both fundamental mode and SH mode (crossing points of dashed lines in figure 2.8) is definitely not the point of highest efficiency even if it is close to it.

And third and the most important from the technological point of view, there are some values of propagation constant mismatch that offer large windows of very good efficiency. This is a real asset since the practical values of $\kappa_{f/SH}$ can strongly depend on mask alignment or layer thickness tolerances. For example in the $\Delta\beta = 1\ \mu m$ situation, a very slight variation in the value of κ can pass the system from a critical coupling situation, with high conversion efficiency, to a very low efficiency case. On the contrary, the $\Delta\beta = 2\mu m^{-1}$ case offers a large set of values of κ_f of very good efficiency, with values of κ similar to those obtained in the previous section.

In order to get more insight to this tolerance property of the nonlinear process, we plotted on figure 2.9 for each combination of values of propagation constant mismatch ($\Delta\beta_f$, $\Delta\beta_{SH}$), the percentage of the $\kappa_{f/SH}$ surface map showing an efficiency larger than 50% of the maximum efficiency in figure 2.8. The integration range for κ goes from 0 to 0.7 for the fundamental and from 0 to 0.4 in the SH case, the upper bounds are the maximum realistic ones obtained in our calculations and it would correspond to a zero vertical distance and a perfect mode alignment. In the precise configuration of strict $\bar{4}$-QPM considered here and a fixed coupling length of 3.75 µm, we can thus predict that $\Delta\beta_{SH} = 0.9\mu m^{-1}$ and $\Delta\beta_f = 1.4\mu m^{-1}$ are the most reliable conditions to optimize the conversion efficiency, whatever the deviations in the positioning of the waveguides are. Note that this convenience of non-zero values of propagation constant mismatch, also justifies the use of different materials for the microdisk and the waveguides, which is mainly avoided for microresonator evanescent coupling [71].

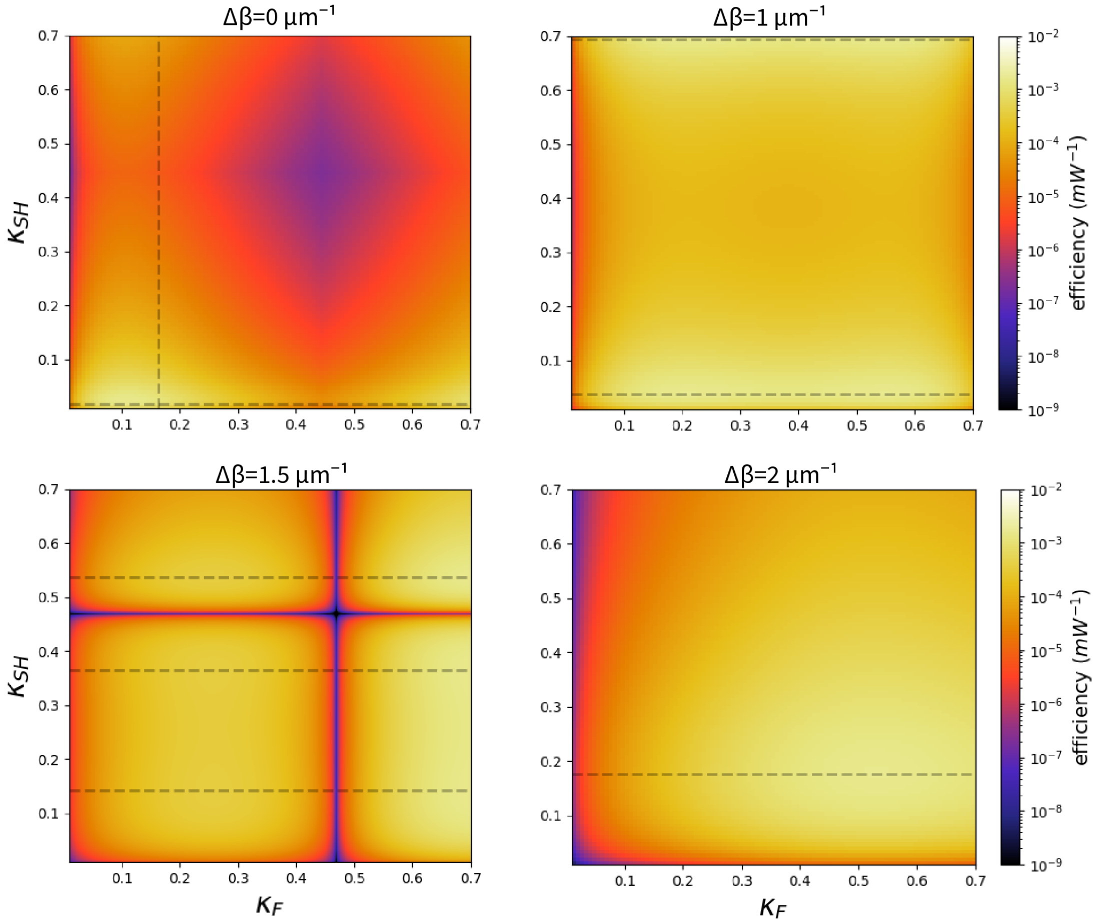

Figure 2.8: Surface maps of conversion efficiency versus κ of fundamental and SH modes. Dashed lines show the values of κ that would give critical coupling with a microdisk of the intrinsic quality factors obtained in section 2.1.3. Nonlinear coupling constant calculated from data in [52]. Panels correspond to the $\Delta\beta = 0\mu m^{-1}$ case (top left), $\Delta\beta = 1\mu m^{-1}$ case (top right), $\Delta\beta = 1.5\mu m^{-1}$ case (bottom left) and $\Delta\beta = 2\mu m^{-1}$ case (bottom right).

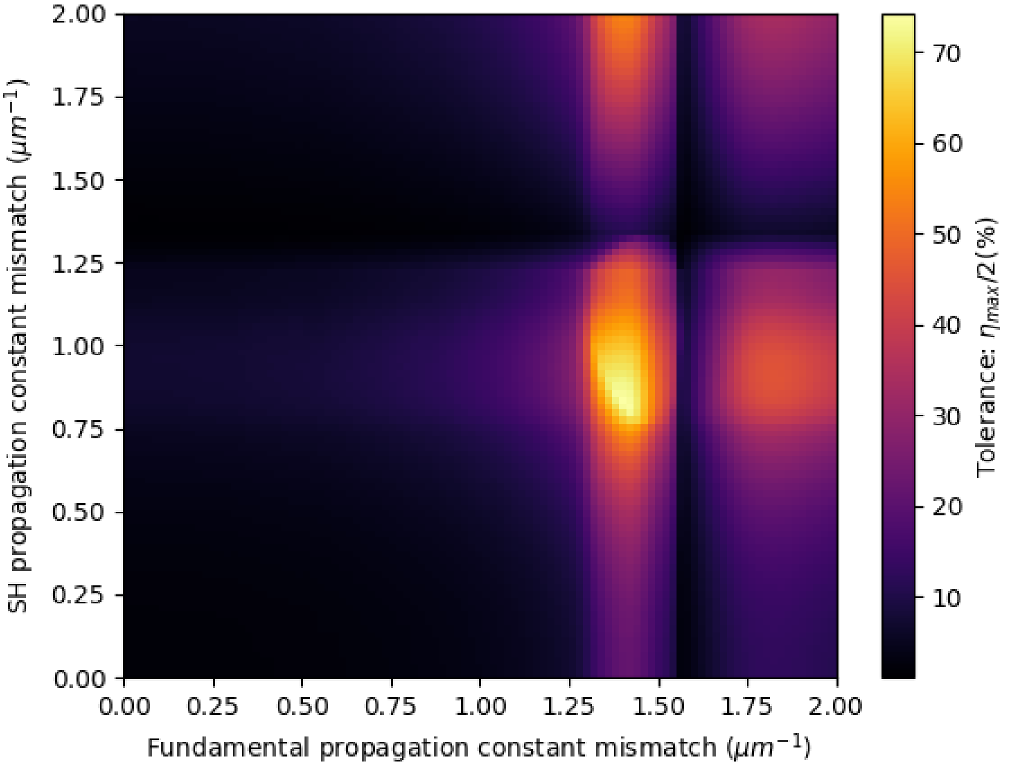

Figure 2.9: Surface map of the percentage of combinations of κ values that give efficiencies of at least 50% of maximum efficiency.

Conclusion

In this chapter we have studied three technologically viable configurations for vertical evanescent coupling. Using CMT we have demonstrated that a detailed analysis of the coupling is needed in order to correctly design the access waveguides and in the positioning to optimize SHG efficiency. We also used 3D FDTD simulations to characterize these systems. We have also shown a much less common approach for evanescent coupling, the slit waveguide, making use of supermodes to independently tune propagation constants. We have also demonstrated that critical coupling is not the point of highest efficiency and that a carefully interplay between overlap, coupling length and propagation constant mismatch should be investigated in order to design efficient SHG integrated microresonators. We also proposed that some values of propagation constant mismatch offer very large windows of very high efficiency, relaxing the fabrication tolerance.

In the end, we have come to the conclusion that an integrated coupling scheme based on all-pass configuration should offer good performance and higher tolerance to process flows for wavelength conversion, especially if we can engineer a β mismatch of $1.4\,\mu\text{m}^{-1}$ between the access waveguide and the microdisk resonator. This should be possible with a waveguide platform based on silicon nitride.

Chapter 3

Study of the Second-Order Quasi-phase-matching in Whispering Gallery Resonators

3.1 Actual Azimuthal Number Selection Rules

As discussed in section 1.4.3, conserving momentum in nonlinear processes in whispering gallery mode resonators is not trivial. In this kind of axisymmetric resonators, the phase-matching condition appears as a selection rule on the azimuthal number of input WGMs and nonlinear products. Depending on the crystal symmetry and the material, different additional quanta can appear in this selection rule.

This was attributed to a natural poling of the crystal in axisymmetrical systems [87]. So far, the explanation given to these additional quanta was the derivation of the Fourier components of the azimuthal dependence of the second-order nonlinear coefficient, providing momentum to photons [67].

This has been studied experimentally in a large set of materials. For example lithium niobate, $LiNbO_3$ (LN), can be used to do planar WGM resonators in two crystallographic orientations. In the so-called z-cut configuration, the extraordinary axis of the crystal is parallel to the resonator revolution symmetry axis and the observed selection rule is $\sum m_{prod} = \sum m_{in}$ which requires artificial periodic poling for efficient frequency conversion [88, 89].

On the contrary, in x-cut LN, where the sample plane is the $(2\bar{1}\bar{1}0)$ surface, the extraordinary axis is rotated by 90° compared to the z-cut configuration and lies in the microdisk plane. In this configuration, SHG has been observed between a fundamental mode of $m_F = 111$ and a SH mode of $m_{SH} = 221$, so that only a single momentum quantum is lost [67]. In contrast, the QPM selection rule of wurtzite in GaN microdisk is $\Delta m = 0$ [70].

In zinc-blende crystals, as introduced in chapter 1, the $\bar{4}$-QPM condition [47], named after the $\bar{4}3m$ point group symmetry, requires the introduction of two additional quanta:

$$\Delta m = \sum m_{prod} - \sum m_{in} = \pm 2 \tag{3.1}$$

In the calculation of the nonlinear conversion efficiency, each phase-matching condition is associated with a weight, which is specific to the signed value of the additional quantum, as introduced in equation 1.20 [47]. This Fourier approach gives neither a physical meaning to the expressions of these different weights, nor a rule on the appearance of these additional quanta. In addition, this analysis requires some approximation on the effective radius of the modes. This points out the need of a new formalism for the derivation of second-order nonlinear processes in resonators with rotational symmetry, which is the topic of the present chapter.

3.2 Novel Description of the Polarization Properties in WGM Resonators

Recently, it has been pointed out that under high confinement conditions, the longitudinal electric field component of light becomes non-negligible [90]. This makes possible for photons to carry transverse spin angular momentum (TSAM), a forbidden property in plane wave optics. In this framework one can study the propagation of a photon with a spin perpendicular to the propagation plane. WGM resonators suit particularly well to this description since the geometry of the system and the TSAM polarization basis share the same revolution symmetry.

We take the same labelling as used in section 1.3, making the approximation that TM modes will only feature nonzero electric field component along the symmetry axis of the resonator, so that only the TE modes, which electric field lies in the resonator plane will show a TSAM character. Going beyond this approximation and studying the full-vectorial model of nonlinear processes would even open more possibilities to the present theory as suggested by Ciret *et al.* [90].

Most of the works in the literature of WGMs, from the basic confinement properties to the derivation of NL properties, use the rotating frame $(|r\rangle, |\varphi\rangle, |z\rangle)$ instead of the cartesian one $(|x\rangle, |y\rangle, |z\rangle)$, to fit the symmetry of the structure. But it still has the limitation of the parameterized direction of the basis unit vectors(figure 3.1). On the contrary, using a fixed circular polarization (CP) frame of the WMGs, one can unveil their TSAM character. To mathematically describe this new frame, we define

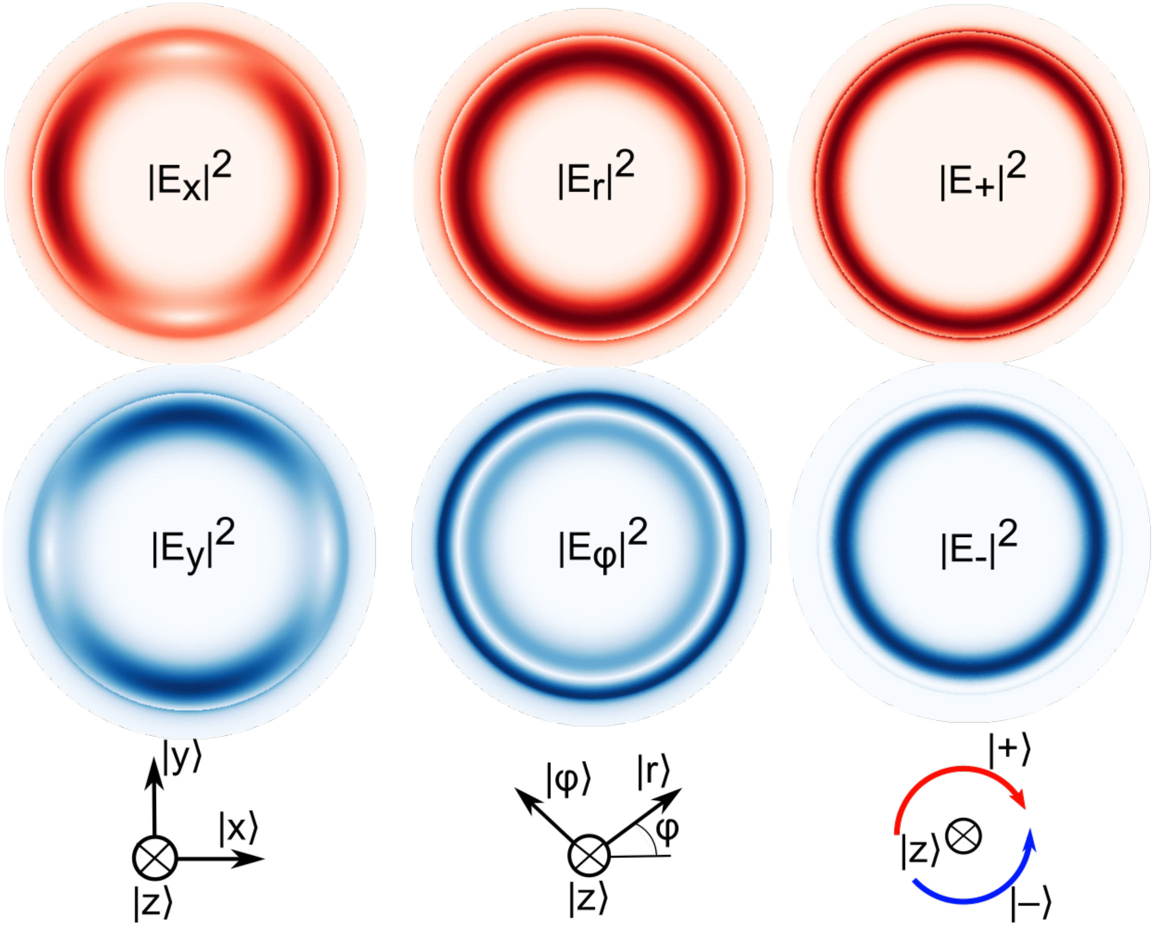

Figure 3.1: Squared magnitudes of the electric field planar components of a TE WGM using a Cartesian fixed basis (left), a rotating polar basis (middle), and the circular polarization basis along the resonator axis (left). The results are obtained from FEM simulations with a WGM at 1.9 µm with azimuthal order m = 18, planar and radial orders of 1, a refractive index of 3.04, radius of 3.4 µm, and 180 nm of thickness

the unit vectors of spin up ($|+\rangle$) and down ($|-\rangle$) polarized photons (figure 3.1):

$$|+\rangle = \frac{1}{\sqrt{2}}(|x\rangle + i|y\rangle) \tag{3.2}$$

$$|-\rangle = \frac{1}{\sqrt{2}}(|x\rangle - i|y\rangle) \tag{3.3}$$

The $|z\rangle$ polarization state remains unchanged and can be seen as describing photons with spin 0. From equations 1.7, we can describe the electric field components of TE modes in the rotating frame:

$$E_r = \frac{m}{r} C_m J_m(\beta_1 r) e^{im\varphi} = S_m(r) e^{im\varphi} \tag{3.4}$$

$$E_\varphi = \frac{i\beta_1}{2} C_m [J_{m-1}(\beta_1 r) - J_{m+1}(\beta_1 r)] e^{im\varphi} = iT_m(r) e^{im\varphi} \tag{3.5}$$

Where m is the WGM azimuthal order, C_m a constant, $J_i(x)$ the Bessel function of first kind and β_1 the effective propagation constant of the WGM. The functions $S_m(r)$ and $T_m(r)$ are real-valued and are introduced for the sake of clarity.

Now we can apply the transfer matrix $\mathcal{R}_z(\varphi)$ and the projections in the CP basis from equation 3.2 and write the mode profiles of the spin-up and spin-down photon components of the WGMs:

$$E_+ = \frac{1}{\sqrt{2}}(S_m(r) + T_m(r)) e^{i(m-1)\varphi} \tag{3.6}$$

$$E_- = \frac{1}{\sqrt{2}}(S_m(r) - T_m(r)) e^{i(m+1)\varphi} \tag{3.7}$$

With this change of basis, we observe the occurrence of opposite additional quanta on the azimuthal dependence of both CP components. This comes from the rotation operator involved in the rotating frame description, which can also be written using the spin operator s of the photon:

$$\mathcal{R}_z(\varphi) = e^{-i\varphi s} \tag{3.8}$$

This phenomenon is the consequence of the Berry phase experienced by each CP component during a round-trip. This was demonstrated by Chiao *et al.*, in the 80s [91, 92]. During a round-trip, the photon does a loop in the parameter space (k_x, k_y, k_z). The $k = 0$ point represents a topological monopole for photons so that they acquire a topological phase proportional to their spin number and to the solid angle completed in the closed circuit with respect to the monopole. Experimentally, the Berry phase was investigated into an optical fiber helically wrapped around a cylinder as sketched in figure 3.2. In this case, the Berry phase takes the form of:

$$\Omega = 2\pi N(1 - \cos(\theta)) \tag{3.9}$$

Where N is the winding number of the helix and θ the angle between the waveguide axis and the cylinder axis. Our case corresponds to a coiling without translation along the cylinder axis so that, $\theta = \pi/2$. For each round-trip the Berry Phase acquired is 2π, satisfying intrinsically the periodic boundary conditions in our resonant system. If we plot the phase of both CP components of a TE WGM (figure 3.2), we can see the different number of phase jumps experienced by each component.

In the next section we take into account this topological phase into the derivation of nonlinear conversion process by changing the basis of the susceptibility tensor. This new formalism allows the generalization of QPM in circular resonators.

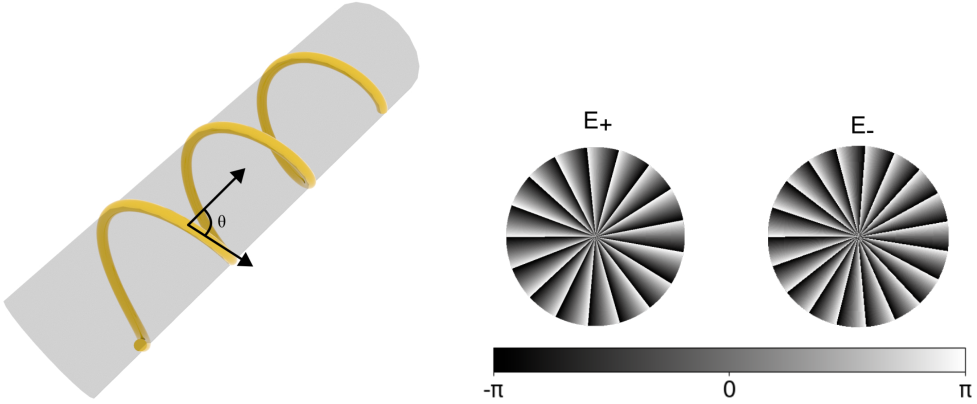

Figure 3.2: (a) Schematic representation of the Berry Phase experimental set up. (b) Phase distribution of the E_+ and E_- components of the TE mode, where opposite Berry phases shows up in the difference of 2π phase jumps (17 and 19 phase jumps, respectively).

3.3 Derivation of the Expressions for the General Case

To unveil the effect of the Berry phase experienced by the CP components on second-order nonlinear processes, one needs to project the susceptibility tensors along the complete CP basis ($|+\rangle, |-\rangle, |z\rangle$). We define the transfer matrix $\mathbf{Q}$ from Cartesian to CP basis so the second-order nonlinear polarization reads as:

$$P_{NL,CP} = \mathbf{Q}\chi^{(2)}_{x,y,x} \cdot (\mathbf{Q}^{-1}E_{CP}) \otimes (\mathbf{Q}^{-1}E_{CP}) \tag{3.10}$$

Where E_{CP} is the total input field and $\otimes$ the Kronecker product. Consequently, the second-order susceptibility tensor is defined as:

$$\chi^{(2)}_{CP} = \mathbf{Q} \cdot \chi^{(2)}_{x,y,z} \cdot (\mathbf{Q}^{-1} \otimes I_3)(I_3 \otimes \mathbf{Q}^{-1}) \tag{3.11}$$

I_3 being the identity matrix of dimension 3. The well-known nonlinear susceptibility tensor, in cartesian basis, usually reads as:

$$\chi^{(2)}_{xyz} = \begin{bmatrix} d_{11} & d_{16} & d_{15} & d_{16} & d_{12} & d_{14} & d_{15} & d_{14} & d_{13} \\ d_{16} & d_{12} & d_{14} & d_{12} & d_{22} & d_{24} & d_{14} & d_{24} & d_{23} \\ d_{15} & d_{14} & d_{13} & d_{14} & d_{24} & d_{23} & d_{13} & d_{23} & d_{33} \end{bmatrix} \tag{3.12}$$

Applying equation 3.11, one obtains the whole tensor representation (presented in annexe B). With the Kleinman symmetry present in the Cartesian basis, conserved during this basis change, we can reduce and simplify the expression of the tensor so that it read as:

$$\chi^{(2)}_{CP} = \begin{bmatrix} a & f & c^* & b - id_{14} & b + d_{24} & a^* \\ f^* & a^* & c & b + d_{24} & b + id_{14} & a \\ b + id_{14} & b - id_{14} & d_{33} & c^* & c & b + d_{24} \end{bmatrix} \tag{3.13}$$

where:

$$a = \frac{\sqrt{2}}{4}(d_{11} + d_{12} + id_{16} + id_{22}) \tag{3.14}$$

$$b = \frac{d_{15} - d_{24}}{2} \tag{3.15}$$

$$c = \frac{\sqrt{2}}{2}(d_{13} + id_{23}) \tag{3.16}$$

$$f = \frac{\sqrt{2}}{4}(d_{11} - 3d_{12} - 3id_{16} + id_{22}) \tag{3.17}$$

so that the whole nonlinear polarization is described by:

$$\begin{pmatrix} P_+ \\ P_- \\ P_z \end{pmatrix} = \chi^{(2)}_{CP} \begin{pmatrix} E_+E_+ \\ E_-E_- \\ E_zE_z \\ E_-E_z \\ E_+E_z \\ E_+E_+ \end{pmatrix} \tag{3.18}$$

We can now apply this new formulation to get the second-order nonlinear susceptibility tensor of any symmetry group, one just need to substitute the non-zero elements that corresponds for a given punctual group[1]. Because the CP basis is the eigenbasis for the measurement of the Berry Phase, the azimuthal selection rules of nonlinear processes can be straightforwardly obtained, for any given symmetry group. Defining Δm as:

$$\Delta m = \sum m_{output} - \sum m_{input} \tag{3.19}$$

and using the azimuthal dependence of equations 3.6 and 3.7, we can calculate the resulting additional quanta introduced in the azimuthal selection rule for each combination of the field components presented in equation 3.18. These are summarized in table 3.1.

Each nonzero element of the nonlinear tensor in the CP basis is thus associated with a single QPM condition and up to seven different QPM conditions can coexist, from $\Delta m = -3$ to $+3$, depending on the material symmetry. For example, for x-cut

---

[1] The computational code to calculate this has been published in https://github.com/Alex-l-r/QPM_BerryPhase_WGM/blob/master/CP_tensor.ipynb

		$Fdtal$					
SH		$++$ $(2m_F-2)$	$--$ $(2m_F+2)$	zz $(2m_F)$	$-z$ $(2m_F+1)$	$+z$ $(2m_F-1)$	$+-$ $(2m_F)$
$+$	$(m_{SH}-1)$	$+1$	-3	-1	-2	0	-1
$-$	$(m_{SH}+1)$	$+3$	-1	$+1$	0	$+2$	$+1$
z	(m_{SH})	$+2$	-2	0	-1	$+1$	0

Table 3.1: Table summarizing the combinations of different inputs (fundamental) and output (second harmonic) in CP basis and the additional quanta in azimuthal number selection rule they produce.

$LiNbO_3$ we have the following non-zero elements:

$$d_{11} = -33,\ d_{12} = 5,\ d_{13} = -5,\ d_{22} = 3,\ d_{23} = -3 \tag{3.20}$$

which leads to the following nonlinear tensor in CP basis:

$$\begin{bmatrix} \frac{\sqrt{2}}{4}(-28+3i) & \frac{\sqrt{2}}{4}(-48+3i) & \frac{\sqrt{2}}{2}(-5+3i) & 0 & 0 & \frac{\sqrt{2}}{4}(-28-3i) \\ \frac{\sqrt{2}}{4}(-48-3i) & \frac{\sqrt{2}}{4}(-28-3i) & \frac{\sqrt{2}}{2}(-5-3i) & 0 & 0 & \frac{\sqrt{2}}{4}(-28+3i) \\ 0 & 0 & 0 & \frac{\sqrt{2}}{2}(-5+3i) & \frac{\sqrt{2}}{2}(-5-3i) & 0 \end{bmatrix} \tag{3.21}$$

This tensor shows that different SHG processes with $\Delta m = \pm 1$ are expected: with copolarized TE fundamental and SH fields using the $\frac{\sqrt{2}}{4}(-28 \pm 3i)$ element, as detected experimentally by Lin *et al.* [67], and with cross-polarized modes using the $\frac{\sqrt{2}}{2}(-5 \pm 3i)$ element [93].

Aside of obtaining the Δm conditions of the natural QPM in any material, this approach also allows to give a new insight to the nonlinear weight of each field component combination. The weights K_+ and K_- introduced in equation 1.21 for zinc-blende materials can be now understood as the direct overlap of CP field components of input fields and nonlinear products. This greatly simplifies the evaluation of different processes, helping the design of the resonator to match the most efficient Δm

condition. In the next section we make a detailed analysis of this, applied to the $\bar{4}$-QPM condition.

3.4 Study of the $\bar{4}$-QPM Conditions in the Zinc-Blende Case

To detail the case of SHG in a III-V zinc-blende material microdisk resonator, we first write the nonlinear polarization in CP basis (equation 3.18) with the help of equation 3.13 applied to the case of zinc-blende materials:

$$\begin{pmatrix} P_+ \\ P_- \\ P_z \end{pmatrix} = \epsilon d_{14} \begin{bmatrix} 0 & 0 & 0 & -1 & 0 & 0 \\ 0 & 0 & 0 & 0 & i & 0 \\ i & -i & 0 & 0 & 0 & 0 \end{bmatrix} \begin{pmatrix} E_+E_+ \\ E_-E_- \\ E_zE_z \\ E_-E_z \\ E_+E_z \\ E_+E_+ \end{pmatrix} \tag{3.22}$$

We can see (using table 3.1) that a TM (E_z) polarized SH field can be generated from a E_+E_+ or E_-E_- combination resulting in a $\Delta m = +2$ and $\Delta m = -2$ respectively, as demonstrated experimentally [20].

From this, we can derive in the CP basis the expression of the nonlinear coupling coefficient for SHG, ζ_2 (introduced in equation **??**), which enters into account for the calculation of the conversion efficiency:

$$\zeta_2 = \frac{1}{4}\frac{\int d^3x \sum_{ijk} \epsilon\chi^{(2)} E^*_{2i} E_{1j} E_{1k}}{[\int d^3x\epsilon|E_1|^2][\int d^3x\epsilon|E_2|^2]^{1/2}} \; i,j,k = x,y,z \tag{3.23}$$

$$= \frac{id_{14}}{4}\frac{\int d^3x\epsilon E^*_{2z}(E^2_{1+} - E^2_{1-})}{[\int d^3x\epsilon|E_1|^2][\int d^3x\epsilon|E_2|^2]^{1/2}} \tag{3.24}$$

Inserting equation 3.6 and 3.7 into equation 3.23, in order to explicit the azimuthal dependence in the overlap integral, one can obtain directly the well-known $\bar{4}$-QPM condition $\Delta m \pm 2 = 0$. The coupling coefficients $K_\pm$ introduced by Kuo *et al.*, [19] can thus be attributed to the overlap integral of the SH mode with either spin up or spin down photon field components of the fundamental field.

The investigation of this overlap around fundamental and SH frequencies in this framework is very convenient to assess the efficiency of a given QPM condition and explore the use of modal phase-matching as reported in figure 3.3. To do so we plot the mode profiles of the fundamental fields ($E_{+/-}$) together with the first three radial orders of SH fields. The WGMs under scrutiny are chosen to satisfy the $\Delta m = +2$ condition but further calculations show that small changes in the azimuthal number barely modifies the distribution of the fields, so that the following analysis also suits to the $\Delta m = -2$ and can be generalized to other materials.

It is also important to remark that in III-V resonators, the large chromatic dispersion of TE and TM modes technically limits the number of accessible QPM conditions since energy conservation is not necessarily obtained. When investigating a nonlinear conversion between a fundamental TE mode and a SH TM mode with radial orders $r_F = r_{SH} = 1$ (upper plot and plain black line), the best overlap is obtained for the E_+ component ($\Delta m = 2$, red line) which is unfortunately forbidden by chromatic dispersion [47]. Then a weaker overlap with the E_- (blue line) should be considered.

The plot shows that an optimization of this later overlap should be possible by the use of microring instead of microdisks to push the E_- field to the outer side of the resonator.

Looking for higher radial order modes, the E_- field with $r_F = 1$ (middle graph) shows a very good overlap with SH fields with $r_{SH} = 2$. Also, the combination with the SH WGM of $r_{SH=3}$ gives a remarkable overlap. This use of higher radial order modes can compensate the chromatic dispersion which is otherwise achieved using periodic poling configurations [88].

Conclusion

In this chapter we have used the TSAM description of light to show that photons trapped in a planar circular cavity experience a Berry phase which depends on the direction of their spin along the symmetry axis of the resonator. This phase is found to be at the origin of the additional quanta appearing in the quasi-phase-matching condition of second-order nonlinear processes. We have shown that every element of the second-order nonlinear susceptibility tensor is associated to a unique QPM condition and is defined by the polarization of the input and output fields. We also illustrate our analysis in the $\bar{4}$-QPM case to discuss the efficiency of conversion depending on the overlap of the TSAM components of the fields.

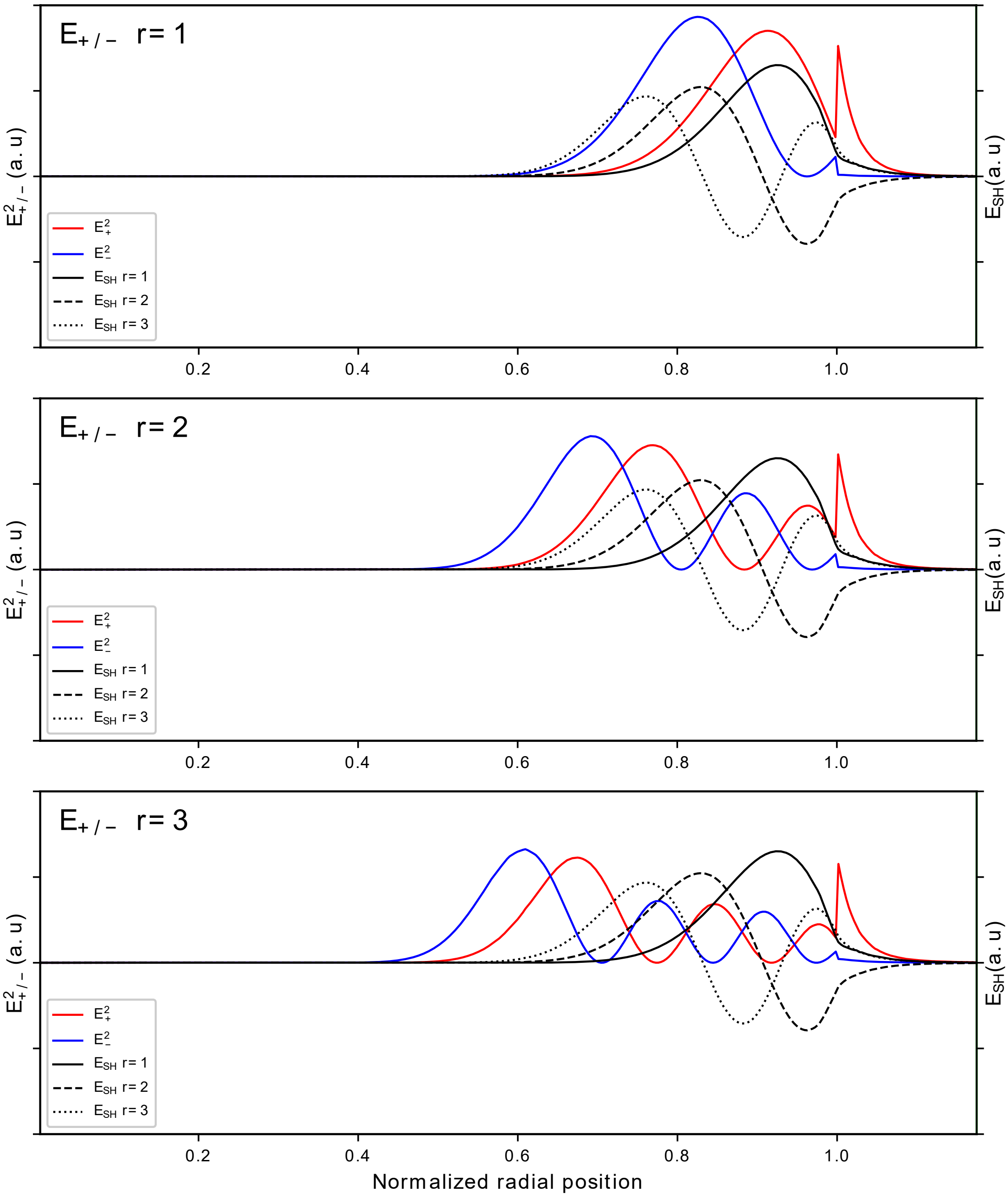

Figure 3.3: Representation of the radial profiles of $E_{\pm}$ components for the first three radial orders at fundamental wavelength, around 2 µm, compared to the E_z components of the first three radial orders of SH TM-polarized (1 µm) WMGs around 1 µm. The considered azimuthal orders are $m_F = 18$ and $m_{SH} = 38$ to satisfy the $\Delta m = +2$ condition. These profiles are qualitatively similar to $m_F = 20$ if $\Delta m = -2$ is to be considered.

Chapter 4

Fabrication and Characterization of GaP Integrated Devices

In chapter 2 we studied and proposed different configurations of fully integrated solutions for wavelength conversion. In this chapter we are going to discuss the fundamental building blocks of an integrated GaP-based photonic platform and the underlying technological processes. First we explore the use of different techniques to bond and encapsulate GaP and Si_3N_4 layers to prepare an encapsulated coupled microdisk. Part of the experimental work shown here has been done in the framework of the M2 internship of Jérémy Potet, which I co-supervised. Most technological developments have been made with the support of J. Le Pouliquen and K. Tavernier.

The design of our GaP photonic integrated circuit is based on the stack of the GaP photonic layer, containing resonant devices like disks and microrings and a passive layer of photonic circuitry of Si_3N_4 waveguides. The two layers are encapsulated into a transparent dielectric cladding such as SiO_2 or BCB. A sketch of the architecture is presented in figure 4.1. The optical coupling to the first PICs developed will be

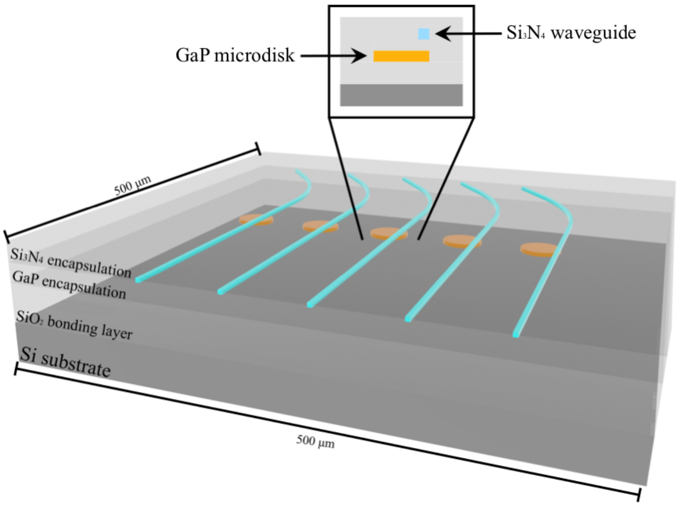

Figure 4.1: 3D sketch of the projected PIC design.

obtained by end-fire coupling at cleaved facets. The shortest stripes achievable with our cleave-tools are 500 µm large so that the technological process should guarantee high resolution of photonic structures in an area larger than this size.

In the following we address three important technological locks for the fabrication of such devices:

- The bonding of a GaP membrane onto a dielectric substrate.
- The development of an e-beam lithography process meeting the requirements of the PIC design.
- The encapsulation strategy.

4.1 Bonding Techniques

For all the processes described in previous chapters, we need a highly nonlinear material. As previously stated, our choice for the wavelength conversion is GaP, due to its strong $\chi^{(2)}$ performances and large band gap. Gallium phosphide based alloys are however hardly suited for strong photonic confinement due the similarity in the refractive index; for example $\mathrm{Al_0 \cdot 7\, Ga_0 \cdot 3\, P}$ only shows a 0.2 refractive index mismatch with GaP, making difficult the development of such a platform on the native GaP substrate.

During the last decade, the OHM team of FOTON institute has developed a unique know-how on growing GaP on Si. Even if it does not solve the photonic confinement issue, it facilitates the bonding process thanks to a better etching selectivity between GaP and Si compared to GaP and AlGaP. Allowing the bonding of GaP membranes onto host photonic substrate.

Gallium phosphide has a very similar lattice parameter compared to silicon (0.36% lattice mismatch), allowing a few dislocations epitaxial growth over hundreds of nm. The growth of a III-V material over a non-polar substrate is however expected to lead to the generation of specific structural defects called antiphase domains (APDs). These are regions where the lattice polarity is locally reversed, separated by planes of Ga-Ga or P-P misplaced bonds propagating through the material, called antiphase boundaries (APB). Thanks to the optimization of the epitaxial process [94, 37] and notably the use of vicinal 6°-off substrates, a good control on the generation of APDs has been reached. The FOTON institute also works at growing both APD-free GaP membranes on Si and mixed-polarity GaP membrane for the demonstration of random quasi-phase-matching [62].

Heterogeneous integration seems to be the solution to develop photonic components based on GaP. The GaP layer can be released from the Si substrate thanks to the differences in the chemical reactivity between Si and GaP. Two strategies are investigated to bond the GaP membranes onto a host substrate, the use of molecular

BCB Bonding

Process	Parameters
Cleaning Sample	Acetone + Isopropylic alcohol + DI water
BCB spin coat (2 steps)	1: 7 s, 500 min^{-1}, 500 s^{-2} 2: 23 s, 4000 min^{-1}, 4000 s^{-2}
BCB solvent drying	1 min 80 °C
BCB half cure	210 °C slow ramp 40 min, N_2 flux
Pressure bonding	Manual uniform and light pressure
BCB hard cure	250 °C slow ramp 1h, N_2 flux

Table 4.1: Table summarizing the process of the adhesive bonding using BCB.

bonding using silicon oxide (SiO_2) or the adhesive bonding with benzocyclobutene (BCB), a polymeric resin widely used in microelectronics with a refractive index similar to SiO_2.

4.1.1 BCB Adhesive Bonding

The bonding technique with BCB has been widely used in III-V semiconductor research thank to its ease of use [31]. BCB is a liquid polymer that can be easily spin-coated in the desired surface and then baked to become solid. This helps to reduce the roughness requirements of the bonded surfaces since BCB will adapt to its surface. The interesting property of BCB for bonding is its behaviour as a function of baking temperature. A 1 h baking at 250 °C makes the resin solid while the same process at lower temperature makes it half-cured, in a state where adhesion remains strong.

Our objective is the development of an adhesive bonding procedure of GaP membrane into dielectric substrate, without the use of a dedicated wafer bonding equipment. One of the main issues of this type of bonding is the formation of bubbles, trapped into the resin during the curing process. This can cause scattering of light in our photonic structure together with a mechanical stress into the bonded membranes. To reduce this issue, we have explored several parameters of the process.

We use the commercial solution of BCB *Cyclotene 3022-46* of Dow Chemicals. The resulting layers when used directly are too thick for our objectives thus we dilute the BCB with the same solvent as in the original formulation, trimethylbenzene, under its commercial name T1100. To obtain layers of 500 nm we need a dilution of 1:1 in volume with T1100. The preparation of the solution together with the reduction of the viscosity of the BCB introduces a lot of gas in the solution. After soft baking to evaporate the solvent, the occurrence of bubbles can become a detrimental issue. Different concentrations of the new solution only change the size of these bubbles but do not limit their number. In contrast, degassing with ultrasound the solution and filtering before use with a 0.2 µm filter has proved to be efficient as shown in figure 4.2.

Even though the optimization of the process drastically reduces the number of bubbles in the final result, it is not possible to remove all of them in the bonding of a 1 cm^2 sample. To limit the interaction between the evanescent tail of the confined modes and these bubbles, we decided to deposit a 1 µm thick layer of SiO_2 on top of the GaP layer prior to bonding. This layer also provides a better adhesion of the spin-coated BCB. The results we obtained with Si dummy samples are nice surfaces free of bubbles as big as 2 µm to 3 µm (figure 4.3). The process flow of our adhesive bonding technique is summarized in table 4.1.

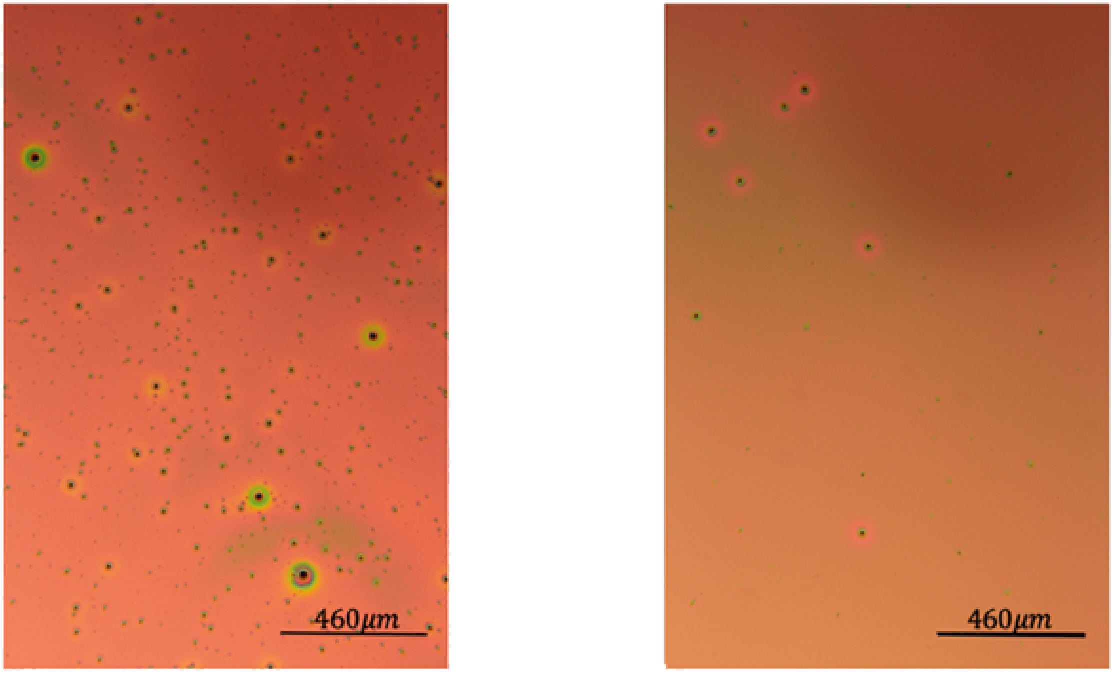

Figure 4.2: Optical microscope image of sample surfaces after BCB coating, before (left) and after (right) ultrasound degassing and filtration through a 0.2 µm membrane

4.1.2 Molecular Bonding Using SiO_2

Another approach to bond GaP membranes onto a host dielectric substrate is the use of molecular bonding. Depending on the bonding surfaces, there are different mechanisms. In our case, we make use of the procedure described by Nakanishi *et al.* [95], of SiO_2-SiO_2 bonding using hydrofluoric acid (HF) at room temperature. A few droplets of diluted HF are placed on the host substrate before pressing the samples together. During this bonding process, HF dissolves the SiO_2 at the interface, and after vaporization, the SiO_2 recrystallizes, trapping the H and F atoms in the matrix.

In this case the process begins by depositing a SiO_2 layer by PECVD on both the host substrate and the sample. Not only the surfaces have to be extremely clean but also the roughness has to be as low as possible. Roughness is a critical

Figure 4.3: Optical microscope image of an adhesive-bonded Si-Si sample showing a bubble-free interface.

SiO_2 Bonding

Process	Parameters
Cleaning Sample	Acetone + Isopropylic alcohol + DI water
SiO_2 PECVD	280 °C SiH_4(5%): 200 sccm, N_2O: 1000 sccm Ar: 40 sccm, N_2: 3000 sccm, 1900 mtorr
Molecular bonding	1% HF, 0.98 MPa
Substrate removal	RIE: SF_6: 22 sccm O_2: 11 sccm 1.3×10^{-1} mbar, 100 W 2: 5% TMAH wet etching at 80 °C

Table 4.2: Table summarizing the process of the molecular bonding using SiO_2.

parameter in bonding processes without a resin adhesive layer like BCB. To achieve molecular bonding, the roughness of both host and substrate should have an RMS[1] below 1 nm [96]. Regarding commercial Si wafers, roughness is usually below this value. However, the roughness of a GaP layer grown on Si is an issue since typically has a RMS of a few nanometres (figure 4.4 a)). Hence, it becomes mandatory to decrease the roughness of the GaP sample. The FOTON institute has developed a chemical-mechanical polishing (CMP) technique for GaP, achieving an RMS for GaP layers grown on Si below 1 nm (figure 4.4 b)) [97].

Then the 300nm layer of SiO_2 is deposited. Depending on the recipe, we can vary the stress of the SiO_2 layer. Higher proportion of SiH_4 with respect to N_2O results in a faster and less stressed growth while a more diluted silane gives a more constrained matrix but a flatter surface (figure 4.4 c)). Samples bonded using this SiO_2 peel off in a few hours. To solve this and obtain an stable bonded membrane, we deposit a low stress SiO_2 layer, with a roughness RMS of 3.3 nm(figure 4.4 d)) and we polish this layer to obtain a very good surface with just 0.7 nm of roughness RMS (figure 4.4 e)).

Before the bonding procedure, we clean the samples with a piranha solution (70 °C to 80 °C mixture of H_2SO_4 and H_2O_2) to also remove all organic residue that could be present. Once it is ready, we drop the HF solution of 1% w.t on the surface of the host substrate and then the GaP sample is placed facing down and pressure is applied. The concentration of the solution used will determine the etching rate of the SiO_2 and thus the strength of the bond, too diluted HF will result in a weak bond. This process can also be performed with another SiO_2 etchant like KOH but the much slower etching rate gives very weak bonding results.

---

[1] Root Mean Squared

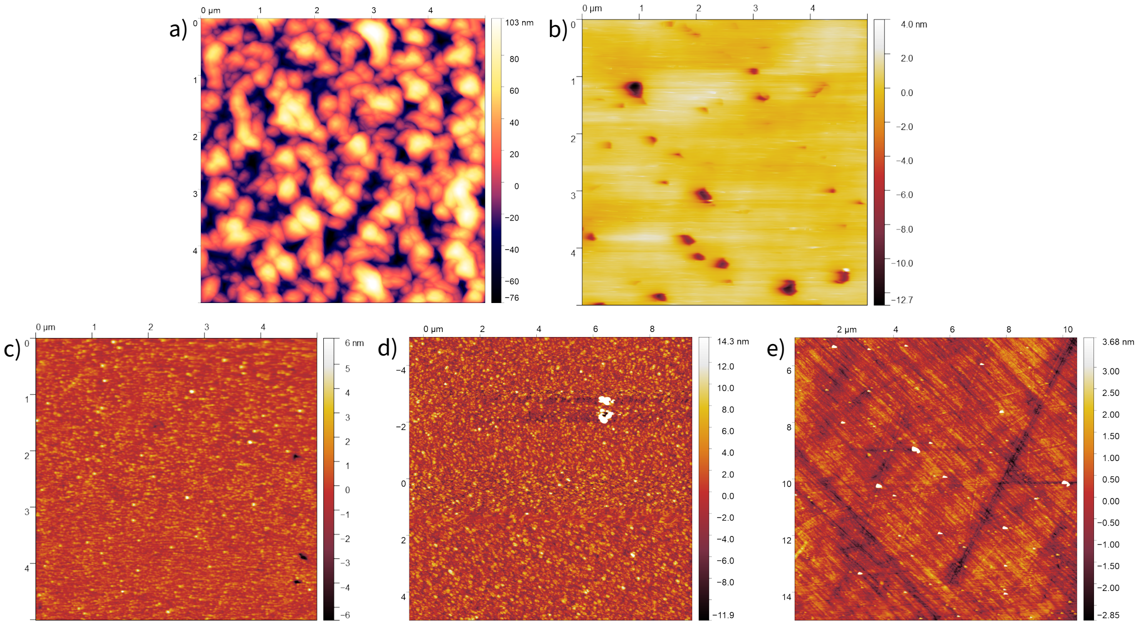

Figure 4.4: AFM images of a) GaP layer right after epitaxy, b) GaP layer after CMP processing; 1 nm RMS roughness can be reached, excluding holes generated in the GaP growth, c) constrained SiO_2 layer after growth, d) low stress SiO_2 layer before CMP and e) low stress SiO_2 layer after CMP.

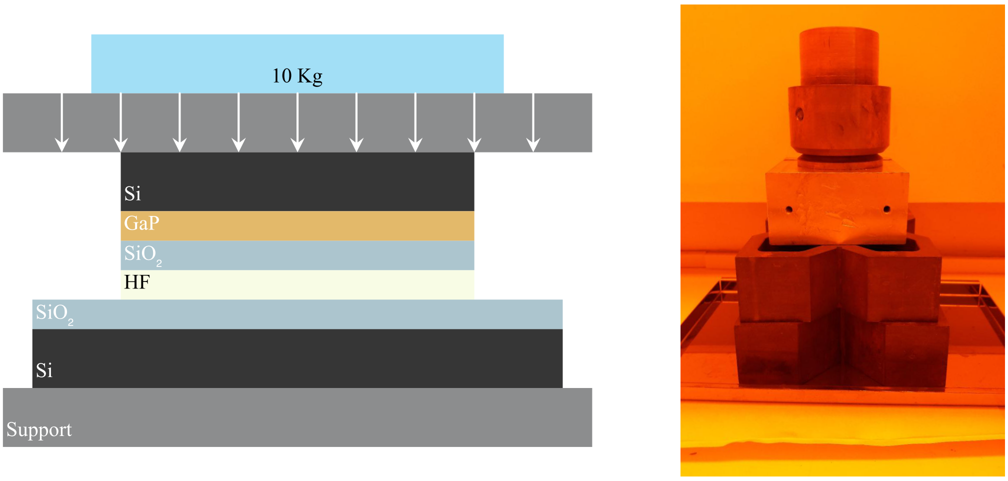

Figure 4.5: (a) Schematic view of the bonding system used. (b) Photography of the actual bonding system.

To ensure that the pressure is uniformly applied, the samples are glued to sample holders. Over the top holder a 10 kg weight is placed (figure 4.5). Since the size of the GaP samples used is 1 cm, this makes a total pressure of 0.98 MPa. This is important because the higher the pressure, the thinner the bonding interlayer. It is desirable to make this layer as thin as possible since it will contain hydrogen and fluorine impurities from the etching process.

After 24 hours, the sample is removed from setup and rinsed with deionised water. The last step consists in removing the growth substrate. This substrate has been first mechanically thinned to 100 µm before the bonding process to simplify this process. We etch the remaining substrate with reactive ion etching. Finally, the last micrometers are etched in a hot (80 °C) TMAH bath.

With the developed process, summarized in table 4.2, the bonding is very robust when performed on dummy Si wafers with an interface between the two SiO_2 layers that completely disappears after bonding as shown in figure 4.6. However, molecular

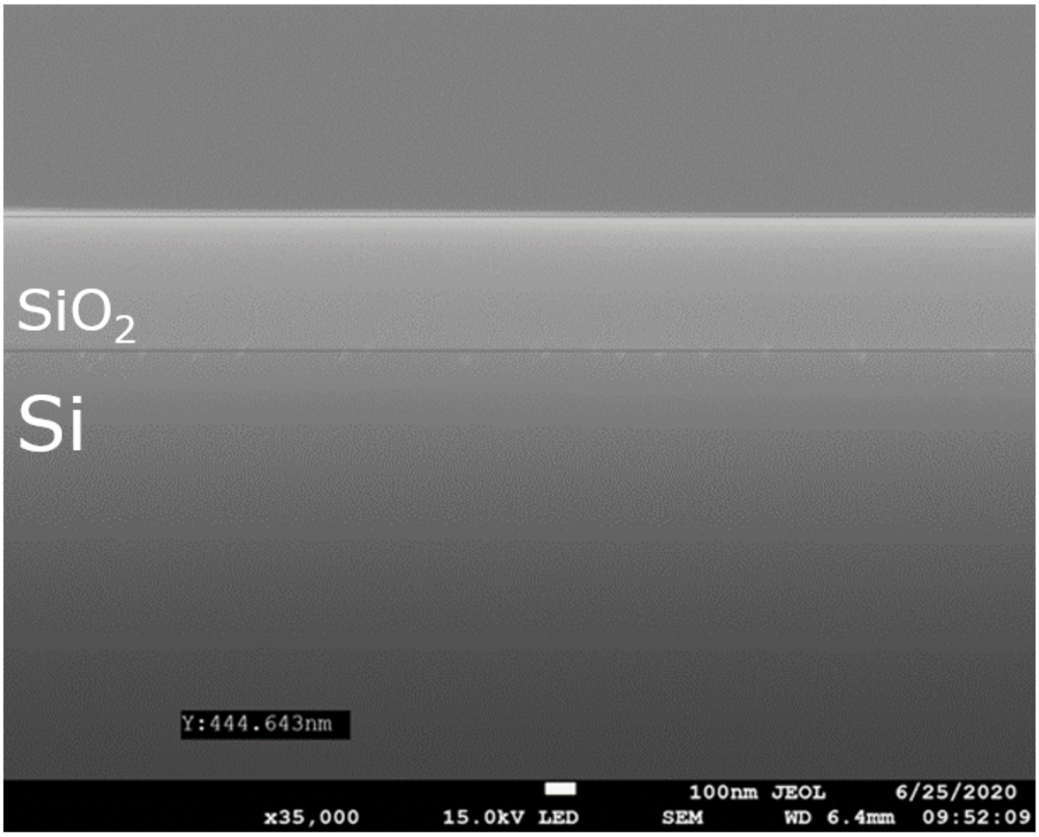

Figure 4.6: SEM image of the cut-section of a SiO_2-SiO_2 bonding.

bonding of GaP/Si sample always failed at the surface-removal step, where peeling of the GaP membrane is observed on most of the sample surface. We attribute this to the roughness of the bonding surface on the GaP side, still too large to make the bonding strong enough to support the stress on GaP membrane when releasing it from its silicon substrate.

4.2 Realization of the PIC components

4.2.1 E-Beam Lithography

In order to fabricate the components of the PICs showed in previous chapters, we need to use lithography techniques. Due to the small size of both guides and resonators, and the required alignment, electron-beam (e-beam) lithography is mandatory in our case. A limitation of most stepper lithography tools like the e-beam writers in the fabrication of large PICs is related to the concept of writing area (characterized by the field size parameter) which is the area in which the lithography is made by deflection of the e-beam only, without displacement of the samples. If the pattern to expose is larger than the field size, the stage holding the sample will move. This mechanical motion introduces a positioning error, known as stitching error, leading to misalignment issues. Our e-beam tool[2] shows a $50000 \times 50000 px$ grid with a field size adjustable between 50 µm to 800 µm and a stitching error of about 10 nm.

The GaP photonic devices fabricated so far at the FOTON institute were individual suspended microdisks [97]. They were processed using a complex multi-step process, involving a metallic lift-off with polymethyl methacrylate (PMMA) as e-

---

[2] Xenos XeDraw 2 EBL system

HSQ e-beam lithography

Process	Parameters
Sample preparation	5% HF deoxidation 15 s, 25 nm SiO_2 layer
HSQ Spin coating	30 s, 2000 min^{-1}, 1000 s^{-2}
HSQ Baking	30 min, 200 °C in oven
E-beam exposure	30 keV, 200 pA, 1100-1400 $mC\,cm^{-2}$
Development	30 s developing with AZ400K

Table 4.3: Table summarizing the process of the e-beam lithography using HSQ.

beam positive resist. In this process, a small field size of 200 µm was used during the lithography to optimize the definition of the patterns. Towards the development of photonic integrated circuits including GaP devices and passive circuitry, both a simplification of the GaP processing and the use of larger field sizes are necessary. These are the motivations behind the development of a lithography procedure using hydrogen silsesquioxane (HSQ) as electro-sensitive resist. The use of the largest field-size achievable with our e-beam tool allows us to design PICs in areas of 800×800 µm, without misalignment issues.

The first advantage of HSQ is that it is a negative resist, contrary to PMMA. The HSQ areas exposed to the e-beam remain after the development and can be used as hard mask for the etching step. The suppression of the lift-off is expected to reduce the lateral roughness of our devices, one of the main sources of losses in our photonic devices. In addition, after the first tests, the contrast properties of the HSQ resist seem compatible with the lithography of patterns using the 800 µm field size of the e-beam total as shown in figure 4.7. The only cons in the use of HSQ is the need of

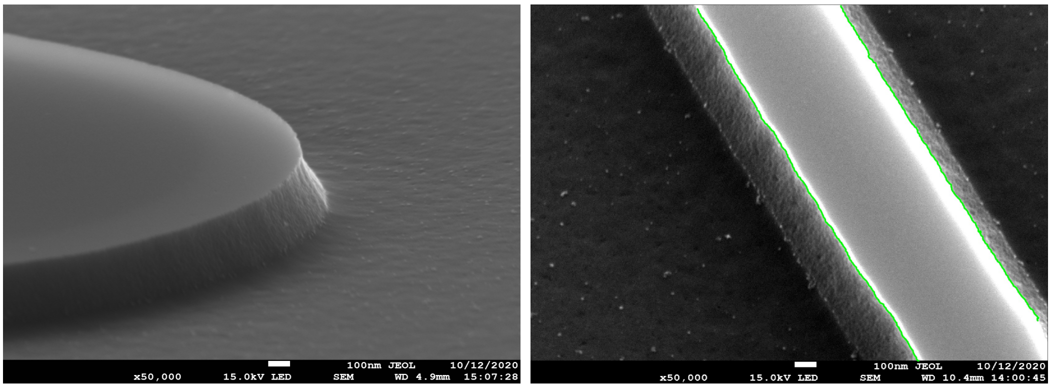

Figure 4.7: SEM images of a microdisk (left) and a waveguide (right) etched in silicon using HSQ as photoresist. We can see that our process gives very good lateral roughness.

growing a thin SiO_2 layer to improve the resist adhesion.

The lateral roughness of test devices has been measured to 4 nm RMS as shown in figure 4.7 and no evidence of pixelization was observed, even in circular patterns. The summary of the HSQ lithography process is given in table 4.3.

4.2.2 Encapsulation of Components

To achieve the full encapsulation of the PIC, we need a transparent dielectric, with a low refractive index to act as a cladding of the configuration. As demonstrated in chapter 2, we no longer need to have the same material for our microdisk that for the coupling waveguides. This opens up the possibility of using Si_3N_3 as the material of the second layer of the PIC. Silicon nitride can be deposited by PECVD at 280 °C, allowing the use of two possible platforms for the encapsulation of the first photonic layer, BCB and SiO_2. Since both of them have similar refractive index, they are indeed compatible, and both used in the same scheme [33].

The key difference between these two encapsulation materials lies in their deposition process. Because PECVD is used for SiO_2, the deposition is conformal so that the SiO_2 surface will follow the profile of the buried photonic components. A planarization process should thus be developed to recover a flat surface before adjusting the encapsulation layer thickness to the desired one. On the other hand, BCB is deposited by spin coating so that planarization is possible during the deposition process if the layer is thick enough.

4.2.2.1 Encapsulation and planarization of PICs using BCB

To reduce the cost of process development, the different process steps were studied with dummy samples containing Si waveguides processed by UV photolithography. These steps are summarized in table 4.4.

Figure 4.8 shows the scheme of the planarization process flow. We first take samples with stripes of 300nm thick and we spin coat them with BCB to uniformly distribute the resin. Then the sample is placed in the oven with a slow temperature ramp under a nitrogen flux. This N_2 atmosphere is very important because at these temperatures, the presence of oxygen would oxide the BCB. Profilometer measurements after this process reveal that although notoriously reduced, the topology of the stripes is still present at the surface, with heights of 15 nm for thin waveguides, of 1 µm to 3 µm wide. For wider waveguides, from 25 µm to 40 µm wide, the height is 35 nm.

Since a single BCB layer is not enough to fully planarize the sample, a second layer of BCB is spin coated in the same conditions. The baking step for this second layer will be made up to 250 °C to completely cure BCB. The results here are far better, completely eliminating the shape of guides in the surface and leaving only the natural roughness of surfaces of this kind of resins. After this two-step encapsulation, BCB Encapsulation

Process	Parameters
Cleaning Sample	Acetone + Isopropylic alcohol + DI water
BCB 1st spin coat	1: $7\,\mathrm{s}$, $500\,\mathrm{min}^{-1}$, $500\,\mathrm{s}^{-2}$ 2: $23\,\mathrm{s}$, $4000\,\mathrm{min}^{-1}$, $4000\,\mathrm{s}^{-2}$
BCB solvent removal	2 min 130 °C
BCB half cure	210 °C slow ramp 40 min, N_2 flux
BCB 2nd spin coat	1: $7\,\mathrm{s}$, $500\,\mathrm{min}^{-1}$, $500\,\mathrm{s}^{-2}$ 2: $23\,\mathrm{s}$, $4000\,\mathrm{min}^{-1}$, $4000\,\mathrm{s}^{-2}$
BCB solvent removal	2 min 130 °C
BCB hard cure	250 °C slow ramp 1h, N_2 flux
BCB RIE etching	SF_6: 22 sccm O_2: 11 sccm 1.3×10^{-1} mbar, 100 W, bias: 200 V

Table 4.4: Table summarizing the process of the sample encapsulation using two layers of BCB.

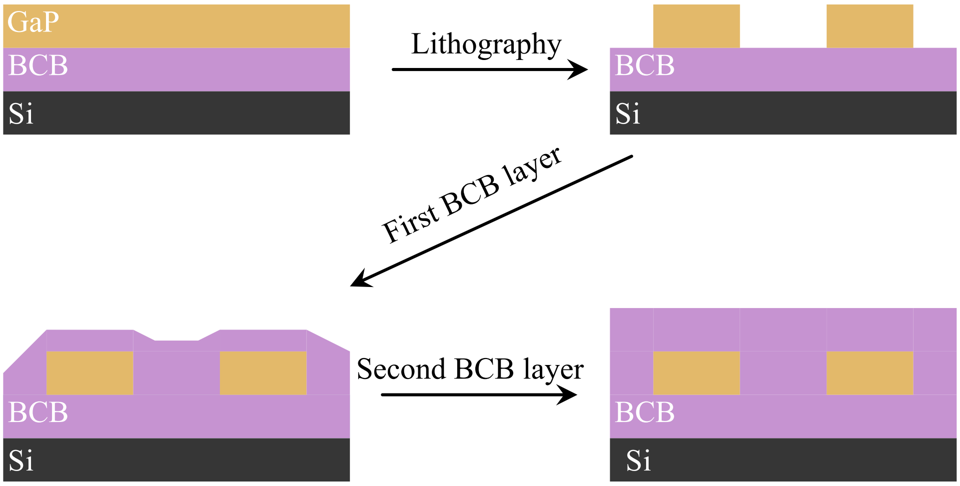

Figure 4.8: Schematic process of the encapsulation of waveguides using BCB.

the BCB layer is 5400 nm thick as measured by reflectometry.

Since our target architecture is made of two photonic layers, evanescently coupled one very important aspect is to reduce the thickness of the encapsulation layer down to a few hundreds of nm. To do this, we need to etch the BCB after it has been planarized since the etching will be conformal. The best technique to etch cured BCB is with *reactive ion etching* (RIE). The plasma will be composed of a mixture of SF_6 and O_2. With a etching rate of $280\,\mathrm{nm\,min^{-1}}$. Aside of the calculated etching rate during the calibration test, the etched thickness is also controlled through in-situ reflectometry. This allows us to stop the etching process at the desired distance between the two layers of the PIC.

Especially, we were able to etch down the BCB layer so that the BCB surface is 160nm above the top of the buried waveguides, in agreement with the values calculated in chapter 2 (figure 4.9).

4.2.2.2 SiO_2 Encapsulation

The second option for encapsulation is the use of SiO_2 (figure 4.10). Again, its high transparency and wide use in Si technological processing have made of it one of the main materials for encapsulation in integrated photonics [32]. The technological lock for this approach lies in the conformal deposition of PECVD SiO_2. Isotropic RIE is not enough to flatten the surface so that CMP has to be considered.

Like for the BCB samples, we perform this study with dummy samples of Si waveguides. A 600 nm thick SiO_2 layer is deposited to bury the waveguides. The CMP process is made with a suspension of CeO nanoparticles. Figure 4.11 shows a cross-section SEM image of a buried waveguide after the planarization process. A 200 nm thick SiO_2 layer can be measured above the waveguide. However, a residual

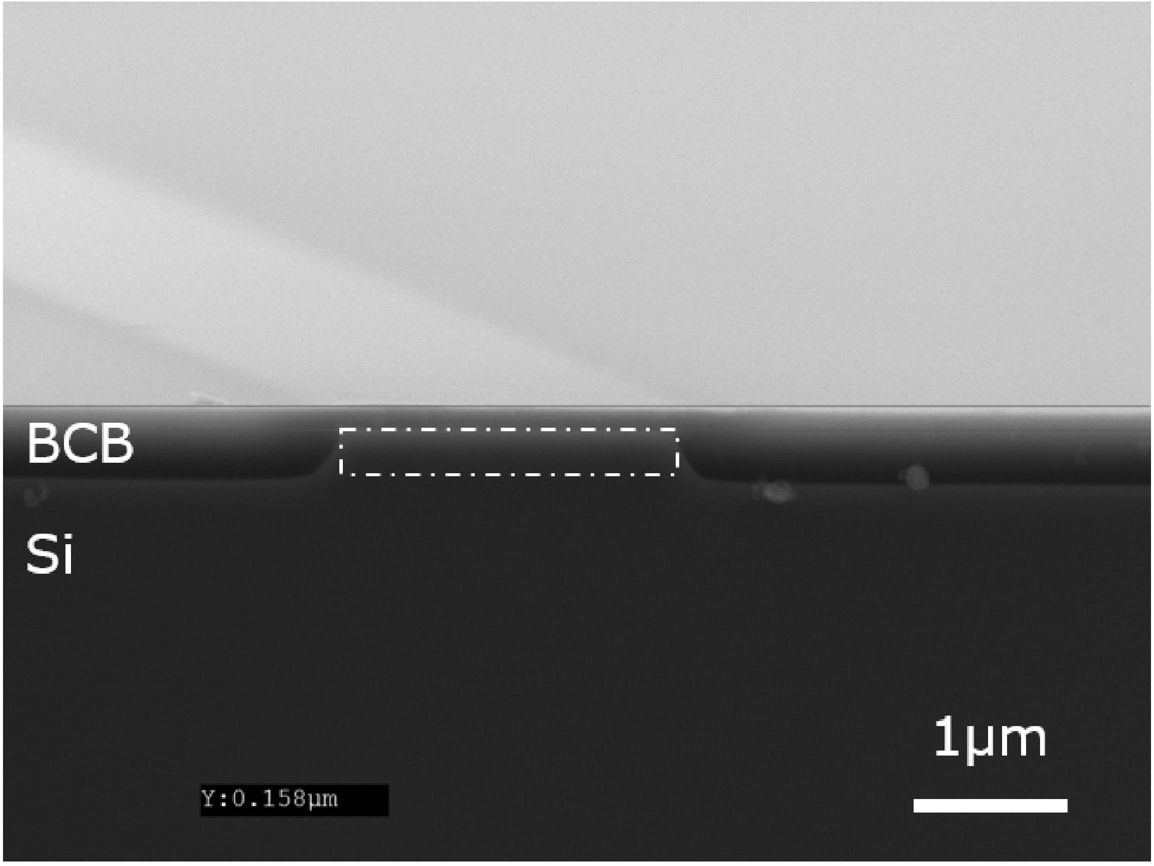

Figure 4.9: SEM image of Si waveguide encapsulated using BCB, with 158 nm of BCB over the guide.

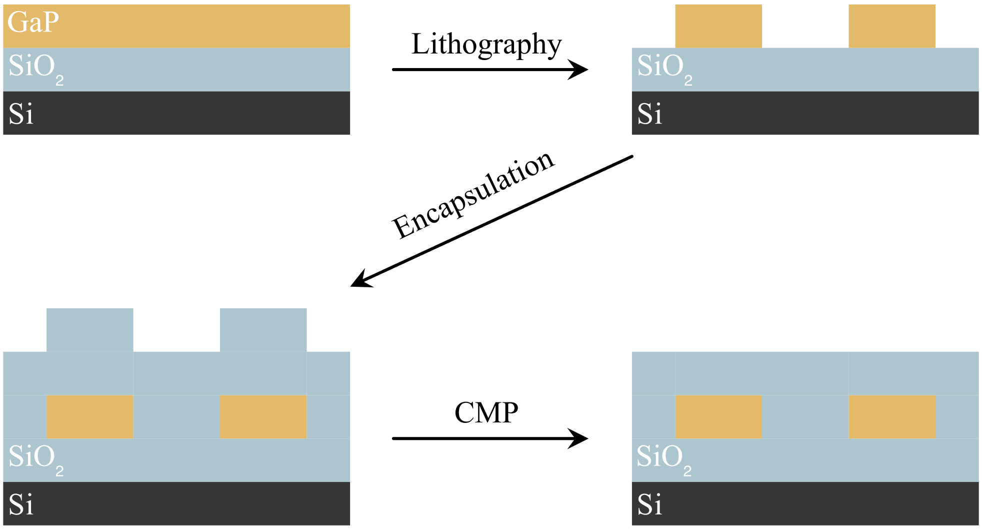

Figure 4.10: Schematic process of the encapsulation of waveguides using SiO_2.

SiO_2 Encapsulation

Process	Parameters
Cleaning sample	Acetone + Isopropylic alcohol + DI water
SiO_2 PECVD	280 °C SiH_4(5%): 200 sccm, N_2O: 1000 sccm Ar: 40 sccm, N_2: 3000 sccm, 1900 mtorr
Chemical-Mechanical Polishing	CeO nanoparticles suspension in water
SiO_2 RIE etching	SF_6: 30 sccm 1.3×10^{-1} mbar, 40 W, bias: 65 V

Table 4.5: Table summarizing the process of the sample encapsulation using SiO_2.

topology is observable suggesting that the encapsulation layer should be thicker to enable full planarization with CMP.

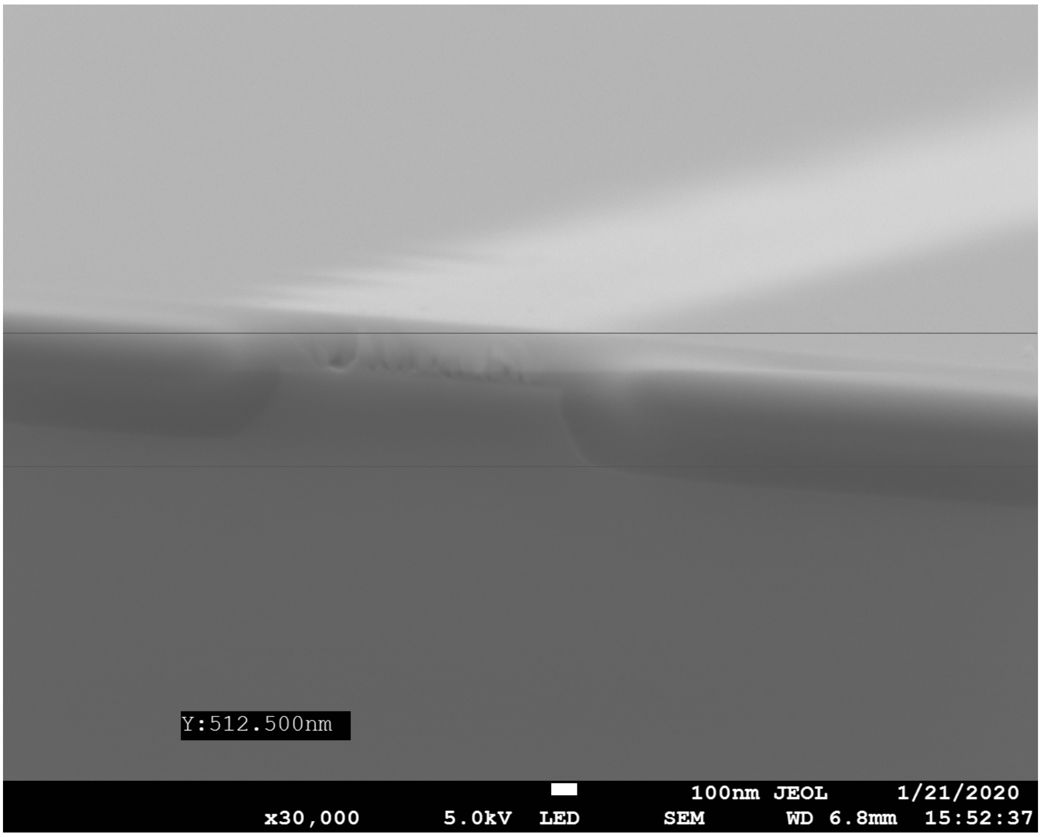

Figure 4.11: SEM image of Si waveguide encapsulated using SiO_2 after grinding with CeO to planarize the surface, with 200 nm of SiO_2 over the guide. Blurriness is due to the charging effect of SiO_2.

Conclusions

In this chapter we have defined a global process flow for the fabrication of GaP-based nonlinear PICs. Each step has been developed independently and validated. Two strategies have been defined for both bonding of GaP membranes and encapsulation of photonic layers. For these two steps, a BCB and a SiO_2 based solutions are validated. For both procedures we were able to fully encapsulate waveguides and control the thickness of the cladding layer.

We have also started the study of electron beam lithography methods to etch the necessary part for the designed schemes such as microdisk resonators and waveguides using HSQ as resist. All the developed procedures are compatible with the designs proposed in chapter 2.

Unfortunately, most of the experimental work of this chapter was carried out at the beginning of 2020. Due to the COVID-19 global crisis we have not been able to fabricate and demonstrate experimentally a GaP-based PIC during the duration of the PhD. Hence, the next objective is the fabrication of the first GaP-based 3D PIC at the FOTON institute. Also, the use of HSQ as encapsulation material, while more expensive could be an investigation option.

Chapter 5

Gallium Phosphide Nonlinear Photonics for THz Generation

Terahertz (THz) waves are the part of the electromagnetic spectrum lying between microwaves and mid-infrared optical waves with frequencies ranging from 300 GHz to 30 THz(wavelength spanning from 10 µm to 1 mm). These frequencies correspond to the intermolecular rotations and vibrations and thus a lot of molecules have their fingerprint in this spectral region. This motivates the research of THz devices for sensing applications [98].

Large progresses have been achieved in THz technology during the last decades. For the upper part of the THz regime, integrated sources emitting in the few-THz regime are mainly based on quantum cascade lasers (QCL), usually in cryogenic conditions. But the Reststrahlen band of III-V semiconductors, the spectrum between 5 THz to 15 THz remains mostly uncovered, the longer wavelength for a cryogenic QCL being 10 THz [59].

Another approach for THz generation is the use of nonlinear processes, notably difference frequency generation (DFG). This has been integrated in existing QCL to generate 5 THz at room temperature. [60].

Here we focus on THz generation in the Reststrahlen band of semiconductors. In this band, THz field strongly couples to phonon resonances and can form a quasi-particle called surface phonon polariton. We will demonstrate here that we can take advantage of this specific light propagation to design novel schemes of photonic devices for THz generation. We choose to study GaP-based devices as this material shows one of the largest Reststrahlen band (1 THz for GaP against 0.7 THz for GaAs) centered around 11.5 THz. As described in previous chapters, it also shows excellent optical properties for nonlinear processes such as low two-photon absorption for optical wavelengths larger than 1 µm. Moreover, GaP can be integrated monolithically on silicon as explained in chapter 4. This can further allow integration of driving and read-in/out electronics required and large-scale integration.

In this chapter we aim to investigate the THz generation in the Reststrahlen band of GaP (11 THz to 12 THz) through DFG using two different pump spectra regimes, near infrared and middle infrared.

5.1 The Reststrahlen Band

The Reststrahlen band is the region of the electromagnetic (EM) spectrum corresponding to the frequencies between the transversal-optical (TO) and longitudinal-optical (LO) phonon frequencies. It is characteristic of polar semiconductors, and its size is related to the polarity of the covalent bonds present in semiconductors. While a large number of photonic and electronic devices rely on III-V semiconductors, this region is usually avoided due to the strong phonon absorption and the high

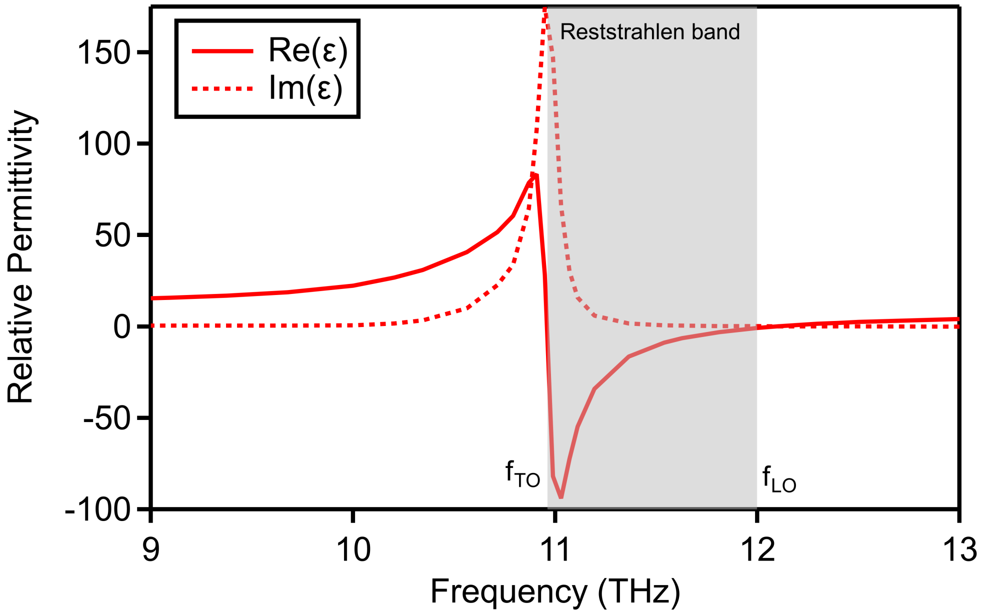

Figure 5.1: Real and imaginary part of the permittivity of GaP. The Reststrahlen band, grey area, corresponds to the 11 THz to 12 THz interval where the real part is negative.

reflectivity of the materials in this frequency range.

When approaching the TO frequency from lower frequencies, the permittivity passes from the static dielectric constant ε_s to an exponential growth until exhibiting a discontinuity at the TO frequency, becoming negative, like in metals, figure 5.1. Above this frequency, the permittivity remains negative until the frequency reaches the LO frequency. At higher frequencies, the permittivity will approach ε_∞ and hence between TO and LO frequencies light starts to strongly couple with the phonons. This increases the losses drastically since we have very high absorption inside the material but it also allows to have sub-wavelength confinement with electromagnetic (EM) waves propagating through the surface as *Surface Phonon Polaritons* (SPhP), these modes will be detailed in the following.

Another effect that arises when approaching this TO frequency is the magnifi-

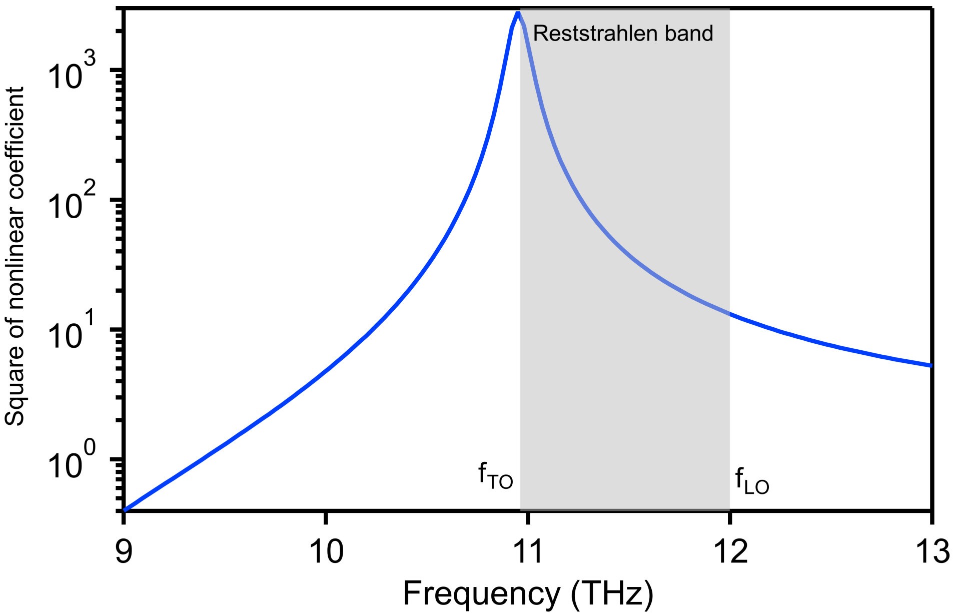

Figure 5.2: Resonance of the nonlinear susceptibility coefficient, d_{14} around 11 THz.

cation of the second-order nonlinear susceptibility 3 orders of magnitude due to the resonance of EM waves with the ionic displacement as shown in figure 5.2 [99]. This can increase by the same magnitude the output power of second-order nonlinear processes [100].

5.2 Terahertz Surface Phonon Polariton Confinement in the Reststrahlen Band

As stated before, we are going to make use of the negative permittivity in the Reststrahlen band to guide the terahertz modes through surface phonon polaritons(SPhP). It is analogous to surface plasmon polariton in metal/dielectric interface with the difference that collective oscillation of electrons is replaced by a collective ionic motion. In our case we will have a GaP stripe acting as a metal surrounded by a transparent

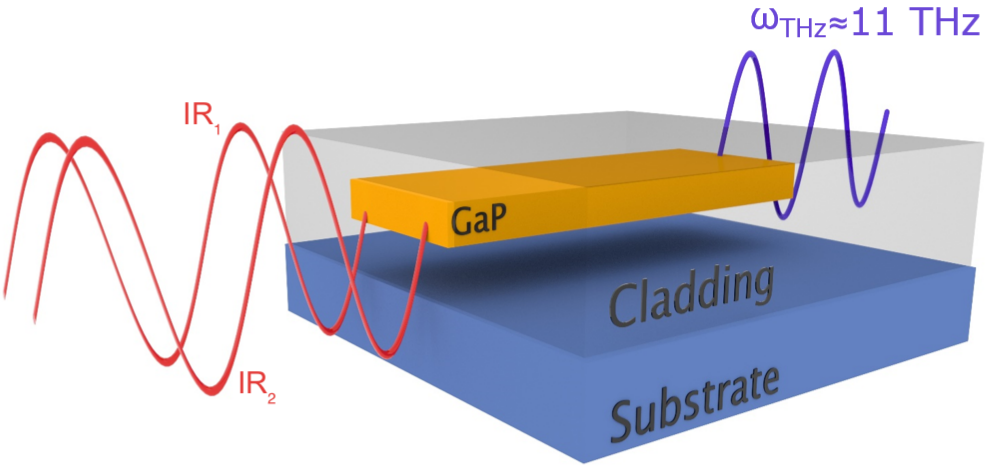

Figure 5.3: 3D sketch of the designed GaP stripe for THz generation.

dielectric5.3. Since we have already used it in previous chapters and the losses are low in the terahertz regime, a cyclic olefin copolymer (COC) is our choice.

Surface phonon polariton modes can be described with the same notation that for plasmon polariton modes [101] since the only difference is the origin of the negative permittivity value. We consider a symmetrical thin GaP guide of finite width encapsulated by a homogeneous transparent dielectric material as shown in figure 5.3. We can then divide the supported modes into four families depending on the symmetry of their fields. These four families are ss, as, sa and aa (figure 5.4), where a means antisymmetric while s is symmetric. This notation can be extended to describe leaky and higher order modes. Since we will not consider the latter modes in this work, the indexes b and 0 for bounded and first order modes are omitted. Also, at the frequencies and geometrical sizes that we study, as modes are not considered either.

All the simulations needed to obtain the propagating modes are made with FEM methods, similar to those made in chapter 2. In this case, to properly simulate the

SPhP modes, we need an extremely small mesh at the interface between GaP and COC since the electric field changes very abruptly.

Each of these modes will have different field distributions and dispersions and thus the optimization process is not only bounded to the geometry design but also to the choice of the THz mode under scrutiny. In figure 5.4 we can see that depending on the chosen mode, we will have more power in the vertical surfaces or in the horizontal surfaces. Also, the amount of field penetrating into GaP will be different for each mode. Like explained for the second harmonic process, one of the crucial terms to optimize is the overlap between the nonlinear polarization of the pump beams and the generated modes. While in the COC part the terahertz wave is going to propagate as a EM mode, inside GaP is going to do so coupled with phonons, this means that losses inside GaP are going to be very high. While with certain geometrical optimization one could achieve a low loss propagation by reducing the amount of the EM field inside the stripe, this would reduce the efficiency of the nonlinear second-order process. Therefore, a good balance between this two processes is needed to achieve an efficient device.

In the next section we will see which mode fits better the requirements for the second-order nonlinear process.

5.3 THz Generation Through Difference Frequency Generation

As introduced in section 1.4.2, we can use two pump beams separated by a few terahertz to benefit from the DFG in gallium phosphide. We can obtain the nonlinear

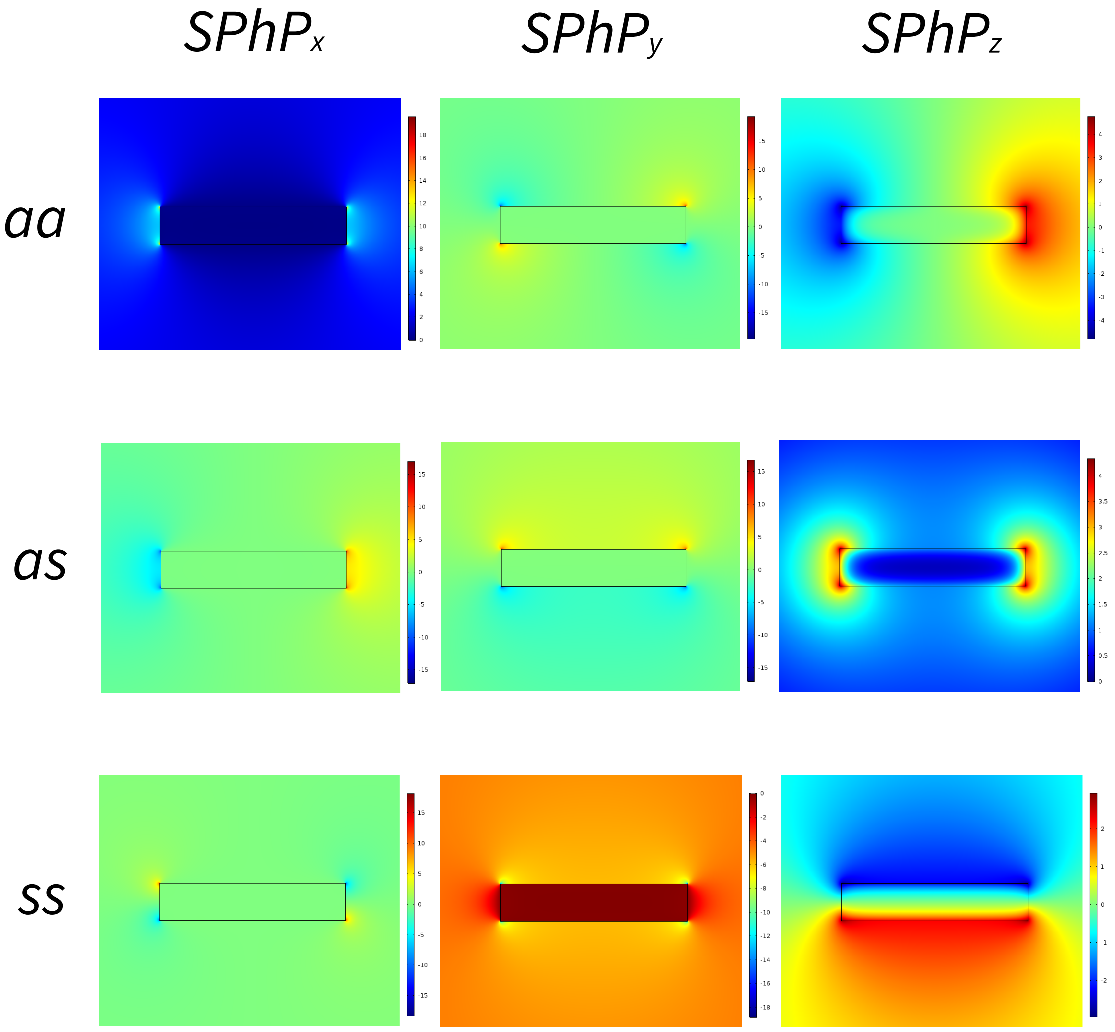

Figure 5.4: Electric field distribution for the three electric field components of the *aa*, *as* and *ss* 11 THz SPhP modes in a $8 \times 1.7 \mu m$ GaP stripe propagating in the z direction.

polarization using equation 1.19. Depending on the chosen pump modes this nonlinear polarization will have different modal distributions. Ruan *et al.*, obtained the coupled-mode equations for the DFG process in a rectangular waveguide [79], solving them and integrating along the propagation distance (L) one obtains:

$$\eta(L) = \frac{c_{THz}}{c_{IR_1}c_{IR_2}}\frac{\omega_{THz}^2|\kappa_{THz}|^2}{16}|\frac{e^{\frac{\alpha_{THz}-\alpha_{IR_1}-\alpha_{IR_2}}{2}+i\Delta\beta L}-1}{\frac{\alpha_{THz}-\alpha_{IR_1}-\alpha_{IR_2}}{2}+i\Delta\beta L}|^2 e^{-\alpha_{THz}L} \tag{5.1}$$

where c_j is the time-averaged power of the mode, in lossless conditions $c_j = 1$ so we will consider the terms corresponding to the pump beams as 1 while in the THz case need to be computed for each case. $\Delta\beta$ corresponds to the propagation constant mismatch $\Delta\beta = \beta_{IR_1} - \beta_{IR_2} - \beta_{THz}$ and α_j is the power loss coefficient for the given mode. κ_{THz} corresponds to the nonlinear coupling coefficient between the nonlinear polarization and the THz mode electric field distribution:

$$\kappa_{THz} = \int P_{NL}(E_{THz,tranversal} - E_{THz,longitudinal})dz \tag{5.2}$$

In order to maximize the conversion efficiency three parameters dare to be optimized:

- The nonlinear coupling constant, κ_{THz}, depends on two factors: i) the nonlinear susceptibility, in this case we want to be as close as possible to the TO phonon resonance to maximize its value; ii) the overlap between the THz mode and the nonlinear polarization, this term will depend on the mode profiles of the SPhP and IR waves but also on the crystallographic direction.
- The phase-matching will be optimized for the $\Delta\beta = 0$ condition. As described in equation 1.23, this condition can be simplified due the large difference in

wavelengths between pumps and THz to $n_{THz} = n_g$ where the latter is the group index of the IR modes.

- The losses of the THz mode, which are expressed as the α_{THz} term, this will determine the length of our guide for which the efficiency will be maximum. If we consider $\Delta\beta = 0$ the length of highest efficiency is $L_{max} = 2ln(\alpha_{THz})/\alpha_{THz}$.

5.3.1 Strip Waveguides

The configuration that we are going to study is a GaP stripe encapsulated by COC. Although with SPhP we can achieve subwavelength confinement and thus larger mode overlap, a too small stripe would cause a large phase mismatch. Of the three SPhP modes supported by the GaP stripe (figure 5.4), the *aa* and the *as* modes are extremely lossy, with attenuation constants of 400 and 1000 dB/cm while for the *ss* mode this value is less than 3 dB/cm. We will focus on the latter in the following.

In the DFG in the optical regime, the usual direction is the [110], the reason for this can be deduced with the expression of the nonlinear polarization of two IR beams. With z as the propagation direction (longitudinal component) and x and y as the horizontal and vertical directions (transversal components) in this direction we have:

$$\begin{pmatrix} P_z \\ P_x \\ P_y \end{pmatrix} = \epsilon d_{14} \begin{bmatrix} 0 & 0 & 1 & 0 & 0 & 0 & 1 & 0 & 0 \\ 0 & 0 & 0 & 0 & 0 & -1 & 0 & -1 & 0 \\ 1 & 0 & 0 & 0 & -1 & 0 & 0 & 0 & 0 \end{bmatrix} \begin{pmatrix} E_z^{IR_1} E_z^{IR_2} \\ E_z^{IR_1} E_x^{IR_2} \\ E_z^{IR_1} E_y^{IR_2} \\ E_x^{IR_1} E_z^{IR_2} \\ E_x^{IR_1} E_x^{IR_2} \\ E_x^{IR_1} E_y^{IR_2} \\ E_y^{IR_1} E_z^{IR_2} \\ E_y^{IR_1} E_x^{IR_2} \\ E_y^{IR_1} E_y^{IR_2} \end{pmatrix} \tag{5.3}$$

Since we can consider the longitudinal component of the IR modes zero unless in very high photonic confinement conditions, this only leaves the following combinations with the non-zero elements of the nonlinear susceptibility tensor: a TE(E_x)+TM(E_y) combination to produce a nonlinear polarization with its non-zero component in the horizontal direction, P_x, suitable to overlap with TE modes; and a TE(E_x)+TE(E_x) combination to produce a nonlinear polarization P_y, adequate to overlap with TM modes.

If now we take a look at the modal profiles of the THz SPhP modes, figure 5.4, we see that the transversal, x and y, components are zero in the GaP and thus only the longitudinal component is exploitable. Then, none of the combinations along the [110] are suitable for SPhP modes generation. To solve this, we propose to turn 45° the propagation direction and thus be aligned with the [100] direction. If we write the nonlinear polarization after rotating the nonlinear susceptibility tensor we have:

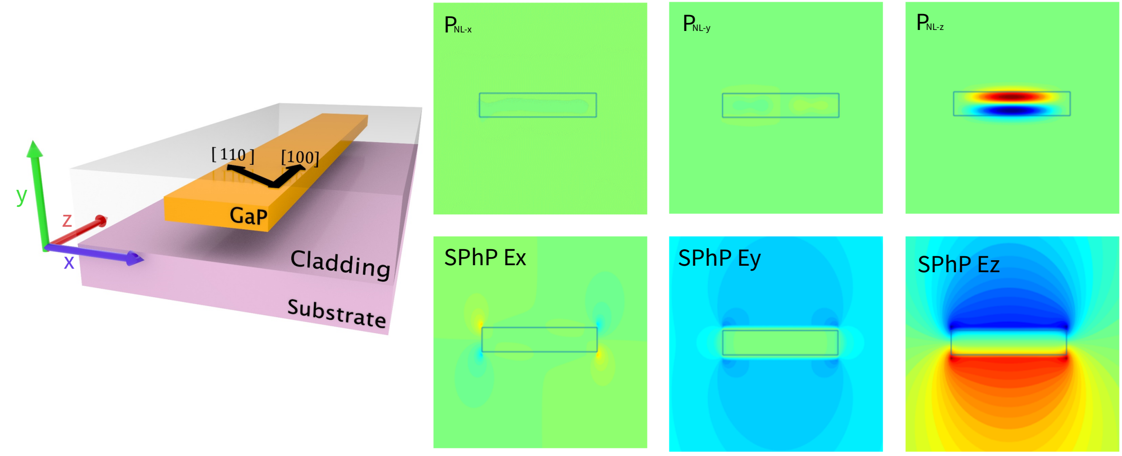

Figure 5.5: Modal profiles of the nonlinear polarization of the combination of TM-TE m-IR modes in the [100] propagation direction compared to the electric field components of the SPhP. A 3D sketch (left) is place for the sake of clarity.

$$\begin{pmatrix} P_z \\ P_x \\ P_y \end{pmatrix} = \epsilon d_{14} \begin{bmatrix} 0 & 0 & 0 & 0 & 0 & 1 & 0 & 1 & 0 \\ 0 & 0 & 1 & 0 & 0 & 0 & 1 & 0 & 0 \\ 0 & 1 & 0 & 1 & 0 & 0 & 0 & 0 & 0 \end{bmatrix} \begin{pmatrix} E_z^{IR_1} E_z^{IR_2} \\ E_z^{IR_1} E_x^{IR_2} \\ E_z^{IR_1} E_y^{IR_2} \\ E_x^{IR_1} E_z^{IR_2} \\ E_x^{IR_1} E_x^{IR_2} \\ E_x^{IR_1} E_y^{IR_2} \\ E_y^{IR_1} E_z^{IR_2} \\ E_y^{IR_1} E_x^{IR_2} \\ E_y^{IR_1} E_y^{IR_2} \end{pmatrix} \tag{5.4}$$

Under the same assumption of the small longitudinal components of the IR fields, we find that the only combination with the non-zero elements of the tensor is a TE(E_x)+TM(E_y) to produce the nonlinear polarization in the longitudinal direction P_z, figure 5.5, and thus suitable for the generation of SPhP through the DFG process.

This SPhP-mediated DFG process can be obtained at different input wavelengths in different parts of the IR spectrum. While the size of our waveguide only allows for first order terahertz modes, for the pump IR modes the waveguide is clearly multimode. We thus need to do a selection of the right modes to achieve not only phase-matching but also the maximum overlap possible. Looking at the shape of the *ss* mode we can see that to optimize overlap we need to use at least one IR mode of vertical order equal to one.

To maximize the conversion efficiency of the nonlinear process, κ must be increased by maximizing the THz field penetration into GaP. However, the more the THz field penetrates inside GaP, the higher the losses are, as shown in figure 5.6. The generated THz output power is proportional to κ^2 but also depends on losses through attenuation and phase-matching as expressed in equation 5.1. The problem of a high losses and high overlap configuration is that the high efficiency is obtained only after a long propagation distance. Hence, the generation of a significant THz output power requires a careful trade-off between THz absorption and THz field penetration into GaP.

For pump beams in the n-IR, we combine a TM mode of 1498.96 nm with a TE mode of 1586.45 nm. With these wavelengths, the phase-matching condition with a SPhP of 11.03 THz is satisfied with a stripe of 8.5 µm of width and 1703.47 nm of thickness. Solving equation 5.1 in these conditions give us a maximum efficiency of $7.5 \times 10^{-6}\,\mathrm{W}^{-1}$, figure 5.7, but with propagation lengths over 30 cm which is not technologically possible. Another con is that the phase-matching condition has no tolerance to changes in the thickness of the stripe and indeed ± 1 nm is enough to lose it but in short propagating distances, <1 mm, it makes no difference, giving efficiencies about $1 \times 10^{-9}\,\mathrm{W}^{-1}$.

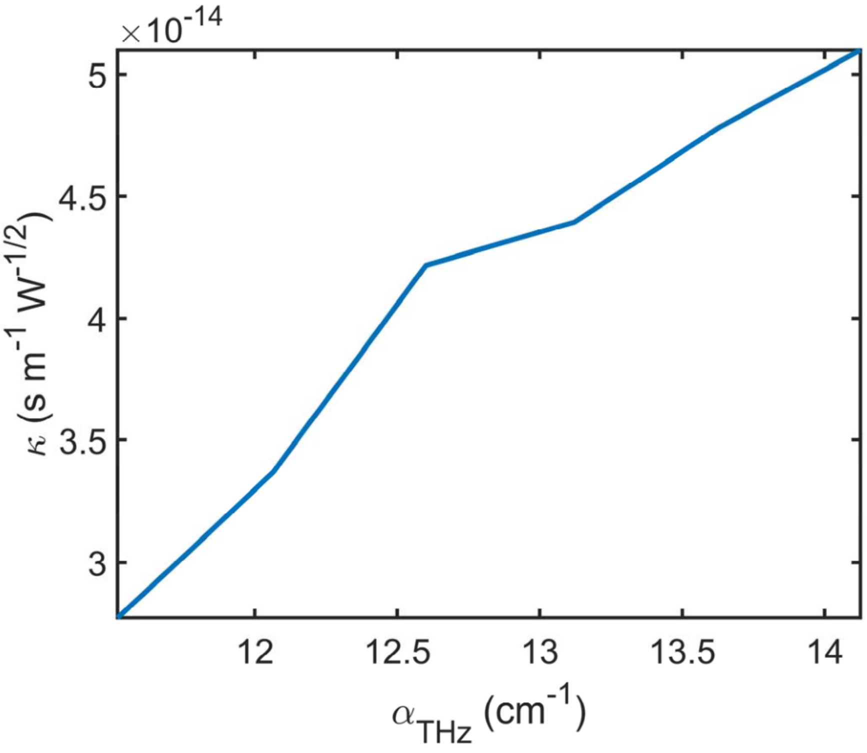

Figure 5.6: Relation of coupling coefficient κ with THz losses α_{THz} for a TE-TM mid-IR combination to generate a *ss* 11.03 THz mode. The geometrical parameter tuned to increase the losses is the thickness of the stripe.

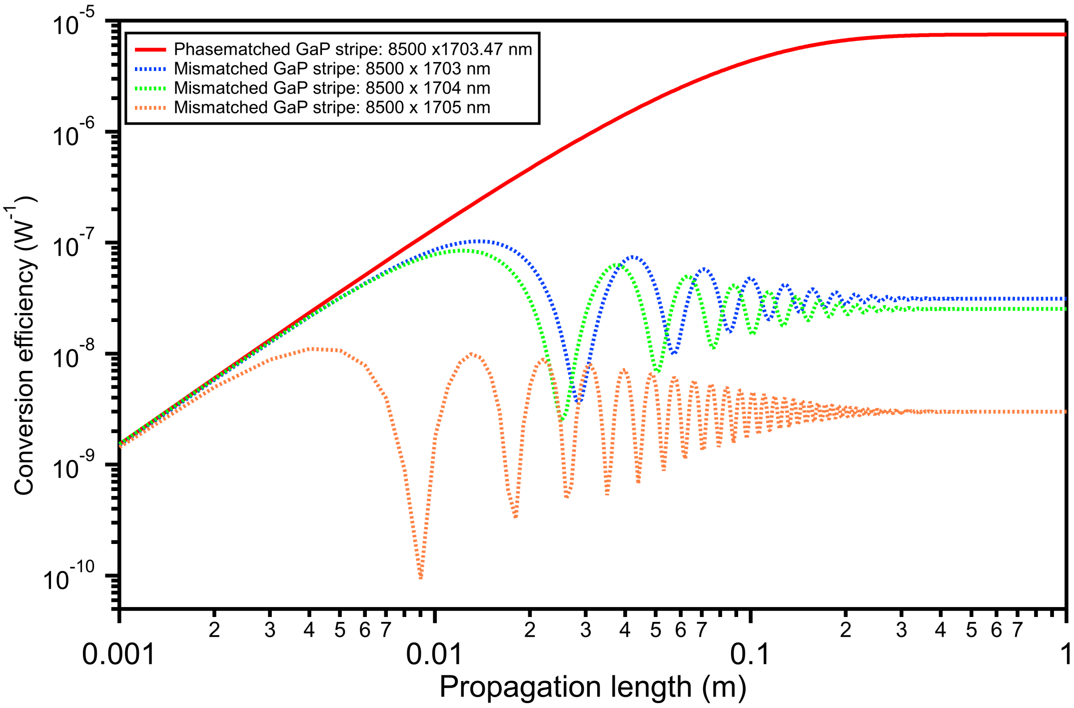

Figure 5.7: Conversion efficiency with the n-IR pump for the phase matched configuration (solid red line) and for small variations in the thickness (dashed lines).

The second proposal is the use of m-IR pump waves, with a TM mode of 4.9 µm and a TE mode of 6 µm. The larger wavelength compared to the n-IR case is going to make the IR modes less confined, increasing the overlap with the THz mode but reducing their propagation constant. To reduce the phase mismatch, we need to increase the cross-section of the stripe to 15 µm of width and 2.7 µm of thickness, complete phase-matching is not possible without increasing dramatically the losses of the SPhP mode. Preliminary results without phase-matching and optimization give a maximal efficiency of $1 \times 10^{-10}\,\mathrm{W}^{-1}$.

Conclusions

In this chapter we have proposed the use of DFG process for the generation of THz waves. Benefiting from the strong coupling of light with phonons that happens in the Reststrahlen band of GaP we demonstrated that we can efficiently produce THz waves around 11 THz. We analysed the choice of the right crystallographic orientation, concluding that the standard alignment along the [110] direction is not suitable for the generation of SPhPs. To successfully overlap the longitudinal components of the SPhPs and the nonlinear polarization we need to rotate the GaP by a 45° angle so that light propagates along the [100] direction.

We have shown a highly efficient configuration with n-IR pumps in a GaP encapsulated stripe in phase-matching conditions and a m-IR pumped configuration with good efficiency in phase mismatch condition. Future work concerns the reduction of losses of the SPhP modes to reduce the propagation length needed to achieve good efficiency and to study a promising configuration, using a slit waveguide to confine the THz modes and thus increase the overlap.

Conclusion

The objective of this thesis was the study of two different aspects of integrated devices for nonlinear photonics based on GaP. The second harmonic generation using GaP microdisks for wavelength conversion in the n-IR regime and the THz surface phonon polariton generation in GaP stripes.

The review of the state-of-the-art shows that integrated resonators are one of the key components of photonic integrated circuits. The demand of integrated wavelength convertors, between the telecom and the datacom regimes motivated the research of this type of devices. One of the weaknesses of the domain was the lack of a study that addresses the role of the coupling process in the nonlinear process. We have thus the objective of studying the impact of the propagation constant mismatch and overlap into the device efficiency.

Using coupled mode theory, 3D FDTD and FEM models, we proposed three technologically viable configurations for vertical evanescent coupling for wavelength conversion from 2 µm to 1 µm. We have demonstrated that propagation constant matching is not necessary for critical coupling and that this point is not the point of highest efficiency in the second harmonic generation process. We also found that specific values of propagation mismatch offer large regions of high efficiency. This result has two major consequences: first it enlarges the panel of materials available to design the access waveguides; second, these propagation constant mismatch conditions offer high tolerance versus fabrication flaws and misalignment issues.

We also investigated the origin of the natural phase-matching arising in second-order nonlinear circular resonators, such as the $\bar{4}$-QPM in zinc-blende microdisks. We used a transverse spin angular description of light to demonstrate that the origin of the additional quanta that appears in the azimuthal order selection rule of the nonlinear process results from the conversion of the Berry phase experienced by the TSAM components of the WGMs into azimuthal momentum. We generalized this effect and showed that every element of the second-order nonlinear susceptibility tensor is associated to a single QPM condition. With this result, we developed a tool to easily obtain the QPM condition for any nonlinear material.

As a first step towards fully encapsulated GaP nonlinear wavelength converter, based on the on the theoretical results of chapters 2 an 3 and previous works realized in the laboratory, we design an architecture based on small GaP microdisks where strict $\bar{4}$-QPM applies, vertically coupled to a silicon nitride waveguide. We investigated technological challenges of the process flow for the fabrication of these GaP-based PICs. Three technological locks have been addressed independently: the bonding of GaP membranes onto dielectric substrates, the development of e-beam lithography processes to build the PIC components and the encapsulation of these components for the realization of a 3D PIC. Two strategies have been defined for both bonding of GaP membranes and encapsulation of photonic layers. Molecular bonding using SiO_2 is the most promising one, resulting in flat and clean interfaces, further optimization of the membrane releasing process is being done to ensure the stable fixation of the GaP layer. For the encapsulation process, both alternatives give good results but the expertise gained in the surface treatment of SiO_2 for the bonding process, makes the surfaces obtained of excellent quality. The short-term goal is the fabrication of a fully encapsulated GaP microdisks coupled to Si_3N_4 waveguides to demonstrate the high efficiency in the SHG in strict $\bar{4}$-QPM conditions.

In parallel, we have explored the potential of the GaP nonlinear platform for the THz generation in the Reststrahlen band through difference frequency generation in GaP stripes. In this wavelength range, the propagation of THz waves in the form on surface phonon polaritons leads to unexpected designs of nonlinear waveguides. We demonstrated that the optimal orientation of the waveguide is in this case the [100] direction. The designed GaP encapsulated stripes show promising THz generation efficiencies, up to $7.5 \times 10^{-6}\,\mathrm{W}^{-1}$, for different wavelengths of the input fields, specially in the n-IR range where phase-matching has been obtained.

Further optimization can be achieved by reducing the losses of the SPhP modes or increasing the overlap without loss increase. The objective of these two processes is to reduce the propagation length needed to achieve a significant efficiency. Also the study of a slit waveguide is promising since we would have a third parameter to adjust the phase-matching. Furthermore, first estimations show overlaps two times higher than for the stripe case but also much higher losses due to the increased part of the longitudinal electric field component inside the GaP

The realization of an integrated THz source, in the Reststrahlen band would be the first step towards a complete on-chip sensing device in this regime, areas like spectroscopy for cancer or protein identification are already using THz sensing in parts of the spectrum that correspond to rotations and vibrations of molecules, like the Reststrahlen band of III-V, that serve as fingerprint. Also imaging research has made use of these frequencies to obtain far-IR images avoiding the water interference.

All the results converge in the demonstration of gallium phosphide as one of the best candidates for nonlinear PIC components. The versatility of different processes, together with an existing experimental procedure to build the devices shows the potential of this material. The ability to efficiently couple to second-order nonlinear GaP resonators and to create a two level PIC with Si_3N_4 can be the base to design two vertically coupled microresonators where one acts as the nonlinear material and the other allows to tune spectrally the output of the device. This configuration can be even combined with materials susceptible to electromagnetic induced transparency to further control the process. This kind of integrated nonlinear sources are expected to revolutionise quantum communication and computation since using cascaded $\chi^{(2)}$ processes, like second harmonic generation followed by a spontaneous parametric down conversion process, are a demonstrated source of entangled photon-pairs. Also this kind of coupled integrated resonators can be designed with materials featuring third order nonlinearities to feature bistability and temporal effects.

Bibliography

[1] T. H. Maiman, “Stimulated optical radiation in ruby,” *Nature*, vol. 187, no. 4736, pp. 493–494, 1960.

[2] Z. I. Alferov, “AlAs-GaAs heterojunction injection lasers with a low room-temperature threshold,” *Sov. Phys. Semicond.*, vol. 3, pp. 1107–1110, 1970.

[3] K. C. Kao and G. A. Hockham, “Dielectric-fibre surface waveguides for optical frequencies,” in *Proceedings of the Institution of Electrical Engineers*, vol. 113, pp. 1151–1158, IET, 1966.

[4] P. Nozières and P. Baruch, “Pierre Aigrain,” *Physics Today*, vol. 56, pp. 76–77, Sept. 2003.

[5] R. Soref and J. Lorenzo, “Single-crystal silicon: a new material for 1.3 and 1.6 μm integrated-optical components,” *Electronics Letters*, vol. 21, no. 21, pp. 953–954, 1985.

[6] D. Albares and R. Soref, “Silicon-on-sapphire waveguides,” in *Integrated Optical Circuit Engineering IV*, vol. 704, pp. 24–25, International Society for Optics and Photonics, 1987.

[7] R. Soref, F. Namavar, and J. Lorenzo, “Optical waveguiding in a single-crystal layer of germanium silicon grown on silicon,” *Optics Letters*, vol. 15, no. 5, pp. 270–272, 1990.

[8] G. Abstreiter, “Engineering the future of electronics,” *Physics World*, vol. 5, pp. 36–40, mar 1992.

[9] R. A. Soref, “Silicon-based optoelectronics,” *Proceedings of the IEEE*, vol. 81, no. 12, pp. 1687–1706, 1993.

[10] R. J. Mears, L. Reekie, I. Jauncey, and D. N. Payne, “Low-noise erbium-doped fibre amplifier operating at 1.54 μm,” *Electronics Letters*, vol. 23, no. 19, pp. 1026–1028, 1987.

[11] J. Faist, F. Capasso, D. L. Sivco, C. Sirtori, A. L. Hutchinson, and A. Y. Cho, “Quantum cascade laser,” *Science*, vol. 264, no. 5158, pp. 553–556, 1994.

[12] A. Krishnamoorthy, L. Chirovsky, W. Hobson, R. Leibengath, S. Hui, G. Zydzik, K. Goossen, J. Wynn, B. Tseng, J. Lopata, J. Walker, J. Cunningham, and L. D’Asaro, “Vertical-cavity surface-emitting lasers flip-chip bonded to gigabit-per-second CMOS circuits,” *IEEE Photonics Technology Letters*, vol. 11, pp. 128–130, Jan. 1999.

[13] J. W. Silverstone, R. Santagati, D. Bonneau, M. J. Strain, M. Sorel, J. L. O’Brien, and M. G. Thompson, “Qubit entanglement between ring-resonator photon-pair sources on a silicon chip,” *Nature communications*, vol. 6, no. 1, pp. 1–7, 2015.

[14] X. Ma, C.-H. F. Fung, and H.-K. Lo, “Quantum key distribution with entangled photon sources,” *Physical Review A*, vol. 76, no. 1, p. 012307, 2007.

[15] D. Bouwmeester, J.-W. Pan, K. Mattle, M. Eibl, H. Weinfurter, and A. Zeilinger, “Experimental quantum teleportation,” *Nature*, vol. 390, no. 6660, pp. 575–579, 1997.

[16] M. Fink, F. Steinlechner, J. Handsteiner, J. P. Dowling, T. Scheidl, and R. Ursin, “Entanglement-enhanced optical gyroscope,” *New Journal of Physics*, vol. 21, no. 5, p. 053010, 2019.

[17] X. Guo, C.-L. Zou, and H. X. Tang, “Second-harmonic generation in aluminum nitride microrings with 2500%/W conversion efficiency,” *Optica*, vol. 3, pp. 1126–1131, Oct. 2016.

[18] P. S. Kuo and G. S. Solomon, “On- and off-resonance second-harmonic generation in GaAs microdisks,” *Optics Express*, vol. 19, pp. 16898–16918, Aug. 2011.

[19] P. S. Kuo, W. Fang, and G. S. Solomon, “$\bar{4}$-quasi-phase-matched interactions in GaAs microdisk cavities,” *Optics Letters*, vol. 34, pp. 3580–3582, Nov. 2009.

[20] P. S. Kuo, J. Bravo-Abad, and G. S. Solomon, “Second-harmonic generation using quasi-phasematching in a GaAs whispering-gallery-mode microcavity,” *Nature Communications*, vol. 5, pp. 1–7, Jan. 2014.

[21] R. Soref, “The Past, Present, and Future of Silicon Photonics,” *IEEE Journal of Selected Topics in Quantum Electronics*, vol. 12, pp. 1678–1687, Nov. 2006.

[22] K.-W. Lee, A. Noriki, K. Kiyoyama, T. Fukushima, T. Tanaka, and M. Koyanagi, “Three-Dimensional Hybrid Integration Technology of CMOS, MEMS, and Photonics Circuits for Optoelectronic Heterogeneous Integrated Systems,” *IEEE Transactions on Electron Devices*, vol. 58, pp. 748–757, Mar. 2011.

[23] M. Poot and H. X. Tang, “Characterization of optical quantum circuits using resonant phase shifts,” *Applied Physics Letters*, vol. 109, p. 131106, Sept. 2016.

[24] L. Sansoni, F. Sciarrino, G. Vallone, P. Mataloni, A. Crespi, R. Ramponi, and R. Osellame, “Two-Particle Bosonic-Fermionic Quantum Walk via Integrated Photonics,” *Physical Review Letters*, vol. 108, p. 010502, Jan. 2012.

[25] C. Koos, P. Vorreau, T. Vallaitis, P. Dumon, W. Bogaerts, R. Baets, B. Esembeson, I. Biaggio, T. Michinobu, F. Diederich, W. Freude, and J. Leuthold, “All-optical high-speed signal processing with silicon–organic hybrid slot waveguides,” *Nature Photonics*, vol. 3, pp. 216–219, Apr. 2009.

[26] T. Baehr-Jones, M. Hochberg, G. Wang, R. Lawson, Y. Liao, P. A. Sullivan, L. Dalton, A. K.-Y. Jen, and A. Scherer, “Optical modulation and detection in slotted Silicon waveguides,” *Optics Express*, vol. 13, pp. 5216–5226, July 2005.

[27] J. S. Levy, A. Gondarenko, M. A. Foster, A. C. Turner-Foster, A. L. Gaeta, and M. Lipson, “CMOS-compatible multiple-wavelength oscillator for on-chip optical interconnects,” *Nature Photonics*, vol. 4, pp. 37–40, Jan. 2010.

[28] L. Chang, Y. Li, N. Volet, L. Wang, J. Peters, and J. E. Bowers, “Thin film wavelength converters for photonic integrated circuits,” *Optica*, vol. 3, pp. 531–535, May 2016.

[29] G. I. Stegeman, A. Villeneuve, J. S. Aitchison, and C. N. Ironside, "Nonlinear Integrated Optics and All-Optical Waveguide Switching in Semiconductors," in *Fabrication, Properties and Applications of Low-Dimensional Semiconductors* (M. Balkanski and I. Yanchev, eds.), NATO ASI Series, pp. 415–449, Dordrecht: Springer Netherlands, 1995.

[30] M. Poot, C. Schuck, X.-s. Ma, X. Guo, and H. X. Tang, "Design and characterization of integrated components for SiN photonic quantum circuits," *Optics Express*, vol. 24, pp. 6843–6860, Apr. 2016.

[31] M. Lamponi, S. Keyvaninia, F. Pommereau, R. Brenot, G. de Valicourt, F. Lelarge, G. Roelkens, D. Van Thourhout, S. Messaoudene, J. . Fedeli, and G. . Duan, "Heterogeneously integrated inp/soi laser using double tapered single-mode waveguides through adhesive die to wafer bonding," in *7th IEEE International Conference on Group IV Photonics*, pp. 22–24, 2010.

[32] J. V. Campenhout, P. Rojo-Romeo, P. Regreny, C. Seassal, D. V. Thourhout, S. Verstuyft, L. D. Cioccio, J.-M. Fedeli, C. Lagahe, and R. Baets, "Electrically pumped InP-based microdisk lasers integrated with a nanophotonic silicon-on-insulator waveguide circuit," *Optics Express*, vol. 15, pp. 6744–6749, May 2007.

[33] G. Roelkens, J. Van Campenhout, J. Brouckaert, D. Van Thourhout, R. Baets, P. R. Romeo, P. Regreny, A. Kazmierczak, C. Seassal, X. Letartre, G. Hollinger, J. M. Fedeli, L. Di Cioccio, and C. Lagahe-Blanchard, "III-V/Si photonics by die-to-wafer bonding," *Materials Today*, vol. 10, pp. 36–43, July 2007.

[34] S. M. Hendrickson, A. C. Foster, R. M. Camacho, and B. D. Clader, "Integrated nonlinear photonics: emerging applications and ongoing challenges [Invited]," *JOSA B*, vol. 31, pp. 3193–3203, Dec. 2014.

[35] J. Leuthold, C. Koos, and W. Freude, "Nonlinear silicon photonics," *Nature Photonics*, vol. 4, pp. 535–544, Aug. 2010.

[36] M. Liao, S. Chen, J.-S. Park, A. Seeds, and H. Liu, "III–V quantum-dot lasers monolithically grown on silicon," *Semiconductor Science and Technology*, vol. 33, p. 123002, Oct. 2018.

[37] I. Lucci, S. Charbonnier, L. Pedesseau, M. Vallet, L. Cerutti, J.-B. Rodriguez, E. Tournié, R. Bernard, A. Létoublon, N. Bertru, A. Le Corre, S. Rennesson, F. Semond, G. Patriarche, L. Largeau, P. Turban, A. Ponchet, and C. Cornet, "Universal description of III-V/Si epitaxial growth processes," *Physical Review Materials*, vol. 2, p. 060401, June 2018.

[38] E. A. Beam, S. Mahajan, and W. A. Bonner, "Dislocation replication and annihilation in InP homoepitaxial layers grown by liquid phase epitaxy," *Materials Science and Engineering: B*, vol. 7, pp. 83–101, Sept. 1990.

[39] L. C. Chuang, F. G. Sedgwick, R. Chen, W. S. Ko, M. Moewe, K. W. Ng, T.-T. D. Tran, and C. Chang-Hasnain, "GaAs-Based Nanoneedle Light Emitting Diode and Avalanche Photodiode Monolithically Integrated on a Silicon Substrate," *Nano Letters*, vol. 11, pp. 385–390, Feb. 2011.

[40] D. Liang, G. Roelkens, R. Baets, and J. E. Bowers, "Hybrid Integrated Platforms for Silicon Photonics," *Materials*, vol. 3, pp. 1782–1802, Mar. 2010.

[41] N. Thomas, R. J. Barbour, Y. Song, M. L. Lee, and K.-M. C. Fu, "Waveguide-integrated single-crystalline GaP resonators on diamond," *Optics Express*, vol. 22, pp. 13555–13564, June 2014.

[42] C. Baker, S. Stapfner, D. Parrain, S. Ducci, G. Leo, E. M. Weig, and I. Favero, "Optical instability and self-pulsing in silicon nitride whispering gallery resonators," *Optics Express*, vol. 20, pp. 29076–29089, Dec. 2012.

[43] J. D. Caldwell, L. Lindsay, V. Giannini, I. Vurgaftman, T. L. Reinecke, S. A. Maier, and O. J. Glembocki, "Low-loss, infrared and terahertz nanophotonics using surface phonon polaritons," *Nanophotonics*, vol. -1, Apr. 2015.

[44] M. Gould, S. Chakravarthi, I. R. Christen, N. Thomas, S. Dadgostar, Y. Song, M. L. Lee, F. Hatami, and K.-M. C. Fu, "Large-scale GaP-on-diamond integrated photonics platform for NV center-based quantum information," *JOSA B*, vol. 33, pp. B35–B42, Mar. 2016.

[45] E. F. Schubert, *Light-Emitting Diodes (Second Edition, 2006).* E. Fred Schubert, Jan. 2006.

[46] D. J. Wilson, K. Schneider, S. Hönl, M. Anderson, Y. Baumgartner, L. Czornomaz, T. J. Kippenberg, and P. Seidler, "Integrated gallium phosphide nonlinear photonics," *Nature Photonics*, vol. 14, pp. 57–62, Jan. 2020.

[47] Y. Dumeige and P. Féron, "Whispering-gallery-mode analysis of phase-matched doubly resonant second-harmonic generation," *Physical Review A*, vol. 74, p. 063804, Dec. 2006.

[48] J. E. Goell, “A Circular-Harmonic Computer Analysis of Rectangular Dielectric Waveguides,” *Bell System Technical Journal*, vol. 48, no. 7, pp. 2133–2160, 1969.

[49] N. Poulvellarie, U. Dave, K. Alexander, C. Ciret, M. Billet, C. M. Arabi, F. Raineri, S. Combrie, A. De Rossi, G. Roelkens, S.-P. Gorza, B. Kuyken, and F. Leo, “Second Harmonic Generation Enabled by Longitudinal Electric Field Components in Photonic Wire Waveguides,” *arXiv:2001.01709 [physics]*, Jan. 2020.

[50] O. M. Lord Rayleigh, “IX. Further applications of Bessel’s functions of high order to the Whispering Gallery and allied problems,” *The London, Edinburgh, and Dublin Philosophical Magazine and Journal of Science*, vol. 27, Jan. 1914.

[51] J. Heebner, R. Grover, T. Ibrahim, and T. A. Ibrahim, *Optical Microresonators: Theory, Fabrication, and Applications.* Springer Science & Business Media, 2008.

[52] P. Guillemé, *Second harmonic generation in gallium phosphide microdisks integrated on Silicon.* Theses, Université Bretagne Loire, Dec. 2016.

[53] Z.-F. Bi, A. W. Rodriguez, H. Hashemi, D. Duchesne, M. Loncar, K.-M. Wang, and S. G. Johnson, “High-efficiency second-harmonic generation in doubly-resonant $\chi^{(2)}$ microring resonators,” *Optics Express*, vol. 20, p. 7526, Mar. 2012.

[54] J.-Y. Bengloan, A. De Rossi, V. Ortiz, X. Marcadet, M. Calligaro, I. Maurin, and C. Sirtori, “Intracavity sum-frequency generation in GaAs quantum cascade lasers,” *Applied Physics Letters*, vol. 84, pp. 2019–2021, Mar. 2004.

[55] K. Miyamoto, S. Ohno, M. Fujiwara, H. Minamide, H. Hashimoto, and H. Ito, "Optimized terahertz-wave generation using BNA-DFG," *Optics Express*, vol. 17, pp. 14832–14838, Aug. 2009.

[56] A. Rice, Y. Jin, X. F. Ma, X. Zhang, D. Bliss, J. Larkin, and M. Alexander, "Terahertz optical rectification from [110] zinc-blende crystals," *Applied Physics Letters*, vol. 64, pp. 1324–1326, Mar. 1994.

[57] P. A. Franken, A. E. Hill, C. W. Peters, and G. Weinreich, "Generation of Optical Harmonics," *Physical Review Letters*, vol. 7, pp. 118–119, Aug. 1961.

[58] M. De Regis, S. Bartalini, M. Ravaro, D. Calonico, P. De Natale, and L. Consolino, "Room-Temperature Continuous-Wave Frequency-Referenced Spectrometer up to 7.5 THz," *Physical Review Applied*, vol. 10, p. 064041, Dec. 2018.

[59] K. Ohtani, D. Turčinková, C. Bonzon, I.-C. Benea-Chelmus, M. Beck, J. Faist, M. Justen, U. U. Graf, M. Mertens, and J. Stutzki, "High performance 4.7 THz GaAs quantum cascade lasers based on four quantum wells," *New Journal of Physics*, vol. 18, p. 123004, Dec. 2016.

[60] M. A. Belkin, F. Capasso, F. Xie, A. Belyanin, M. Fischer, A. Wittmann, and J. Faist, "Room temperature terahertz quantum cascade laser source based on intracavity difference-frequency generation," *Applied Physics Letters*, vol. 92, p. 201101, May 2008.

[61] G. Insero, C. Clivati, D. D'Ambrosio, P. D. Natale, G. Santambrogio, P. G. Schunemann, J.-J. Zondy, and S. Borri, "Difference frequency generation in

the mid-infrared with orientation-patterned gallium phosphide crystals," *Optics Letters*, vol. 41, pp. 5114–5117, Nov. 2016.

[62] P. Guillemé, Y. Dumeige, J. Stodolna, M. Vallet, T. Rohel, A. Létoublon, C. Cornet, A. Ponchet, O. Durand, and Y. Léger, "Second harmonic generation in gallium phosphide microdisks on silicon: from strict $\bar{4}$ to random quasi-phase matching," *Semiconductor Science and Technology*, vol. 32, p. 065004, May 2017.

[63] K. Saito, T. Tanabe, and Y. Oyama, "Design of a GaP/Si composite waveguide for CW terahertz wave generation via difference frequency mixing," *Applied Optics*, vol. 53, pp. 3587–3592, June 2014.

[64] J. U. Fürst, D. V. Strekalov, D. Elser, M. Lassen, U. L. Andersen, C. Marquardt, and G. Leuchs, "Naturally Phase-Matched Second-Harmonic Generation in a Whispering-Gallery-Mode Resonator," *Physical Review Letters*, vol. 104, p. 153901, Apr. 2010.

[65] G. Lin, J. U. Fürst, D. V. Strekalov, and N. Yu, "Broadband second harmonic generation in whispering gallery mode resonators," *arXiv:1303.3814 [physics]*, Mar. 2013.

[66] G. Lin, J. U. Fürst, D. V. Strekalov, and N. Yu, "Wide-range cyclic phase matching and second harmonic generation in whispering gallery resonators," *Applied Physics Letters*, vol. 103, p. 181107, Oct. 2013.

[67] J. Lin, N. Yao, Z. Hao, J. Zhang, W. Mao, M. Wang, W. Chu, R. Wu, Z. Fang, L. Qiao, W. Fang, F. Bo, and Y. Cheng, "Broadband Quasi-Phase-Matched

Harmonic Generation in an On-Chip Monocrystalline Lithium Niobate Microdisk Resonator," *Physical Review Letters*, vol. 122, p. 173903, May 2019.

[68] J. Li, R. Yu, Y. Qu, C. Ding, D. Zhang, and Y. Wu, "Second-harmonic generation with ultralow-power pump thresholds in a dimer of two active-passive cavities," *Physical Review A*, vol. 96, p. 013815, July 2017.

[69] S. Mariani, A. Andronico, A. Lemaître, I. Favero, S. Ducci, and G. Leo, "Second-harmonic generation in AlGaAs microdisks in the telecom range," *Optics Letters*, vol. 39, pp. 3062–3065, May 2014.

[70] I. Roland, M. Gromovyi, Y. Zeng, M. El Kurdi, S. Sauvage, C. Brimont, T. Guillet, B. Gayral, F. Semond, J. Y. Duboz, M. de Micheli, X. Checoury, and P. Boucaud, "Phase-matched second harmonic generation with on-chip GaN-on-Si microdisks," *Scientific Reports*, vol. 6, pp. 1–8, Sept. 2016.

[71] K. Schneider, P. Welter, Y. Baumgartner, H. Hahn, L. Czornomaz, and P. Seidler, "Gallium Phosphide-on-Silicon Dioxide Photonic Devices," *Journal of Lightwave Technology*, vol. 36, pp. 2994–3002, July 2018.

[72] D. P. Lake, M. Mitchell, H. Jayakumar, L. F. dos Santos, D. Curic, and P. E. Barclay, "Efficient telecom to visible wavelength conversion in doubly resonant gallium phosphide microdisks," *Applied Physics Letters*, vol. 108, p. 031109, Jan. 2016.

[73] A. D. Logan, M. Gould, E. R. Schmidgall, K. Hestroffer, Z. Lin, W. Jin, A. Majumdar, F. Hatami, A. W. Rodriguez, and K.-M. C. Fu, "400%/W second harmonic conversion efficiency in 14μm-diameter gallium phosphide-on-oxide resonators," *Optics Express*, vol. 26, pp. 33687–33699, Dec. 2018.

[74] L. Li, L. Chen, J. Zhu, J. Freeman, P. Dean, A. Valavanis, A. Davies, and E. Linfield, "Terahertz quantum cascade lasers with >1 W output powers," *Electronics Letters*, vol. 50, pp. 309–311, Feb. 2014.

[75] F. Barho, H. Philip, Z. Loghmari, M. Bahriz, A. N. Baranov, and R. Teissier, "Long wavelength ($\lambda = 10$ - 18 μm) mid-ir quantum cascade lasers operating in a continuous wave at room temperature," in *2019 44th International Conference on Infrared, Millimeter, and Terahertz Waves (IRMMW-THz)*, pp. 1–1, Sept. 2019.

[76] M. S. Vitiello, G. Scalari, B. Williams, and P. D. Natale, "Quantum cascade lasers: 20 years of challenges," *Optics Express*, vol. 23, pp. 5167–5182, Feb. 2015.

[77] K. L. Vodopyanov and Y. H. Avetisyan, "Optical terahertz wave generation in a planar GaAs waveguide," *Optics Letters*, vol. 33, pp. 2314–2316, Oct. 2008.

[78] K. L. Vodopyanov, J. E. Schaar, P. S. Kuo, M. M. Fejer, X. Yu, J. S. Harris, V. G. Kozlov, D. F. Bliss, and C. Lynch, "Terahertz wave generation in orientation-patterned GaAs using resonantly enhanced schemes," in *Nonlinear Frequency Generation and Conversion: Materials, Devices, and Applications VI*, vol. 6455, p. 645509, International Society for Optics and Photonics, Feb. 2007.

[79] Z. Ruan, G. Veronis, K. L. Vodopyanov, M. M. Fejer, and S. Fan, "Enhancement of optics-to-THz conversion efficiency by metallic slot waveguides," *Optics Express*, vol. 17, pp. 13502–13515, Aug. 2009.

[80] K. Saito, T. Tanabe, and Y. Oyama, “Elliptically polarized THz-wave generation from GaP-THz planar waveguide via collinear phase-matched difference frequency mixing,” *Optics Express*, vol. 20, pp. 26082–26088, Nov. 2012.

[81] T. Tanabe, K. Suto, J. Nishizawa, T. Kimura, and K. Saito, “Frequency-tunable high-power terahertz wave generation from GaP,” *Journal of Applied Physics*, vol. 93, pp. 4610–4615, Mar. 2003.

[82] S. Keyvaninia, S. Verstuyft, L. V. Landschoot, F. Lelarge, G.-H. Duan, S. Messaoudene, J. M. Fedeli, T. D. Vries, B. Smalbrugge, E. J. Geluk, J. Bolk, M. Smit, G. Morthier, D. V. Thourhout, and G. Roelkens, “Heterogeneously integrated iii-v/silicon distributed feedback lasers,” *Opt. Lett.*, vol. 38, pp. 5434–5437, Dec 2013.

[83] K. Okamoto, *Fundamentals of optical waveguides.* Academic press, 2006.

[84] C. Arlotti, O. Gauthier-Lafaye, A. Monmayrant, and S. Calvez, “Achromatic critically coupled racetrack resonators,” *JOSA B*, vol. 34, pp. 2343–2351, Nov. 2017.

[85] A. Lorenzo-Ruiz, C. Cornet, A. Beck, and Y. Léger, “Dual wavelength evanescent coupler for nonlinear gap-based microdisk resonators,” *OSA Continuum*, vol. 3, pp. 43–49, Jan 2020.

[86] T. J. A. Kippenberg, *Nonlinear optics in ultra-high-Q whispering-gallery optical microcavities.* PhD thesis, California Institute of Technology, 2004.

[87] J. Fürst, B. Sturman, K. Buse, and I. Breunig, "Whispering gallery resonators with broken axial symmetry: Theory and experiment," *Optics express*, vol. 24, no. 18, pp. 20143–20155, 2016.

[88] J. Lu, J. B. Surya, X. Liu, A. W. Bruch, Z. Gong, Y. Xu, and H. X. Tang, "Periodically poled thin-film lithium niobate microring resonators with a second-harmonic generation efficiency of 250,000%/w," *Optica*, vol. 6, no. 12, pp. 1455–1460, 2019.

[89] R. Wolf, Y. Jia, S. Bonaus, C. S. Werner, S. J. Herr, I. Breunig, K. Buse, and H. Zappe, "Quasi-phase-matched nonlinear optical frequency conversion in on-chip whispering galleries," *Optica*, vol. 5, no. 7, pp. 872–875, 2018.

[90] C. Ciret, K. Alexander, N. Poulvellarie, M. Billet, C. M. Arabi, B. Kuyken, S.-P. Gorza, and F. Leo, "Full vectorial modeling of second harmonic generation in iii-v-on-insulator nanowires," *arXiv preprint arXiv:2001.02210*, 2020.

[91] R. Y. Chiao and Y.-S. Wu, "Manifestations of berry's topological phase for the photon," *Physical Review Letters*, vol. 57, no. 8, p. 933, 1986.

[92] A. Tomita and R. Y. Chiao, "Observation of berry's topological phase by use of an optical fiber," *Physical Review Letters*, vol. 57, no. 8, p. 937, 1986.

[93] L. S. Trainor, F. Sedlmeir, C. Peuntinger, and H. G. Schwefel, "Selective coupling enhances harmonic generation of whispering-gallery modes," *Physical Review Applied*, vol. 9, no. 2, p. 024007, 2018.

[94] C. Cornet, S. Charbonnier, I. Lucci, L. Chen, A. Létoublon, A. Alvarez, K. Tavernier, T. Rohel, R. Bernard, J.-B. Rodriguez, L. Cerutti, E. Tournié, Y. Léger,

M. Bahri, G. Patriarche, L. Largeau, A. Ponchet, P. Turban, and N. Bertru, “Zinc-blende group iii-v/group iv epitaxy: Importance of the miscut,” *Phys. Rev. Materials*, vol. 4, p. 053401, May 2020.

[95] H. Nakanishi, T. Nishimoto, R. Nakamura, A. Yotsumoto, T. Yoshida, and S. Shoji, “Studies on sio2–sio2 bonding with hydrofluoric acid. room temperature and low stress bonding technique for mems,” *Sensors and Actuators A: Physical*, vol. 79, no. 3, pp. 237 – 244, 2000.

[96] X. Luo, Y. Cao, J. Song, X. Hu, Y. Cheng, C. Li, C. Liu, T.-Y. Liow, M. Yu, H. Wang, *et al.*, “High-throughput multiple dies-to-wafer bonding technology and iii/v-on-si hybrid lasers for heterogeneous integration of optoelectronic integrated circuits,” *Frontiers in Materials*, vol. 2, p. 28, 2015.

[97] R. Saleem-Urothodi, J. L. Pouliquen, T. Rohel, R. Bernard, C. Pareige, A. Lorenzo-Ruiz, A. Beck, A. Létoublon, O. D. Sagazan, C. Cornet, Y. Dumeige, and Y. Léger, “Loss assessment in random crystal polarity gallium phosphide microdisks grown on silicon,” *Opt. Lett.*, vol. 45, pp. 4646–4649, Aug 2020.

[98] R. Bogue, “Sensing with terahertz radiation: a review of recent progress,” *Sensor Review*, 2018.

[99] W. Faust and C. H. Henry, “Mixing of visible and near-resonance infrared light in gap,” *Physical Review Letters*, vol. 17, no. 25, p. 1265, 1966.

[100] Y. J. Ding, “Efficient generation of high-frequency terahertz waves from highly lossy second-order nonlinear medium at polariton resonance under transverse-pumping geometry,” *Optics Letters*, vol. 35, no. 2, pp. 262–264, 2010.

[101] P. Berini, “Plasmon-polariton waves guided by thin lossy metal films of finite width: Bound modes of symmetric structures,” *Physical Review B*, vol. 61, no. 15, p. 10484, 2000.

[102] A. Yariv, “Universal relations for coupling of optical power between microresonators and dielectric waveguides,” *Electronics Letters*, vol. 36, no. 4, pp. 321–322, 2000.

List of Figures

List of Tables

Appendix A

Expressions of the Transmitted and Circulating Power in a Coupled Microresonator

Following [102] and [52], we can describe the phenomena of coupling between a waveguide and a microresonator using coupled mode theory (CMT).

To summarize the effect of a coupler, a scattering matrix can be obtained integrating equations 2.8 along the interaction length. With $A_{0/1}$ and $B_{0/1}$ as the input/output field envelopes in waveguide 1 and 2 respectively, the scattering matrix is defined as:

$$\begin{pmatrix} A_1 \\ B_1 \end{pmatrix} = \begin{pmatrix} t & -ir \\ -ir^* & t^* \end{pmatrix} \begin{pmatrix} A_0 \\ B_0 \end{pmatrix} \tag{A.1}$$

where t and r are the complex transmission and coupling coefficients of the coupler respectively (figure A.1). When considering a lossless coupling, r and t satisfy the relationship $|r|^2 + |t|^2 = 1$. Internal losses are modeled by the *inner circulation*

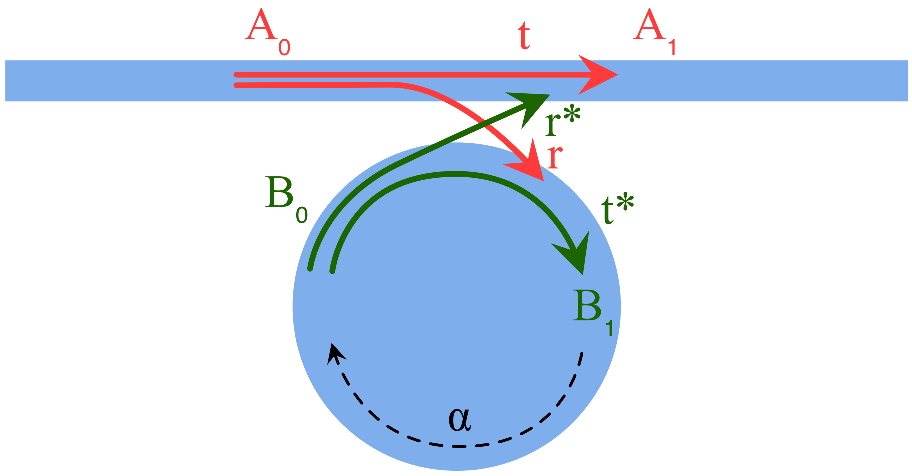

Figure A.1: Scheme showing the notation used to describe the coupling through CMT. t is the transmission coefficient. r is the coupling coefficient between the waveguide and the resonator. α represents the internal losses each round-trip. A and B are the amplitudes of the fields in the waveguide and the microdisk respectively.

factor α. Then, after one round trip, one can relate B_0 to B_1 writing explicitly the accumulated phase shift:

$$B_0 = B_1 \alpha e^{i\varphi} \tag{A.2}$$

φ being the phase difference in one round-trip. From A.1 and A.2 we can thus write:

$$B_1(1 - t^* \alpha e^{i\varphi}) = -r^* A_0 \tag{A.3}$$

$$B_0(t^* - \frac{e^{-i\varphi}}{\alpha}) = r^* A_0 \tag{A.4}$$

Now if we want to find the expression for the transmitted power, $|A_1|^2$, we put A.4

into A.1 to obtain:

$$A_1 = tA_0 - r\frac{\alpha r^* A_0}{-\alpha t^* + e^{-i\varphi}} = \frac{-\alpha + te^{-i\varphi}}{-\alpha t^* + e^{-i\varphi}}A_0 \tag{A.5}$$

And considering that the coupling process does not introduce a phase shift, we finally get:

$$|A_1|^2 = \frac{\alpha^2 - 2\alpha tcos(\varphi) + t^2}{1 - 2\alpha tcos(\varphi) + \alpha^2 t^2}|A_0|^2 \tag{A.6}$$

If we do the same for the circulating power inside the microresonator, $|B_0|^2$, introducing equation A.3 into A.2 we obtain:

$$|B_0|^2 = \frac{\alpha^2(1 - t^2)}{1 - 2\alpha tcos(\varphi) + \alpha^2 t^2}|A_0|^2 \tag{A.7}$$

Appendix B

Complete Representation of the Nonlinear Tensor in Circular Basis

As explained in chapter 2, to write the second-order nonlinear susceptibility tensor in the circular basis we have:

$$\chi^{(2)}_{CP} = \mathbf{Q} \cdot \chi^{(2)}_{x,y,z} \cdot (\mathbf{Q}^{-1} \otimes I_3)(I_3 \otimes \mathbf{Q}^{-1}) \tag{B.1}$$

being $\mathbf{Q}$ the transfer matrix from Cartesian to CP basis and I_3 the identity matrix of dimension 3. The nonlinear susceptibility tensor, in cartesian basis, usually reads as:

$$\chi^{(2)}_{xyz} = \begin{bmatrix} d_{11} & d_{16} & d_{15} & d_{16} & d_{12} & d_{14} & d_{15} & d_{14} & d_{13} \\ d_{16} & d_{12} & d_{14} & d_{12} & d_{22} & d_{24} & d_{14} & d_{24} & d_{23} \\ d_{15} & d_{14} & d_{13} & d_{14} & d_{24} & d_{23} & d_{13} & d_{23} & d_{33} \end{bmatrix} \tag{B.2}$$

and thus applying B.1 we obtain:

$$\begin{bmatrix} a & a^* & b+d_{24} & a^* & f & b-id_{14} & b+d_{24} & b-id_{14} & c^* \\ f^* & a & b+id_{14} & a & a^* & b+d_{24} & b+id_{14} & b+d_{24} & c \\ b+id_{14} & b+d_{24} & c & b+d_{24} & b-id_{14} & c^* & c & c^* & d_{33} \end{bmatrix} \tag{B.3}$$

where:

$$a = \frac{\sqrt{2}}{4}(d_{11} + d_{12} + id_{16} + id_{22}) \tag{B.4}$$

$$b = \frac{d_{15} - d_{24}}{2} \tag{B.5}$$

$$c = \frac{\sqrt{2}}{2}(d_{13} + id_{23}) \tag{B.6}$$

$$f = \frac{\sqrt{2}}{4}(d_{11} - 3d_{12} - 3id_{16} + id_{22}) \tag{B.7}$$

With the Kleinman symmetry present in the Cartesian basis, conserved during this basis change, we can reduce and simplify the expression of the tensor that results in the reduced form presented in 3.13:

$$\chi^{(2)}_{CP} = \begin{bmatrix} a & f & c^* & b-id_{14} & b+d_{24} & a^* \\ f^* & a^* & c & b+d_{24} & b+id_{14} & a \\ b+id_{14} & b-id_{14} & d_{33} & c^* & c & b+d_{24} \end{bmatrix} \tag{B.8}$$

Appendix C

Publications and Conferences Related to This Thesis

Articles

R. Saleem-Urothodi, J. Le Pouliquen, T. Rohel, R. Bernard, C. Pareige, A. Lorenzo-Ruiz, A. Beck, A. Létoublon, O. De Sagazan, C. Cornet, Y. Dumeige, and Y. Léger, “Loss assessment in random crystal polarity gallium phosphide microdisks grown on silicon,”Optics Letters,vol. 45, no. 16, p. 4646, 2020.

A. Lorenzo-Ruiz and Y. Léger, “Generalization of Second-Order Quasi-phase-matching in Whispering Gallery Mode Resonators Using Berry Phase,”ACS photonics, 2020.

A. Lorenzo-Ruiz, C. Cornet, A. Beck, and Y. Léger, “Dual wavelength evanescent coupler for nonlinear GaP-based microdisk resonators,”OSA Continuum, vol. 3, no. 1, pp. 43–49, 2020.

Conferences

A. Lorenzo-Ruiz, C. Cornet, A. Beck, and Y. Léger, “Dual wavelength coupler for second-harmonic generation in gallium phosphide microdisks,” 19th International Conference Laser Optics (ICLO), (St.Petersburg, Russia), Nov. 2020.

R. Saleem-Urothodi, J. Stervinou, T. Rohel, R. Bernard, C. Pareige, A. Lorenzo-Ruiz, A. Beck, A. Létoublon, O. De Sagazan, C. Cornet, Y. Dumeige, and Y. Léger, “Crystal-polarity engineered gallium phosphide microdisks grown on silicon.” IOP PHOTON, Cambridge, September 2020. Invited talk.

A. Lorenzo-Ruiz, Y. Léger, C. Cornet, and A. Beck, “THz sur-face phonon polariton generation in GaP photonic waveguide,” 44thInternational Conference on Infrared, Millimeter, and Terahertz Waves (IRMMW-THz), Paris, September 2019

C. Cornet, L. Chen, A. Lorenzo-Ruiz, I. Lucci, A. Beck, L. Pedesseau, and Y. Léger, “Monolithic integration of III-V semiconductors on silicon for photonics and solar hydrogen production.” SPb Photonic, Optoelectronic, Electronic Materials (SPb-POEM), St Petersburg, April 2019. Invited talk.

Posters

A. Lorenzo-Ruiz, A. Beck, C. Cornet, and Y. Léger, “Dual wavelength vertical coupling for SHG in GaP microdisks.” Journée Scientifique Nanomatériaux, Rennes, January 2020.

A. Lorenzo-Ruiz and Y. Léger, “Quasi-Phase Matched 2nd Order Nonlinearity In Whispering Gallery Mode Resonators: A Generalization Using Berry Phase.” OSA Advanced Photonics Congress, July 2020.

A. Lorenzo-Ruiz, A. Beck, C. Cornet, and Y. Léger, “Dual wavelength vertical coupling for SHG in GaP microdisks.” 39ème Journées Nationales d’Optique Guidée (JNOG),Paris-Saclay, July 2019.

A. Lorenzo-Ruiz, A. Beck, C. Cornet, and Y. Léger, “Slit waveguide coupling system for integrated microresonator.” Journées Nano, Micro et Optoélectronique (JNMO),Agay, June 2018.

Appendix D

Résumé en Français

Motivée par la quête du calcul quantique et à plus court terme le développement d'interconnexions optiques sur puces, la recherche en photonique intégrée a connu un essor considérable durant la dernière décennie. De nombreuses fonctionnalités optiques, les briques élémentaires des circuits photoniques de demain, doivent en effet être démontrées. De par leurs spécificités, une partie d'entre elles se basent sur l'optique non-linéaire. Si le silicium reste la plateforme technologique de référence pour la circuiterie photonique passive, son absorption lorsqu'on se rapproche du spectre visible ($< 1,1 \mu m$, voir figure D.1)et son caractère centrosymétrique qui le rend inadapté à l'optique non-linéaire au second ordre dans les conditions normales imposent de trouver de nouveaux matériaux pour le développement de circuits photoniques non-linéaires

L'une des principales alternatives pour ces dispositifs est l'utilisation des semiconducteurs III-V. Avec une susceptibilité non- linéaire au second ordre élevée (χ^2), ils permettent des processus non- linéaires efficaces. Ils présentent également un indice de réfraction élevé permettant un fort confinement optique bénéfique à la

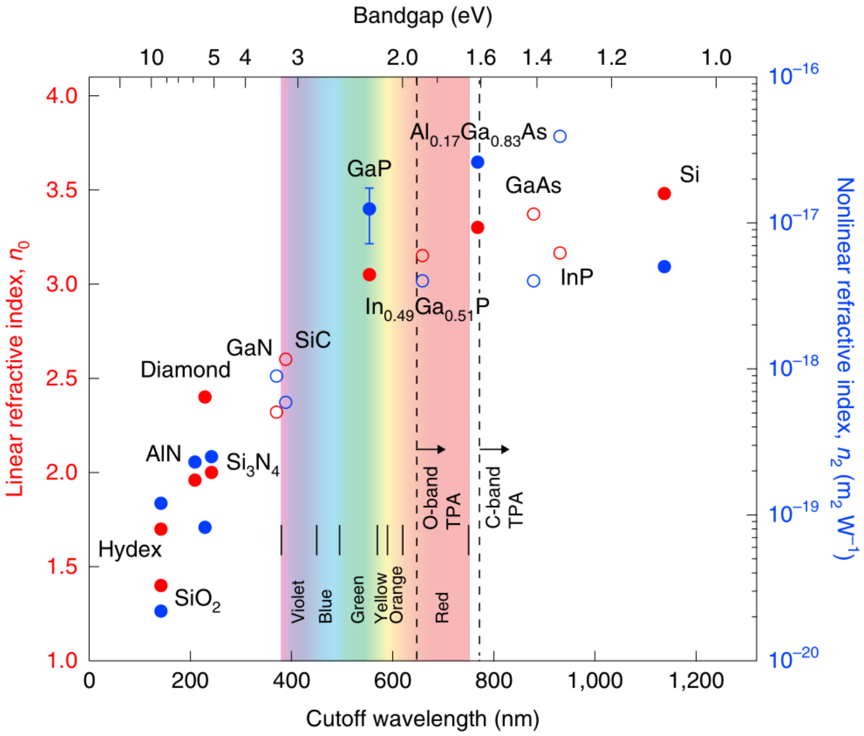

Figure D.1: Indices de réfraction linéaire (rouge) et non-linéaire (bleu) de différentes matériaux pour la photonique intégrée, représentés en fonction de l'énergie du bande interdite et de la longueur d'onde correspondante [46] démonstration d'effets non-linéaires. Parmi eux, le phosphure de gallium (GaP) apparaît comme un candidat de choix du fait de sa large bande interdite, sa susceptibilité au second ordre élevée et la possibilité d'en réaliser l'épitaxie sur silicium.

Dans ce travail de thèse, nous avons exploré deux applications possibles de la plateforme photonique non-linéaire constituée de GaP.

- La première application est un convertisseur de longueur d'onde, basé sur la génération de seconde harmonique dans les microdisques de phosphure de gallium. Ces microrésonateurs à modes de galerie sont des structures parmi les plus prometteuses pour le développement de composants non-linéaires, grâce au fort confinement optique qu'elles offrent et aux multiples possibilités de couplage de ces structures au sein de circuits photoniques. Dans ce manuscrit, nous étudions différents aspects de la physique de ces dispositifs : Nous discutons dans un premier temps la stratégie de couplage de ces microrésonateurs au sein d'une architecture photonique 3D afin d'optimiser l'efficacité de conversion de fréquence et la tolérance des dispositifs vis-à-vis des défauts de fabrication. Nous introduisons ensuite un nouveau cadre théorique pour la compréhension du quasi-accord de phase naturel, observé dans les phénomènes non-linéaires à l'ordre 2 au sein de résonateurs circulaires. Finalement, nous abordons quelques points clés de la fabrication de ces dispositifs non-linéaires intégrés à base de GaP

- La deuxième configuration est la génération d'ondes THz dans la Reststrahlen band des semi-conducteurs (autour 11-12 THz pour le GaP) par génération de différence de fréquences. Nous proposons ici une nouvelle approche pour la génération d'ondes THz dans cette gamme spectrale, laquelle nécessite de prendre en compte la propagation de ces dernières sous la forme de phonons-polaritons de surface.

Conception de l'intégration des microdisques III-V pour la génération seconde harmonique

Dans ce chapitre, nous étudions les stratégies de couplage évanescent d'un microdisque à base de GaP pour la génération de seconde harmonique au sein d'une architecture photonique intégrée 3D. La stratégie de couplage communément choisie pour le couplage évanescent d'un microdisque avec un guide d'onde est d'obtenir un accord des constantes de propagation entre les modes de galerie du résonateur et les modes du ou des guides d'accès, afin d'atteindre le régime de couplage critique. En réintroduisant la possibilité du désaccord des constantes de propagation dans la théorie des modes couplés, nous démontrons que l'efficacité du couplage évanescent dépend en premier lieu d'une interdépendance entre ce désaccord et l'intégrale de recouvrement des champs (κ) (figure D.2 a)).

Par le biais de simulations FDTD (finite difference time domain) 3D, nous explorons différentes configurations de coupleurs évanescents verticaux et estimons l'impact de leur design sur l'efficacité de conversion de fréquence non-linéaire du dispositif. La conclusion majeure de cette étude est que le couplage critique n'est pas la configuration d'efficacité maximale. Selon le désaccord de constante de propagation considéré, il est possible d'atteindre des régimes de couplage extrêmement tolérants sur la valeur de l'intégrale de recouvrement des champs. Cet effet se traduit de manière pratique par une tolérance expérimentale dans la fabrication des dispositifs, autorisant notamment des fluctuations de la distance entre microrésonateurs et

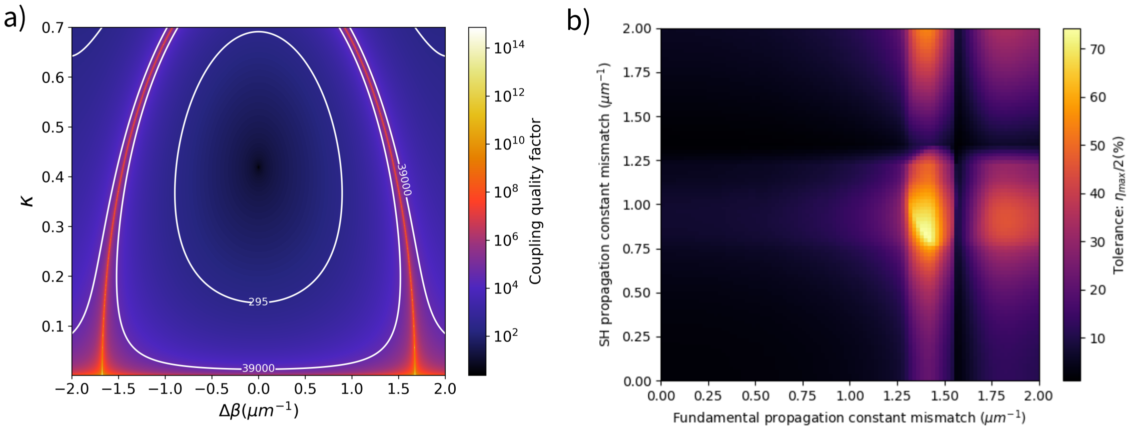

Figure D.2: a) Graphique du facteur de qualité de couplage en fonction du désaccord des constantes de propagation et de l'intégrale de recouvrement des modes pour une longueur de couplage de 3.75 µm. Les courbes blanches correspondent aux facteurs de qualités intrinsèques des modes de galerie impliqués dans le processus de conversion de fréquence et donc aux situations de couplage critique. b) Graphique de la tolérance sur les intégrales de recouvrement des champs pour le couplage du mode fondamental et de seconde harmonique en fonction de leur désaccord de constantes de propagation.

guides, sans conséquence sur l'efficacité des dispositifs (figure D.2 b)).

Étude du seconde ordre quasi-accord de phase dans les résonateurs de modes de galerie

Dans les processus non-linéaires au second ordre au sein de résonateurs axisymétriques, la condition d'accord de phase apparaît comme une règle de sélection sur l'ordre azimutal des modes de galerie initiaux et finaux. En fonction de la symétrie du cristal et du matériau, des quanta additionnels de moment angulaire peuvent apparaître dans cette règle de sélection. Dans l'étude précédente, nous avions considéré une condition d'accord de phase de type $\bar{4}$, liée à l'utilisation d'un matériau de type zinc-blende, comment le GaP [47]. Dans un processus de génération de seconde harmonique, la relation entre les nombres azimutaux du mode fondamental et du mode de seconde harmonique s'écrit:

$$\Delta m = m_{SH} - 2m_{fondamental} = \pm 2 \tag{D.1}$$

Ceci a été attribué à une periodicité naturelle de la polarité du cristal dans les systèmes axisymétriques. Dans ce travail nous revisitons la théorie de l'accord de phase afin de démontrer que ces quanta additionnels proviennent de la conversion d'une phase de Berry de certaines composantes de polarisations des modes de galerie en moment azimutal. Il a en effet été récemment démontré que la lumière peut acquérir un moment de spin transverse (transverse spin angular momentum - TSAM) dans des systèmes fortement confinés tels que les résonateurs à mode de galerie. Les composantes TSAM des modes de galerie, décrits dans une base de polarisation circulaire alignée sur l'axe du résonateur, sont donc soumis à l'acquisition d'une phase topologique lors de leur révolution au sein d'un résonateur. En réécrivant le tenseur de susceptibilité du second ordre du matériau considéré dans cette base circulaire, il est alors possible de montrer comment la non-linéarité au second ordre couple les composantes TSAM du champ et résulte dans la conversion de phase de Berry en moment azimutal. Nous généralisons cet effet à l'ensemble des symétries cristallines et montrons que chaque élément du tenseur de susceptibilité non-linéaire du second ordre est associé à un condition unique de quasi accord de phase.

Fabrication et caractérisation des dispositifs intégrés à base de GaP

Les études précédentes permettent de nous donner les clés du design de microrésonateurs III-V à mode de galerie pour la conversion de fréquence et de leur architecture de cou-

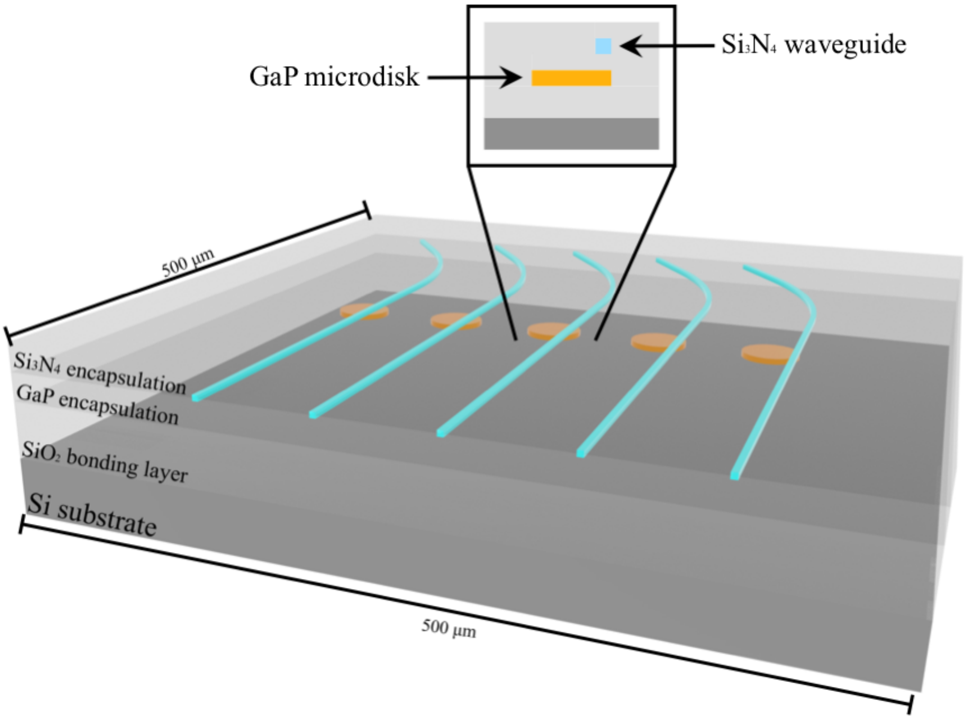

Figure D.3: Représentation schématique de l'architecture photonique à base de GaP envisagée

plage au sein d'un circuit photonique 3D. Dans ce chapitre, nous explorons plusieurs verrous technologiques de la fabrication de tels dispositifs. L'architecture photonique visée est constituée de microdisques de GaP reportés sur substrat diélectrique, encapsulés et couplés à un deuxième étage photonique de guides d'onde en nitrure de silicium (figure D.3).

Pour le collage d'une membrane GaP sur un substrat diélectrique à partir de couche épitaxiées de GaP sur silicium, deux solutions technologiques sont étudiées: l'utilisation de résines comme adhésif, notamment le benzocyclobutène et le collage moléculaire avec SiO_2. Les résultats préliminaires sont très prometteurs notamment pour le collage avec SiO_2, même si la gestion de la contrainte sur la couche épitaxiée de

GaP lors de la suppression du substrat de Si doit être mieux maitrisée. Pour la mise en forme des couches photoniques de GaP et de Si_3N_4 de notre architecture, des techniques de lithographie doivent être utilisées. En raison de la petite taille des guides et des résonateurs, et l'alignement requis entre ces éléments, la lithographie électronique (e-beam) est la solution retenue. Afin de simplifier les procédés technologiques ayant permis de réaliser la précédente génération de microdisques de GaP/Si [97], nous avons mis en place un procédé de lithographie électronique basé sur l'utilisation de silsesquioxane d'hydrogène (HSQ) comme résine électrosensible, pertinente car elle peut directement être utilisée comme masque pour la gravure du GaP. La rugosité latérale des dispositifs tests obtenus a été mesurée à 4 nm RMS sans aucun signe de pixellisation dans des motifs circulaires. Le dépôt d'une couche d'encapsulation des composants photoniques de GaP et la planarisation de cette couche sont étudiées par l'utilisation du BCB ou du SiO2. Les deux alternatives donnent de bons résultats mais l'expertise acquise dans le traitement de surface de SiO2 pour le processus de collage, semble constituer un avantage pour l'intégration des dispositifs.

Photonique non-linéaire à base de phosphure de gallium pour la génération de THz

Nous étudions et proposons une nouvelle approche pour la génération intégrée de THz dans la Reststrahlen band. Cette bande spectrale, entre 5 THz et 15 THz pour les semi-conducteurs III-V, manque de sources, notamment en ce qui concerne les sources intégrées et à température ambiante. Notre approche pour la génération d'ondes THz dans cette bande spectrale est l'utilisation de processus non linéaires, notamment la génération de différence de fréquences à partir de pompes dans le n-IR ou le m-IR.

Nous proposons l'utilisation d'un guide photonique de type stripe à base de GaP pour réaliser ce processus non-linéaire. Cette configuration va permettre de confiner et guider le modes terahertz sous la forme de phonons polaritons de surface (SPhP). Afin d'optimiser le recouvrement des champs de pompes avec le champ THz, nous démontrons que l'orientation du guide par rapport au cristal de GaP communément utilisée pour ce type de processus, la direction[110], n'est pas concluante lorsque l'onde THz se propage sous la forme de SPhP. Au contraire, la direction [100] est la plus indiquée pour cette tâche (figure D.4).

Nous avons optimisé la géométrie du guide de GaP pour obtenir l'accord de phase avec un pompage dans l'infrarouge proche. Les efficacités obtenues atteignent $7.5 \times 10^{-6}\,\mathrm{W}^{-1}$, au niveau du 'état de l'art, mais une faible tolérance sur les paramètres de fabrication et la nécessité de grandes distances de propagation sont constatées. Avec un pompage dans l'infrarouge moyen, le désaccord de phase observé a pour conséquence des efficacités 4 ordres de grandeur plus petites mais avec des distances de propagation plus réalistes du point de vue expérimental.

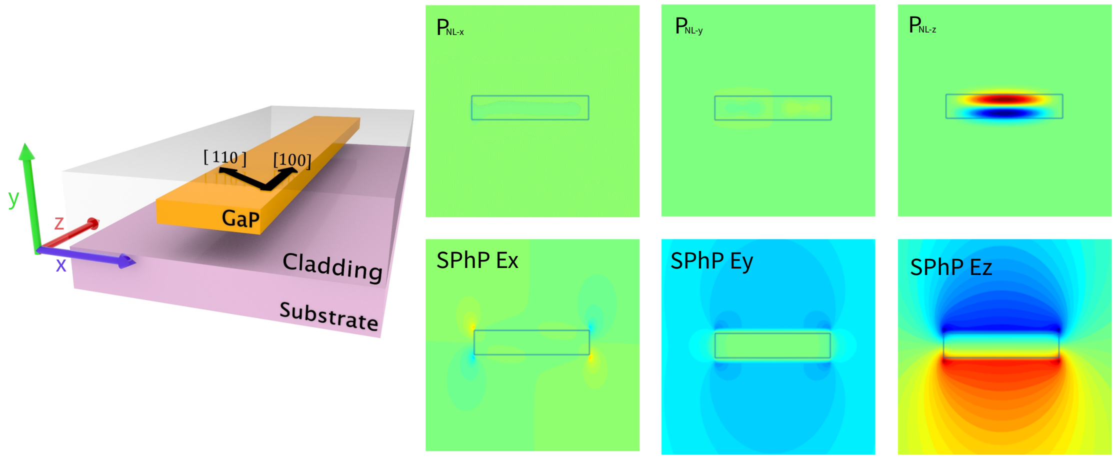

Figure D.4: Profils du modes de la polarisation non-linéaire pour la combinaison des modes TM-TE dans le infrarouge moyen dans la direction de propagation [100] par rapport aux composantes du champ électrique du SPhP. Un croquis en 3D (à gauche) est placé pour plus de clarté.

INSA de RENNES
Service des Formations

AVIS DU JURY SUR LA REPRODUCTION DE LA THESE SOUTENUE

Titre de la thèse:
Dispositifs photoniques intégrés à base de phosphure de gallium pour l'optique non-linéaire

Nom Prénom de l'auteur : LORENZO RUIZ ALEJANDRO

Membres du jury :
- Madame BOUCHOULE Sophie
- Monsieur LÉO François
- Monsieur CORNET Charles
- Monsieur BECK Alexandre
- Monsieur LÉGER Yoan
- Madame MONAT Christelle
- Monsieur CHAUVET Mathieu

Président du jury : Madame BOUCHOULE Sophie

Date de la soutenance : 05 Février 2021

<u>Reproduction de la these soutenue</u>

☒ Thèse pouvant être reproduite en l'état
☐ Thèse pouvant être reproduite après corrections suggérées

Fait à Rennes, le 05 Février 2021

Signature du président de jury

S. Bouchoule

Bouchoule

Le Directeur,

Abdellatif MIRAOUI

DOCTORAT BRETAGNE LOIRE / MATIERE MOLECULES ET MATERIAUX

INSA RENNES

Titre : Dispositifs photoniques intégrés à base de phosphure de gallium pour l'optique non-linéaire

Mots clés : photonique intégrée, photonique non-linéaire, circuits photoniques, microrésonateurs

Résumé : L'objectif de cette thèse est d'étudier les différents aspects de dispositifs intégrés non linéaires basés sur le phosphure de gallium, en se concentrant sur deux processus : l'utilisation des microdisques de GaP pour effectuer la génération de seconde harmonique dans le régime de l'infrarouge proche en utilisant les modes de galerie et l'utilisation des ondes IR pour produire des ondes THz en utilisant la génération de différence de fréquences.

Tout d'abord, nous étudions le processus de couplage évanescent vertical à un microdisque de GaP afin d'étudier son impact sur l'efficacité du dispositif non linéaire et de démontrer l'importance des coupleurs avec désaccord de constante de propagation pour concevoir des dispositifs entièrement encapsulés. Nous démontrons également que l'origine des règles de sélection spécifiques de l'accord de phase dans les microrésonateurs circulaires proviennent de la conversion d'une phase de Berry de certaines composantes de polarisations des modes de galerie en moment azimutal .

Pour fabriquer ce type d'architecture photonique, nous avons étudié les verrous technologiques pour la fabrication de ces circuits photoniques à base de GaP. Nous nous sommes concentrés sur trois processus : le collage, la lithographie et l'encapsulation.

Finalement, nous proposons une nouvelle approche pour la génération intégrée de THz dans la Reststrahlen band. En utilisant les modes de phonons polaritons de surface pour guider les ondes THz et en montrant comment un alignement inhabituel des cristaux est adapté à cette configuration, nous estimons des efficacités de conversion à l'état de l'art.

Title : Nonlinear integrated photonic devices based on gallium phosphide

Keywords : Integrated photonics, nonlinear photonics, photonic circuits, microresonators

Abstract : The objective of this thesis is to investigate different aspects of nonlinear integrated devices based on GaP material, focusing on two processes: the use of GaP microdisks to perform second harmonic generation in the near infrared regime using whispering gallery modes and the use of IR waves to produce THz using difference frequency generation.

First, we study the vertical evanescent coupling process to a GaP microdisk to address its impact on the efficiency of the nonlinear device and demonstrate the importance of propagation constant mismatched couplers to properly design fully encapsulated devices.

We also demonstrate that the origin of the specific phase matching selection rules in circular microresonators is due to the Berry phase experienced by the transverse spin angular momentum components of the WGMs into azimuthal momentum.

To fabricate the designed schemes, we investigated the technological challenges of the process flow for the fabrication of these GaP-based photonic circuits, focusing on three processes: bonding, lithography, and encapsulation.

Finally, we propose a novel approach for integrated THz generation in the Reststrahlen band. Using surface phonon polariton modes to guide THz waves and showing how an unusual crystal alignment is suited for this configuration we estimate efficiencies about the state-of-the-art level.